

# Analysis of Hypersonic Boundary Layer Turbulence by Means of Focused Laser Differential Interferometry

## **Dissertation**

zur Erlangung des akademischen Grades

**Doctor rerum naturalium**

– **Dr. rer. nat.** –

vorgelegt von

**Giannino Ponchio Camillo**

Justus-Liebig-Universität Gießen

Fachbereich 07, I. Physikalisches Institut

**angefertigt am**

Institut für Aerodynamik und Strömungstechnik  
des Deutschen Zentrums für Luft- und Raumfahrt e.V.  
in Göttingen

Juni 2023

Erstgutachter: Prof. Dr. Peter J. Klar  
Zweitgutachter: Prof. Dr. Andreas Dillmann  
Prüfungsdatum: 1. November 2023

---

Ich erkläre: Ich habe die vorgelegte Dissertation selbstständig und ohne unerlaubte fremde Hilfe und nur mit den Hilfen angefertigt, die ich in der Dissertation angegeben habe. Alle Textstellen, die wörtlich oder sinngemäß aus veröffentlichten Schriften entnommen sind, und alle Angaben, die auf mündlichen Auskünften beruhen, sind als solche kenntlich gemacht. Ich stimme einer evtl. Überprüfung meiner Dissertation durch eine Antiplagiat-Software zu. Bei den von mir durchgeführten und in der Dissertation erwähnten Untersuchungen habe ich die Grundsätze guter wissenschaftlicher Praxis, wie sie in der „Satzung der Justus-Liebig-Universität Gießen zur Sicherung guter wissenschaftlicher Praxis“ niedergelegt sind, eingehalten.

Gießen, den 27. Juni 2023

---

Giannino Ponchio Camillo



# Acknowledgments

I thank God for blessing me and my family with the life-changing experience that was conducting this Ph.D. project. This thesis is a dream come true, which was only possible due to the support of many people, all of whom have my deepest gratitude and admiration.

I would like to thank Prof. Dr. Klaus Hannemann, who took me in as a Ph.D. candidate and believed in my commitment and competence early on. I am very sorry that he couldn't be here to see the completion of this thesis. His work has motivated me to pursue this project at DLR, and it was a privilege to have met him and to have worked under his supervision. I am thankful to Prof. Dr. Peter J. Klar, who kindly stepped in when needed as the Supervisor of this work. His resolve was an inspiration, and his friendly and constructive advice towards the elaboration of this thesis and conclusion of this Ph.D. project was always appreciated. I would also like to thank Prof. Dr. Andreas Dillmann, the second Supervisor of this thesis, for his support on the DLR-Göttingen side, without which this work would not have been possible. Thank you also to Jan Martinez Schramm for the incentive and positive attitude towards my work at DLR.

A huge thanks is in order to Alexander Wagner, who has been a mentor and a friend from day one. His teachings and scientific advice in the HEG laboratory were numerous and paramount to the quality of the results presented here. His immense knowledge and friendly personality have made our many technical discussions over the years always a pleasure, and among the richest forms of learning. His attention to the tiniest details when working together on the papers that compose this thesis, even though maddening at times, has contributed to making me a better scientist, and I thank him for that. He has also had a major role in welcoming my family to Germany, from the occasional gathering for dinner with the kids to climbing, skiing, ice-skating, swimming, hiking, indoor-skydiving, and acrobatic flying in a glider (because why not?). For that, I will never be able to thank him enough.

To the technical wizards at HEG, from whom I have also learned a great deal: Ingo Schwendtke, Uwe Frenzel, and Fabian Glasewald, my many thanks as well. This work would not have been possible without their talent and dedication to HEG, and their patience with my questions and shortcomings. It was a great honor to be considered a part of the HEG-team.

A big thanks to Divek Surujhlal, for the pleasant long hours working together at the lab and his light way of looking at things. To the folks from all over the world who just happened to be at DLR-Gö at the same time and became good friends (Divek included): Keith Soal, Jimmy-John Hoste, James Bell, Tamás Bykerk and their families, thank you for the great times together. I am also grateful to the colleagues in the AS-RFZ department at DLR-Gö for the the nice interactions over

---

these years, in particular Lisa Meyer with her uncanny ability to get the whole department together to do something other than work sometimes. Thanks also to the DLR-Gö Fußball group, for whom there were no weather conditions bad enough to stop practicing the world's greatest sport.

I am deeply grateful to the Brazilian Air Force, for having offered me the chance to be in Germany during the necessary time to conduct the present work. My sincere thank you to all the men and women involved in making this possible.

A heartfelt thanks to my parents, Alexandra and Pierangelo, and my little sister, Danielle. They have taught me that knowledge is one's most important asset, and showed me that dedication and perseverance are among the strongest of allies. I am glad to have lived by those words, through which this thesis was written.

Finally, none of this would have made sense without my lovely and incredible wife and best friend, Mariana. I am very lucky to have had the opportunity to live through this journey by her side. At all times, good or bad, her friendship, companionship, optimism and love have pushed me forward and taken us to a place we can both be proud of. Amore mio, this thesis is dedicated to you.

# Contents

<b>Abstract</b>	<b>xi</b>
<b>Zusammenfassung</b>	<b>xiii</b>
<b>1. Overlook</b>	<b>15</b>
<b>2. Introduction</b>	<b>17</b>
2.1. High-speed turbulent boundary layers . . . . .	17
2.2. The need for experimental data . . . . .	19
2.3. Focused Laser Differential Interferometry . . . . .	20
<b>3. Results and Discussion</b>	<b>23</b>
3.1. Measurement of separation distance between FLDI probes using blast waves (Publication 1) . . . . .	23
3.2. Validation of computational FLDI as an analysis tool (Publication 2)	38
3.3. Hypersonic turbulent boundary layer investigation using FLDI (Publication 3) . . . . .	55
<b>4. Conclusions</b>	<b>89</b>
<b>Bibliography</b>	<b>93</b>
<b>A. Lens formula for FLDI <math>\Delta x_1</math> calibration</b>	<b>101</b>
<b>B. Transfer function of FLDI spatial filtering</b>	<b>105</b>



# Abbreviations

<b>CFD</b>	.....	Computational Fluid Dynamics
<b>cFLDI</b>	.....	Computational Focused Laser Differential Interferometer
<b>DLR</b>	.....	Deutsches Zentrum für Luft- und Raumfahrt
<b>FLDI</b>	.....	Focused Laser Differential Interferometer
<b>HEG</b>	.....	High Enthalpy Shock Tunnel Göttingen
<b>HWA</b>	.....	Hot-wire anemometry
<b>LES</b>	.....	Large-Eddy Simulation
<b>PIV</b>	.....	Particle image velocimetry
<b>RANS</b>	.....	Reynolds-Averaged Navier-Stokes
<b>RMS</b>	.....	Root-mean-square
<b>SNR</b>	.....	Signal-to-noise ratio
<b>SRA</b>	.....	Strong Reynolds Analogy



# Abstract

This thesis investigates a hypersonic turbulent boundary layer over a cone with cold walls and a sharp nose tip. The analyses include frequency spectra of density fluctuations up to a frequency of 10 MHz, as well as an analysis of their convection velocities, at multiple wall-normal locations inside the boundary layer and in the near field above it. Experimental measurements are obtained under Mach 7.4 and unit Reynolds number  $4.2 \times 10^6 \text{ m}^{-1}$  in the free-piston driven High Enthalpy Shock Tunnel Göttingen (HEG), using the optical technique of Focused Laser Differential Interferometry (FLDI). A method is proposed to accurately measure the separation distance between the probes of multi-foci FLDI, to allow reliable measurements of convection velocities using cross-correlation between the signals. The method is based on the detection of a propagating weak blast wave generated by an electric spark, and is verified to have similar accuracy and precision than the method of directly imaging the beams, but exhibits increased flexibility. Convection velocities measured in the near field of the hypersonic boundary layer are in agreement with free stream data reported in the literature at similar Mach numbers. The measured frequency spectra of hypersonic turbulent boundary layer density fluctuations show regions with well-defined power laws typical for pressure fluctuations. These spectra are compared with Large-Eddy Simulation (LES) results for a conical turbulent boundary layer, calculated at the experimental test conditions. Direct comparisons are performed by simulating the FLDI response in the numeric flow field, by means of computational FLDI (cFLDI). The cFLDI algorithm is validated using the same blast wave measurements obtained when measuring the separation distance between FLDI probes. To that end, an analytic methodology is proposed to reconstruct the pressure waveform of the spherical blast wave, when detected with the straight-line FLDI. Independence between the cFLDI algorithm and the reconstruction formulation allow the cFLDI code to be validated once the computational response of the reconstructed flow field and the experimental data that generated it are in agreement. The results of the direct comparison between the hypersonic turbulent conical boundary layer frequency spectra calculated with LES and experimentally probed in HEG are in reasonable agreement, once the bandwidth constraints of each are adequately considered. It is also verified that in the present case, in which the divergence of the FLDI beams in the probed region is small, the complex cFLDI algorithm may be substituted by a simple line integral of density variations in the numeric flow field, without significant losses. These observations offer a framework for practical numerical and experimental comparisons, which are necessary to validate simulations and turbulence models. The results of this thesis will help to overcome the current lack of experimental data concerning high-speed turbulent flows, especially at high frequencies.



# Zusammenfassung

Diese Arbeit untersucht eine turbulente Hyperschallgrenzschicht an einem Kegel mit kalten Wänden und einer scharfen Spitze. Die Analysen umfassen Frequenzspektren von Dichteschwankungen bis zu 10 MHz sowie deren Konvektionsgeschwindigkeiten in verschiedenen Abständen zur Oberfläche innerhalb der Grenzschicht und im darüber liegenden Nahfeld. Experimentelle Messungen wurden bei Mach 7.4 und einer Einheitsreynoldszahl von  $4.2 \times 10^6 \text{ m}^{-1}$  im Hochenthalpiekanal Göttingen (HEG) mittels der optischen Technik Fokussierte Laser-Differentialinterferometrie (FLDI) durchgeführt. Für die Bestimmung des Abstandes zwischen den Messpunkten eines FLDI mit mehreren Fokusse wird eine neue Methode vorgestellt, die eine präzise Messungen der Konvektionsgeschwindigkeit durch eine Kreuzkorrelation der Signalen ermöglicht. Die Methode basiert auf der Detektion einer sich ausbreitenden schwachen Druckwelle, die durch einen elektrischen Funken erzeugt wird. Die Methode hat eine ähnliche Genauigkeit und Präzision wie die direkte Abbildung der Strahlen, weist aber eine erhöhte Flexibilität in der Anwendung auf. Im Nahfeld der Hyperschallgrenzschicht stimmen die gemessenen Konvektionsgeschwindigkeiten mit Daten aus der Literatur für ähnliche Machzahlen überein. Die gemessenen Frequenzspektren turbulenter Hyperschallgrenzschichtdichteschwankungen zeigen Bereiche mit den für Druckschwankungen typischen Abfällen. Diese Spektren werden mit Ergebnissen einer Large-Eddy Simulation (LES) einer konischen turbulente Grenzschicht verglichen, die mit den experimentell Anströmungsbedingungen berechnet wurden. Direkte Vergleiche werden mittels eines numerischen FLDI-Verfahrens (cFLDI) im numerischen Strömungsfeld durchgeführt. Der cFLDI-Algorithmus wird anhand derselben Druckwellenmessungen validiert, die bei der Messung des Abstands zwischen FLDI-Messstellen zur Anwendung kamen. Dafür wird eine analytische Vorgehensweise vorgeschlagen, um die Form der sphärischen Druckwelle zu rekonstruieren, während diese mit dem geradlinigen FLDI interagiert. Die Unabhängigkeit zwischen dem cFLDI-Algorithmus und der Rekonstruktionsformulierung ermöglicht die Validierung des cFLDI-Codes. Die Ergebnisse des direkten Vergleichs zwischen den mittels LES berechneten und experimentell im HEG untersuchten Frequenzspektren der turbulenten Hyperschallgrenzschicht stimmen gut überein, wenn die jeweiligen Bandbreitenbeschränkungen berücksichtigt werden. Es wird auch bestätigt, dass im vorliegenden Fall, in dem die Divergenz der FLDI-Strahlen im untersuchten Bereich gering ist, der komplexe cFLDI-Algorithmus ohne wesentliche Verluste durch ein einfaches Linienintegral von Dichteschwankungen im numerischen Strömungsfeld ersetzt werden kann. Diese Beobachtungen bieten einen Rahmen für praktische numerische und experimentelle Vergleiche, die zur Validierung von Simulationen und Turbulenzmodellen notwendig sind. Die Ergebnisse der Dissertation leisten einen wesentlichen Beitrag, um in der Zukunft den Mangel an experimentellen Daten von turbulenten Hochgeschwindigkeitsströmungen, insbesondere bei hohen Frequenzen, zu überwinden.



# 1. Overlook

The goal of this Ph.D. project is to contribute to the advancement of the state-of-the-art of ground-based experimental investigation of hypersonic turbulent boundary layers. The optical technique of Focused Laser Differential Interferometry (FLDI) is explored to that end, given its features of unique temporal and spatial resolutions, and its ability to overcome measurement challenges pertaining to the wind-tunnel environment. The developments presented here are focused on two aspects of the FLDI that are important in the context of its application in hypersonic turbulent boundary layer investigations: its capability as a velocimetry instrument, and the challenge of reversing its output back into flowfield quantities.

The use of FLDI as a velocimetry instrument is allowed by the easy way in which the probes can be multiplied into closely-spaced, independent systems, becoming a multi-foci FLDI. This capability allows investigators to correlate the time-resolved density disturbances with their spatial dimensions, hence providing a more complete picture of the probed flowfield. Convection velocity measurements are obtained simply by using the time lag between the signals of each probe and the distance between them. This distance can be easily measured by directly imaging the FLDI foci. However, this approach may be hindered by geometric constraints, such as in the case of boundary layer studies, where the foci are located close to the wall of the wind-tunnel model. An alternative method to measure beam spacing that overcomes such limitation, while preserving adequate accuracy and precision, has been developed through measurements of weak blast waves. This original contribution is detailed in the first publication, “*A low-effort and inexpensive methodology to determine beam separation distance of multi-foci FLDI*”.

The challenge of reversing FLDI measurements back into flowfield quantities comes from the spatial filtering effect of the FLDI, which varies continuously with the disturbance wavenumber along the probing axis. This makes the FLDI data conversion only possible under certain constraints, which may not be applicable to all cases. In the present work, computational FLDI (cFLDI) is explored as a possibility to avoid this issue altogether when attempting to compare experimental and numerical results. In this methodology, instead of the conventional approach of processing experimental results into flowfield quantities, the opposite is used: the cFLDI extracts quantities from the numeric flowfield that are directly comparable to the experiments.

There is of yet no commercial tool that simulates FLDI measurements. The code to do so in the present work has been implemented in-house based on recent reports in the literature on the topic. A validation case of this code has been pursued by investigating the blast wave measurements of the first publication within the scope of fluid dynamics. In order to perform the validation of the FLDI code, it was necessary to expand an existing methodology to post-process optically-based measurements of circular flowfields, in consideration of special characteristics of the FLDI instrument. This study has led to the second publication, “*Focused laser*

*differential interferometry post-processing methodology for flowfields with circular symmetry*". The flowfield obtained with the original post-processing method is simulated with the custom cFLDI script, and its output is compared against the initial experimental measurements. In addition to validating the cFLDI code, this development lays the foundation for using cFLDI as a tool to analyze the validity of simplifying hypotheses and constraints when post-processing FLDI measurements, regardless of the adopted methodology.

As a result of these two peer-reviewed publications, the disposition of the FLDI foci is accurately measured and the cFLDI tool is developed and validated. This tool set is employed to investigate a hypersonic turbulent boundary layer over a conical model with cold walls at Mach 7.4 in the free-piston driven High Enthalpy Shock Tunnel Göttingen (HEG), at the German Aerospace Center (Deutsches Zentrum für Luft- und Raumfahrt, DLR). A time-resolved Large-Eddy Simulation (LES), calculated under the experimentally observed free stream conditions, provides the numeric flowfield for direct comparison with experiments by means of cFLDI. The findings are reported in the third publication, "*Combined Experimental and Numerical Investigation of a Hypersonic Turbulent Boundary Layer by means of FLDI and Large-Eddy Simulations*". Free stream and boundary layer convection velocity and frequency spectra of density disturbances are reported, showing reasonable agreement with an extrapolation of existing cases and complementing the current database. The experimental convection velocity measurements under the investigated conditions are novel. So are the frequency spectra of the density fluctuations across a hypersonic turbulent boundary layer with a bandwidth up to 10 MHz. The results of numerical and experimental comparisons indicate that the proposed direct approach using cFLDI and FLDI measurements is possible, given appropriate identification of the limitations pertaining to each case, numerical or experimental. This is also a new contribution.

This thesis is structured as follows. Chapter 2 provides an introduction to the topics of high-speed turbulent boundary layer and FLDI, which are central to this work. The three published papers mentioned above are reproduced in their entirety in Chapter 3, each of them preceded by explanatory considerations about their contribution to the current state-of-the-art. The scope chosen for each paper is such that the first paper discusses the experimental setup, the second one explores and validates the implemented cFLDI algorithm, and the final paper addresses the shock tunnel investigation. Detailed expositions of methodologies and the necessary theoretical background to understand them have been included in each paper. For completeness, mathematical proofs of a few of the more work-intensive equations used in the papers are presented in appendixes. Chapter 4 concludes the thesis with a summary of its main results and contributions, and recommendations for future work.

## 2. Introduction

The boundary layer on the surface of an aerospace vehicle plays a fundamental role on its design choices. Heat transfer from a turbulent boundary layer to the surface of the vehicle can be an order of magnitude larger than the laminar case in high-speed flows [1]. If the vehicle is designed considering a worst-case scenario, it may have excessive heat shielding, with implications on weight, maneuverability and range [2]. The increased skin friction in turbulent boundary layers also cause the aerodynamic drag to increase, with an impact on performance. That does not mean, however, that laminar boundary layers are exclusively preferable. On hypersonic vehicles, they may cause problems in the form of flow separation and fuel mixing inefficiency in airbreathing propulsion [3], giving turbulent flows advantages to be traded-off.

### 2.1. High-speed turbulent boundary layers

Applications of high-speed turbulent flows include, for example, acoustic noise estimation and control, potential exhaust plume interaction with control surfaces, fuel mixing in scramjets, influence of wakes on control surfaces and blade interaction in engine rotors, among many others [4]. As a matter of fact, there are predictions that the boundary layer on future airbreathing hypersonic cruise vehicles will be chemically reacting and turbulent [5, 6].

Design requirements for hypersonic re-entry or cruise vehicles may need to inevitably take into account the effects of turbulent boundary layers. Fluid-structure interactions cause vibratory loading of structures due to the passage of turbulent flow, specifically related to small scale, high frequency fluctuations [7, 8]. This vibration and noise transmitted through the structure of an aerospace vehicle can adversely affect, e.g., the components in guidance instruments [9].

An in-depth knowledge of the turbulent behavior of flowfields may also be relevant to enable a better use of experimental observations performed in conventional (noisy) wind tunnels in the design of vehicles to be operated in the low-noise flight environment [10–12].

Aiming at designing such vehicles, the basic understanding of the underlying aerothermodynamic phenomena is fundamental to allow using design tools effectively [13]. Given the broad applications of turbulent boundary layers, it can therefore be seen that the design of hypersonic vehicles has a critical dependence on the accurate prediction of turbulence in high-speed boundary layers.

The advancement of computer technology has enabled exploring computational flowfields to expand the horizons of aerospace vehicle design. If a calculation is performed directly from the Navier-Stokes equations, with enough detail to encompass all significant phenomena, a Direct Numerical Simulation (DNS) flowfield is obtained. However, DNS of complex, three-dimensional flowfields, which are

ubiquitous in engineering applications, is still a tall order. The use of simplified models to emulate the flowfield behavior at its smallest scales is therefore required. Also, in the case of flowfields with high-temperature effects, lower-fidelity turbulence models may allow a larger fraction of computing power to be dedicated to resolving the additional real gas effects [3].

The elaboration of reliable turbulence models requires appropriate consideration of the underlying physics and extensive validation. However, despite the relevance of turbulent phenomena to the design of aerospace vehicles, current understanding of high-speed turbulent boundary layers is still limited due to the lack of available data.

In the absence of experimental high-speed data for validation of models or simulations, available data from the incompressible regime must be used instead [14]. That requires assuming Morkovin's hypothesis, according to which the flow dynamics maintains similarity across the flowfields as long as the Mach number of fluctuations remains small. This hypothesis has a strong impact in the current understanding of turbulence, as it leads to some widely used compressibility transformations. One such transformation is the Van Driest velocity scaling, which transforms the velocity distribution in the inner layer of turbulent boundary layers into a universal profile. Another example is the Strong Reynolds Analogy (SRA), which relates streamwise velocity fluctuations to temperature fluctuations. The SRA is necessary, e.g., for hot-wire measurements lest a number of different overheat ratios is used [15].

However, the validity of Morkovin's hypothesis in the presence of the strong density and pressure fluctuations typical of high-speed flows is a matter of debate [13–19]. In the review work of Spina et al. [20], the authors underlined that Morkovin's hypothesis must have an upper Mach number limit. Contrary to low-speed flows, fluctuations in thermodynamic quantities such as density and temperature become the most significantly varying properties in hypersonic flows [21]. DNS investigations of flat plate turbulent boundary layers at Mach 2.5 [16] and 4.5 [17] have indicated that, indeed, compressibility effects cannot be ignored. On the other hand, turbulent boundary layer DNS investigations at Mach 14 [18] and up to Mach 20 [13] have shown compressibility transformations to hold, although in both cases real gas effects were neglected. Experimental contributions to the discussion are hindered by the still limited measurements at hypersonic speeds that are detailed an accurate enough for testing the validity of Morkovin's hypothesis [22].

Time-averaged models, such as Reynolds-Averaged Navier-Stokes (RANS), when derived for incompressible flow, neglect fluctuations in thermodynamic quantities such as temperature and density, which is unsuited at hypersonic speeds [23]. Most RANS models have been developed and calibrated for highly idealized flowfields, with modifications aiming at correcting deficiencies having been largely empirical and, therefore, not broadly applicable or in some cases invalidated in a later moment [24]. Current turbulence models are still incapable of providing reasonable results for wall-bounded flows with strong heat transfer, such as a hypersonic turbulent boundary layer over a cold surface [25].

## 2.2. The need for experimental data

In line with these observations, an urgent need for detailed experimental turbulence data at high Mach numbers had already been underlined in the 1990s [20]. However, despite the decades since then, limitations of measurement techniques have slowed down experimental efforts. The understanding of the behavior of pressure fluctuations has been pointed out to be lagged behind that of velocity fluctuations in turbulent boundary layers, both in high-speed flowfields [8] and in the subsonic regime [26], due to the lack of suited measurement techniques. Importantly, pressure and velocity have different spectral behavior in turbulent flows [8, 26].

The need for more comparisons between turbulence models and experimental results, especially concerning off-wall data, is again underlined in the review work by Roy and Blottner [27]. The authors also stress the importance of non-intrusive measurement techniques, and the appropriate attention to quantifying experimental uncertainties. While existing measurements mostly provide data in terms of root-mean-square (RMS) values alone, an evaluation of the disturbance spectra up to the high frequencies observed in a transitional hypersonic boundary layer would also be of interest [12].

The knowledge of the power spectrum of density fluctuations has been flagged as a critical ingredient for computational models for LES [28, 29], as well as for the closure of terms of RANS equations [8, 14, 22]. The identification of power laws in the pressure spectrum is a means of gaining insight into the phenomena pertinent to turbulence production. For example, the turbulent energy distribution may be correlated with possible physical sources, e.g., acoustic disturbances in a shock tunnel, depending on the slope of the spectrum [8, 26]. Also, the power laws can be attributed to different sources in the governing equations [30], and indicate the scales of turbulence isotropy [31], which is of relevance for turbulence modeling. Detailed experimental data considered necessary for calibration and/or validation of modeling techniques include controlled and well documented inflow conditions, such as turbulence state and statistics, as well as measurements beyond just the mean flow [4].

Examples of current techniques capable of investigating the disturbance environment in hypersonic wind tunnels are listed in the comprehensive study by Wagner et al. [32]. Pressure fluctuations can be detected using Pitot probes. However, they require protective cavities to endure the thermal loading and be protected against the impact of debris, which leads to frequency-dependent signal damping effects and resonances. Furthermore, the Pitot probe transfer function depends on the shock stand-off distance and the geometry of the probe, which hinders the comparison of results from different probes. Hot-wire anemometry (HWA) can provide velocity measurements. However, HWA presents limited bandwidth (order of 100 MHz), depends on fragile hardware and has limitations for high enthalpy flows. It may also present uncertainties due to mixed-mode sensitivity, being sensitive to both fluctuating mass flux and total temperature [22]. In addition to Pitot probes and HWA, particle image velocimetry (PIV) can be used to obtain turbulence information, specifically on the velocity field [15, 33]. There are, however, challenges

pertaining to the necessary seeding of particles in shock tunnels, and particle lag for measurements in the wall-normal direction. Alternative techniques focusing on overcoming these challenges by using either an inert gas [34] or even the nitrogen in the air [35] as the tagged material are currently in development.

### 2.3. Focused Laser Differential Interferometry

Adding to the non-exhaustive list of techniques mentioned above, density fluctuations and convection velocity of density disturbances can be detected using Focused Laser Differential Interferometry (FLDI). This is the main measurement technique explored in the present work.

FLDI was first proposed in the 1970s [36–38] but has gained momentum more recently, since it was brought to the attention of the hypersonics community with the works of Parziale et al. [39] and Parziale [40]. The most distinctive qualities of the FLDI instrument are an extremely high frequency bandwidth, in the order of 10 MHz, and spatial resolution, in the order of 100  $\mu\text{m}$ , while being able to “see through” the noisy shear layer of shock tunnel nozzles. It presents, therefore, ideal qualities to investigate small fluctuations traveling at high speeds, with the potential to contribute with addressing the lack of experimental data on high-speed turbulence highlighted above.

The most fundamental output of an FLDI instrument, being an interferometer, is a value of phase shift of the laser beam, in radians. This quantity relates to the density gradient of the flowfield along the axis of beam separation in the interferometer [41]. By adding a small number of simple optical components, the FLDI system is easily multiplied into an array of closely spaced (order of 1 mm), independent probes [42]. This multi-foci FLDI instrument has the added ability of measuring the convection velocity of density disturbances, by correlating the outputs from adjacent probes that are separated by a known distance. This is especially relevant because it allows transforming the frequency scale into wavenumbers or wavelengths, which are more amenable to comparisons with models or numeric flowfields.

Over the past decade, FLDI has seen multiple applications. Fundamental studies of FLDI principles of operation are generally performed using a supersonic turbulent free jet [43–52], due to its broad frequency content and the existence of an experimental database and analytic models. An alternative approach is to use a laminar helium jet to study the static response of the FLDI, and single-frequency ultrasonic acoustic beams centered at several frequency values to investigate the dynamic response [53, 54]. Turning to shock tunnel investigations, FLDI has been used to obtain free stream measurements [43, 52, 55–61], probe laminar boundary layers presenting second-mode instabilities [40, 44, 62–69], and investigate disturbances inside a separation bubble [63, 70].

Ways to multiply FLDI probes such as to obtain multi-foci setups have also been targeted by researchers, with different forms of achieving that having been proposed [42, 45, 48, 51, 58, 62, 68, 71]. Multi-foci FLDI configurations have been used to measure convection velocities in supersonic free jets [45, 47, 48, 51], the flowfield generated by a laser induced breakdown [68, 72], disturbances in a shock tube [42], second-mode instabilities in hypersonic boundary layers [62, 64], hypersonic free streams [58, 59], and a scramjet combustor [73].

Despite the ever growing use of FLDI in high-speed wind tunnels around the world demonstrated above, however, its application to hypersonic turbulent boundary layers still remains largely unexplored.

One important caveat concerning FLDI measurements, which may as well be one of the reasons for that, is that the conversion of FLDI data back into flowfield quantities requires some careful considerations. As mentioned above, the most direct output of the FLDI instrument is the phase shift of the laser beam. This quantity has a direct relationship with the density disturbances of the flowfield [41]. However, the phase shift is accumulated across the entire probing volume. The reason why the FLDI is able nonetheless to probe through a noisy shear layer in shock tunnels is that the sensitivity of the FLDI instrument to different sizes of disturbances varies along the optical axis [54, 74, 75]. Disturbances with a wavelength comparable to the beam width get averaged out in the final, integrated response. Hence the sensitivity of the system to high-frequency content, which is associated with disturbances of small scales, is restricted to the vicinity of the focus of the FLDI, where the beam size is minimal. However, because the diameter of the focusing beams varies continuously, so does the FLDI sensitivity to the sizes of disturbances, with no clear cutoff parameter for any given disturbance size.

Many recent works have been devoted to studying this FLDI property and allowing the quantitative conversion of FLDI data into flowfield density values. Fulghum [74] presented the first efforts to use transfer functions to describe the FLDI sensitivity behavior in canonical cases such as a uniform flowfield and a free jet. That approach was later expanded to cases with higher complexity [50]. A solution for the inverse FLDI problem has been deduced for single-direction, continuous-frequency waves [60, 76]. In addition, a framework has been proposed to address the problem by defining a sensitivity function, which depends on parameters of the FLDI setup and the flowfield [47, 77]. These approaches are the current state-of-the-art on FLDI signal post-processing. Nonetheless, assumptions about the geometry and symmetry of the flowfield are inevitable to solve the inverse problem, due to the loss of information associated with the process of turning the three-dimensional density field into a single scalar output value in the form of the laser phase shift [76]. This is an obstacle to taking full advantage of FLDI measurements when probing flowfields with further complexity or non-uniformities.

An alternative approach is explored in the present work, based on advancements on computational FLDI (cFLDI) and high-fidelity numeric flowfield computations. The methodology is useful when a numerical representation of the flowfield exists, such as in a case of turbulence model validation, or combined experimental and numerical investigations. Instead of converting FLDI measurements into density field data, cFLDI is applied to the numeric flowfield to provide quantities that are directly comparable with experiments, with no need for assumptions or simplifications related to FLDI post-processing.

The cFLDI algorithm was first introduced by Schmidt and Shepherd [75]. It consists in calculating the effects of a computational density field on individual rays of light composing the FLDI beams. The only simplification involved in the process is to neglect any deflections of the rays due to the density field. This was verified not to degrade the fidelity of the FLDI simulation in the validation work of Lawson and Austin [78], in which a complex, shock-dominated, dynamic flowfield was studied. To date, only a handful of additional works have explored cFLDI to investigate

high-speed flowfields or the technique itself. It has been used to perform parametric evaluations of the instrument [79, 80], adding to the fundamental understanding of the FLDI principles previously obtained with free jet experiments. Also, a DNS of the boundary layer on the walls of a shock tunnel has been used in combination with cFLDI to assess the instrument's ability to obtain data from the core flowfield [81]. In the present work, the investigations are focused on the core flowfield instead, using cFLDI to extract a simulated response from the computational flowfield.

The present thesis aims at contributing to the advancement of hypersonic turbulence understanding, in particular concerning high-speed turbulent boundary layers and the near field around them. Experimental and computational FLDI are employed to obtain flowfield information in terms of density fluctuations and convection velocity of density disturbances. The methodology and results presented herein represent a means and a small sample of addressing the existing gap in the availability of experimental data on high-speed turbulent flowfields. As such, a rigorous approach is followed to ensure that the quality of the obtained data complies with the stringent requirements for turbulence model validation. Furthermore, the flowfield investigated in this work is one of the suggested cases in the review work of Roy and Blottner [27] as baselines for comparisons between turbulence models and experimental results, namely a sharp cone with a zero-pressure gradient turbulent boundary layer.

## 3. Results and Discussion

This work focuses on advancing the limits of interpretation and reliability of experimental FLDI data for the investigation of hypersonic turbulent boundary layers. The most relevant results are reported in three papers recently published in peer-reviewed journals. These publications compose the core of the present thesis, and are reproduced next.

### 3.1. Measurement of separation distance between FLDI probes using blast waves (Publication 1)

The possibility of velocimetry using a pair of FLDI probes was identified early on in the present Ph.D. project as one of the main advantages of the technique for shock-tunnel investigation. By knowing the separation distance between the FLDI probes, the time lag between closely-spaced probes can be converted into a convection velocity. However, the quality of the velocity measurements are directly dependent on how well the separation distance between the FLDI probes, denoted  $\Delta x_2$ , can be measured. If the measurement of this distance is inaccurate, the velocity results will be biased. In addition, if the distance measurement has a large uncertainty, so will the velocity values.

Accurate and precise beam distance measurements can be obtained using a beam profiler with a large enough sensor area to image the beams. However, this method is not universally applicable. First, the imaging device has a finite size that becomes a constraint in the presence of other objects close to the focus of the FLDI system, such as the wall of a test model. Second, the cost of a beam profiler is comparable to the cost of an entire FLDI system, which may be prohibitive for smaller laboratories. Finally, certain types of multi-foci FLDI, such as the multi-point line FLDI [68], present adjacent probes with no physical separation between them, preventing the use of the imaging approach. The alternative methods that were present in the literature lacked precision, accuracy, or both, as observed in the results of the paper reproduced in this section. One of such methods is the analysis of a lens moving across the optical axis of the FLDI in the direction of beam separation. Although its accuracy and precision for the measurement of the velocimetry-related distance  $\Delta x_2$  was found to be lacking, it was verified to be an excellent alternative to beam imaging in the case of  $\Delta x_1$ , the small separation distance between the pair of beams forming one FLDI. Therefore, a demonstration of the equation employed to obtain  $\Delta x_1$  from the lens measurements, which is usually omitted in the literature, is given in Appendix A.

For the measurement of  $\Delta x_2$ , a solution was found to replace the beam profiler with similar accuracy and precision much reduced geometric constraints, and at a fraction of the cost. The method consists of detecting the passage of a weak blast wave, which propagates at a known speed of Mach 1 in the acoustic limit. A modified

automotive spark plug was used to generate the blast wave. A careful study of the propagation velocity along the radial distance was conducted to identify the acoustic limit region. When using the blast wave detection at a single location within this limit, a beam separation distance within 0.5% of the beam profiler reference value was obtained, with less than 1% uncertainty. By modeling the blast wave trajectory, which allowed using the combined data from the whole probed region, accuracy improved to within 0.2% of the beam profiler reference value. Nonetheless, this comes with significantly more measurement effort, hence the gain was deemed not worth it for most applications.

The conceptual idea of using a controlled acoustic disturbance to measure the separation distance between multi-foci FLDI was proposed by A. Wagner. The experimental setup was designed by I. Schwendtke and me. The experiments and data curation were conducted by me. Analyses of the results were carried out by me and A. Wagner. The manuscript was written by me and edited by A. Wagner. The article is Open Access under a Creative Commons Attribution 4.0 International License (<http://creativecommons.org/licenses/by/4.0/>). It was published in *Experiments in Fluids*, **2022**, *63* (2), 53. (DOI: <https://doi.org/10.1007/s00348-022-03401-0>)

**Copyright © The Authors 2022**



## A low-effort and inexpensive methodology to determine beam separation distance of multi-foci FLDI

Giannino Ponchio Camillo<sup>1</sup> · Alexander Wagner<sup>1</sup>

Received: 25 October 2021 / Revised: 5 February 2022 / Accepted: 8 February 2022  
© The Author(s) 2022

### Abstract

A new method is presented to measure the separation distance between probing volumes of closely spaced multi-foci Focused Laser Differential Interferometers (FLDI). The accuracy and precision of this distance measurement directly translate into the quality of convection velocity measurements performed by means of arrays of FLDI. The suggested method is based on the detection of a propagating weak blast wave, generated with a simple and inexpensive apparatus using an automotive spark plug. Demonstration is conducted using an FLDI with two foci (D-FLDI). The generated blast wave is probed at multiple distances from its source to verify its weakening into an acoustic pulse, which offers ideal conditions to the proposed methodology. D-FLDI separation distance measurement using the new approach is compared to measurements using beam profiler images and to the alternative currently established in the literature, based on the FLDI response to a moving weak lens. Tests are made on varying internal configurations of the D-FLDI, while the distance between the two systems is kept constant. Results show the present method to have improved accuracy and robustness in comparison with the moving lens approach, while requiring significantly less effort. Measured separation distances obtained from blast wave detections in a single location are within 0.5% of the reference value measured through the beam profiler. This procedure is therefore a practical and reliable alternative to the measurement using beam profiler imaging, with similar quality. Its advantages concern associated costs, flexibility when measuring in constrained spaces such as in proximity to walls, and applicability to systems in which beam imaging is not an option, such as multi-point line FLDI.

### 1 Introduction

Focused Laser Differential Interferometry (FLDI) is a non-invasive measurement technique capable of detecting flowfield density fluctuations with remarkable spatial and temporal resolution, being especially suited to the field of experimental hypersonics (Parziale et al. 2013). With simple modifications, it is also possible to use FLDI as a velocity measurement tool by producing two closely spaced probing volumes to obtain a double-foci FLDI (D-FLDI), as shown by Jewell et al. (2016). The detected signal using the two probing volumes is very similar but for a time lag, which can be converted into convection speed measurement if the distance that separates the two systems is known.

In the precursor exploration by Jewell et al. (2016), velocity estimates of second-mode instability wavepackets in a hypersonic boundary layer consistent with typically expected values were obtained using D-FLDI. Exploratory work on velocimetry by means of parallel FLDI measurements has since then been conducted in multiple laboratories. Jewell et al. (2019) presented velocity measurements of compressible turbulent jets. Results followed the jet nominal values, albeit with a consistent offset. Ceruzzi and Cadou (2019) also performed velocity measurements of a turbulent free jet of air. Results agreed to hot-wire measurements and a velocity decay model if a certain distance from the jet exit was observed, although large uncertainties were reported. Bathel et al. (2020) used a carefully adjusted D-FLDI with parallel optical axes to probe a laser-induced breakdown shock wave and a conical hypersonic boundary layer with second-mode instabilities. Measured shock wave convection velocity was in close agreement to the reference obtained from simultaneous high-speed schlieren, and with lower uncertainty. Reasonable agreement was also verified for the velocity of the instability wavepackets, for which FLDI and high-speed

✉ Giannino Ponchio Camillo  
Giannino.PonchioCamillo@dlr.de

Alexander Wagner  
Alexander.Wagner@dlr.de

<sup>1</sup> German Aerospace Center (DLR), Institute of Aerodynamics and Flow Technology, Göttingen, Germany

schlieren were performed in different runs of the shock tunnel. Weisberger et al. (2020) presented FLDI velocimetry using a novel type of arrangement, in which a multi-point line FLDI is obtained. Convection velocity of laser-induced breakdown shock waves were reported with close agreement to high-speed schlieren measurements. Another novel methodology to obtain an array of FLDIs was used in Gragston et al. (2021b) to detect second-mode instabilities in the boundary layer on a flared cone. The obtained wavepacket convection velocities were within the expected range with respect to the nominal boundary layer edge velocity.

The accuracy and precision of velocimetry by means of double- or multi-foci FLDI depend on two main parameters. First, how well the two signals correlate, since the agreement between them informs the time lag to the velocity calculation. This depends on what proportion of the flowfield structures detected with the upstream system convect with little or no change until the downstream one. By taking into account the length scales of the probed flowfield, the distance separating the FLDI systems can be adjusted accordingly to improve signal agreement. The second parameter is how this distance is measured, as the quality of the obtained value is directly transferred to the velocity estimation. This was highlighted by Weisberger et al. (2020) concerning their measurements using adjacent channels of a multi-point line FLDI array, which yielded uncertainties in the order of  $\pm 10\%$ . In that same work measurements with  $\pm 0.9\%$  uncertainty were reported when using channels from separate lines, the difference being only how the spacing between the FLDI probes was determined. A similar occurrence is also seen in Ceruzzi and Cadou (2019) with the turbulent jet measurements, in which the separation between probes in the D-FLDI was given with  $\pm 6\%$  and the velocity measurements presented large error bars.

Three methods are currently established in the literature to obtain the separation distance between FLDI systems: directly imaging the beams with a beam profiler; gradually blocking the beams with a precision-controlled stopper (Weisberger et al. 2020); or analyzing the system response to a lens with large focal length crossing the path of the beams (Ceruzzi and Cadou 2019).

The beam profiler offers a direct and precise measurement, but is not applicable if the systems are not physically discrete, such as the line FLDI. Additionally, it may not be available in all laboratories due to its significant cost in comparison with common FLDI components. The beam-blocking approach also requires specific precision equipment, and was shown to present unsatisfactory precision. The lens response method is inexpensive, but time-consuming and also subject to higher uncertainties as will be further detailed in this work. Furthermore, the beam profiler and the lens methods rely on the existence of certain spatial clearance to accommodate either instrument dimensions or

their movement, which may prevent their application when the FLDI beams are positioned close to a surface, e.g., for boundary layer measurements. These difficulties are minor if beam separation measurements are performed in the preparation phase of an experimental campaign, with flexible time and physical constraints. However, the FLDI has a number of flexible parameters (positioning, differentiation axis, sensitivity, beam convergence, to name a few) which may be tuned or changed in the course of the experiments, as exemplified in Weisberger et al. (2020) and Siddiqui et al. (2021). Such adjustments require choosing and manipulating optical components, which may change the separation distance of the FLDI systems. An updated distance measurement is therefore required, in which the disadvantages of these methods may become relevant.

The present work introduces an alternative approach to measuring the separation distance between FLDI probes, while addressing the limitations pertaining to the current methodologies. The procedure is based on the detection of a propagating weak blast wave, generated with an electric spark in ambient air. The practical advantages analyzed in the present study and the preference for low-cost equipment of easy access are meant to render this technique easily applicable in other laboratories. The developments presented in the next sections are constrained to a double-foci FLDI, but can be directly extrapolated to arrays of more foci, regardless of whether they are optically discrete or continuous on the focal plane.

## 2 Theoretical background

### 2.1 Indirect estimation of FLDI parameters

Two parameters pertaining to FLDI diagnostics are relevant in this work. Namely, the small distance separating the two foci which make one FLDI, and the greater distance that separates two independent FLDI systems. For convenience, the former will be referred to as internal or  $\Delta x_1$  and the latter, external or  $\Delta x_2$ . Figure 1 shows a schematic of the FLDI used in this work and illustrates these distances. Accurate knowledge of the internal separation distance is necessary to correctly interpret the FLDI data, given its differential nature. The external separation is in turn useful when using multiple FLDI bundles to measure convection velocities by means of data cross-correlation.

Approaches to indirectly estimate these distances are valuable when the beams cannot be directly imaged with a beam profiler, e.g., due to hardware or spatial constraints. One such method is presented in Fulghum (2014) to obtain  $\Delta x_1$  by analyzing the FLDI response to a weak lens crossing its path along the axis of beam separation. The method

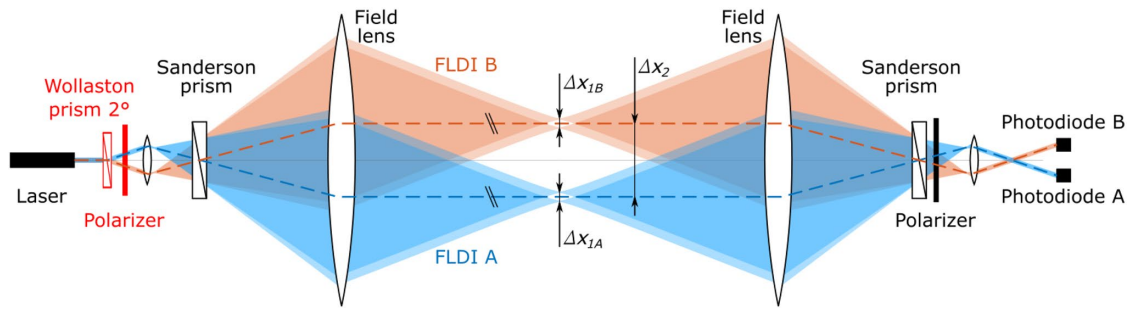


**Fig. 1** Schematic of a double-foci FLDI system with constant separation distance. Beams propagate from left (pitch-side) to right (catch-side). The two independent FLDIs are shown as different colors. Optical components required to duplicate the standard system are highlighted in red

was later extended to also obtain  $\Delta x_2$  in Ceruzzi and Cadou (2019).

The procedure consists of registering the D-FLDI output as a lens of long focal length (in the order of meters) is moved along the axis of beam separation. The output of each FLDI will describe a sinusoid when plotted as a function of the displacement of the lens. The period of the sinusoid depends on  $\Delta x_1$  and the focal length of the lens. The size and focal length of the lens can hence be chosen such as to provide at least one full sinusoid period when traversed across the path of the FLDI beams. With the D-FLDI, the sinusoids produced by each FLDI will be out of phase, due to the distance between them  $\Delta x_2$  as the moving lens is probed. The mathematical description of this behavior is summarized below in view of clarifying the terminology and relevant parameters for the present work.

If the FLDI response to the moving lens is normalized to have unitary amplitude, the corresponding sine wave when the lens moves along the  $x$ -axis can be described as:

$$y_n = \sin\left(\frac{2\pi}{T_n}x + \varphi_n\right) \quad (1)$$

with  $T_n$  and  $\varphi_n$  denoting the spatial period and the phase respectively, and  $n = A, B$  representing the two FLDIs. The dependence of  $T_n$  and  $\varphi_n$  with  $\Delta x_1$  and  $\Delta x_2$  is given by:

$$\Delta x_{1n} = \frac{\lambda_0 f_L}{T_n} \quad (2a)$$

$$\Delta x_2 = \frac{\bar{T}}{2\pi}(\varphi_A - \varphi_B) \quad (2b)$$

with  $f_L$  denoting the focal length of the weak lens and an average period  $\bar{T}$  employed to calculate  $\Delta x_2$ . This is a reasonable approximation because the two periods  $T_A$  and  $T_B$  are ideally identical, since in the type of D-FLDI configuration used here the optical piece controlling  $\Delta x_1$  is shared by the two FLDIs. An alternative to this approximation is to

cross-correlate the two sinusoids to find the spatial lag between them. However, a limited sample of sinusoid cycles resulting from the movement range of the lens can lead to considerable inaccuracy on the spatial lag estimation. The results in this work were obtained using Eq. (2b) to calculate  $\Delta x_2$ .

Another indirect approach to estimate  $\Delta x_1$  concerns the geometric disposition of the FLDI components. As detailed in Sect. 3.1, the internal separation distance originates from a divergence angle  $\varepsilon$  introduced in the FLDI beam at the focus of its field lens  $f_L$  on the emitting side. Assuming small angles, geometric optics yield simply  $\Delta x_1 = f_L \varepsilon$ . In this work, the divergence angle is produced by means of a Sanderson prism (Sanderson 2005), which consists of a bend-stressed polycarbonate bar. Following the approach in Biss et al. (2008), linear elastic theory can be used in combination with the properties of the prism material to estimate the resulting divergence angle introduced between the beams:

$$\varepsilon = \frac{\lambda}{f_\sigma} \frac{6E\delta b}{(Y^2 - 3L^2)} \quad (3)$$

with  $E$  the material modulus of elasticity,  $\delta$  the bending deflection,  $b$  the thickness of the bar and  $Y$  and  $L$  describing the bending supports as shown in Fig. 2. The fringe-stress coefficient  $f_\sigma$  is an optical property of the polycarbonate material measured using a light source of wavelength  $\lambda$ , with their ratio remaining constant for varying wavelengths.

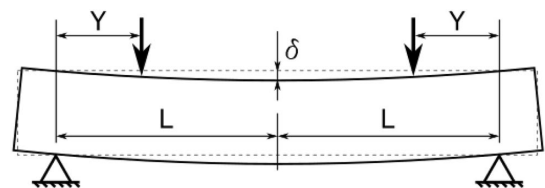


**Fig. 2** Schematic of the arrangement to generate a pure bending moment

## 2.2 Blast waves

A blast wave is originated in a fluid as a result of sudden movement, such as the expansion of high-pressure gases previously confined, or an instantaneous localized energy release. The pressure disturbance caused by such an event propagates away from its source with the local speed of sound. In ambient air, the elevated pressure is accompanied by an elevated temperature, which causes the local speed of sound to increase. With these portions of the disturbance propagating faster than their vicinity, a discontinuity is eventually formed as a shock wave front (Kinney and Graham 1985).

The velocity described by a moving shock wave is proportional to its strength. In the case of blast waves originated by localized events such as energy addition in a finite volume, the strength of the shock wave front will progressively become weaker due to volume divergence, dissipation and relaxation. As the blast wave loses strength, it eventually becomes an acoustic pulse, propagating approximately with the ambient sound speed. Even in this limit, it still retains a distinct pressure signature marked by a compression phase and an expansion phase. This waveform of unique shape and known convection speed offers ideal conditions for the experimental detection of distances. Nonetheless, this requires knowing at which point the blast wave is adequately approximated as an acoustic pulse.

An accurate physical simulation of the blast wave evolution is beyond the scope of this work. Instead, a simple formulation of blast wave convection velocity as a function of distance is pertinent. Specifically, the case of very weak blast waves, with  $M \approx 1$  no more than a few centimeters from the source will be of interest.

Jones et al. (1968) proposed a simple theoretical model to estimate the trajectory of the blast wave generated by a lightning discharge. The model is based on the strong shock similarity solution for a cylindrical shock wave, first-order corrected for the weak shock limit<sup>1</sup>. It will be shown in Sect. 4.2 that for the spark-generated disturbance in this work, the region with significant gradient of blast wave propagation velocity is confined to the vicinity of the source (distances of same order of magnitude as the length of the

spark). Therefore, assuming the shock wave to be cylindrical is reasonable when considering the blast wave trajectory estimation.

The trajectory of the shock wave front is described in terms of radius  $R$  and arrival time  $t$ . The undisturbed speed of sound  $c_0$  and a characteristic radius  $R_0$  are used to non-dimensionalize  $R$  and  $t$  as  $x = R/R_0$  and  $\tau = c_0 t/R_0$ , respectively. The characteristic radius is defined as:

$$R_0 = \sqrt{\frac{4E_0}{\gamma B P_0}} \quad (4)$$

with  $\gamma$  the specific heat ratio (assumed constant),  $P_0$  the undisturbed ambient pressure,  $E_0$  the energy deposited per unit length and  $B = 3.94$  a constant for air. The trajectory for the weak shock is described as:

$$\tau = \frac{1}{2} \left( \sqrt{1 + 4x^2} - 1 \right) \quad (5)$$

Equation (5) can be used to obtain an analytic expression for the dimensional shock wave convection velocity  $U_s = dR/dt$  as a function of the distance to the blast wave source  $R$ , as:

$$U_s = c_0 \frac{\sqrt{1 + 4(R/R_0)^2}}{2R/R_0} \quad (6)$$

In this equation, the only unknown parameter is  $R_0$ , which is determined by the energy addition  $E_0$  following Eq. (4). An experimental method to obtain  $E_0$  will be shown in Sect. 4.2.

## 3 Experimental setup

### 3.1 Double-foci FLDI

The D-FLDI arrangement used in this work is shown schematically in Fig. 1. The laser source is a 200 mW Oxixus LCX-532S DPSS laser with nominal wavelength 532.3 nm. As mentioned in Sect. 2.1, Sanderson prisms are used to split the beams into interferometric pairs. The prismatic bar is a 6 mm thick Makrolon<sup>®</sup> bent with  $L = 85$  mm and  $Y = 29$  mm (refer to Fig. 2). Light intensity after beam recombination is measured using Thorlabs DET36A2 photodetectors, terminated with  $50\Omega$ . The outputs from the photodiodes were amplified 25 times using a SRS SR445A DC-350 MHz preamplifier. All data presented in this work were recorded for 1 ms using an AMOtronics transient recorder with DC-coupling and a sampling rate of 100 MHz.

The FLDI presented here has been designed to operate in the HEG shock tunnel (DLR 2018). The free gap between the field lenses is approximately 3.8 m. The beams are expanded to approximately 45 mm diameter at the field

<sup>1</sup> Bach and Lee (1970) proposed a more complex model, derived from the Navier–Stokes equations assuming a power law for the density profile behind the shock wave. Although this is not the case for the weak shock limit, the authors highlight that the obtained shock trajectory would remain accurate in the limit due to the conservation of total mass and energy. The solution obtained through this method has been compared to the one from the approach of Jones et al. (1968), yielding identical results for trajectory. For simplicity, the approach from Jones et al. (1968) is retained in this work.

**Table 1** Sanderson prism deflections (measured) and corresponding beam divergence angles (estimated from linear elastic theory) investigated in the present work, separated by method and scope

Method	Scope	$\delta$ [mm]	$\epsilon$ [arc min]
Beam profiler	$\Delta x_1, \Delta x_2$	0.25, 0.40, 0.55, 0.70, 0.90, 1.10, 1.40	0.42, 0.58, 0.75, 0.92, 1.14, 1.36, 1.69
Moving lens	$\Delta x_1, \Delta x_2$	0.30, 0.59, 0.95, 1.45	0.47, 0.79, 1.19, 1.75
Blast wave	$\Delta x_2$	0.30, 0.59, 0.95, 1.45	0.47, 0.79, 1.19, 1.75
Linear elastic theory	$\Delta x_1$	0.00 to 1.80 (continuous)	0.14 to 2.14

lenses, which have a diameter of 100 mm and focal length 500 mm.

Eleven different values of Sanderson prism deflection were used, allowing flexibility of separation between the orthogonally polarized components in the range of  $70 \leq \Delta x_1 \leq 250 \mu m$ . When adjusting the prism deflection, bending was always applied past the intended value and then returned to it, to avoid hysteresis following Biss et al. (2008). The prism deflections  $\delta$  were measured with a deflection gauge with 0.01 mm precision. The investigations were separated into indirect evaluation using a lens with focal length 3 m and the present blast wave method (4 points), and direct measurement using a DataRay TaperCamD-UCD23 beam profiler (7 points) as detailed in Table 1. The table also shows the beam divergence angles corresponding to the Sanderson prism deflection values, for reference. These angles are estimates from linear elastic theory, including a vertical offset due to residual stress to be seen in Sect. 4.1.

Prior to blast wave measurements, the undisturbed response of the FLDI was adjusted to approximately half-way between its lowest and highest output, where sensitivity is at its maximum. This was accomplished by fine adjustment of the relative position of the Sanderson prism on the catch-side along the axis of beam separation. When the beam-splitting optics is manipulated in this way, the phase difference between the resulting colinear beams changes. Since the interferometer is adjusted to an infinite fringe configuration, this results in a uniform intensity change after the beams are made to interfere with the polarizer before the photodiode. This approach is present in Lawson et al. (2019), only using Wollaston prisms instead of Sanderson. Conversion of voltage produced by the photodetectors into phase difference was also performed following that work.

Duplication of the basic FLDI into two or more closely spaced systems can be achieved in many different ways (Ceruzzi and Cadou 2019; Jewell et al. 2019; Bathel et al. 2020; Weisberger et al. 2020; Gragston et al. 2021a). In the present work, the D-FLDI is produced by means of a Wollaston prism of  $2^\circ$  splitting angle together with a polarizer, highlighted in red in Fig. 1. In this approach, the prism splits the incoming beam into two diverging beams with orthogonal polarization. The accompanying polarizer is oriented to

project the beams back into the original polarization plane, such that the remainder of the system operates identically to the single FLDI arrangement. With both the original beam and the polarizer oriented at  $45^\circ$  with respect to the fast axis of the prism, two systems with identical power are obtained.

The duplicated system is obtained regardless of the precise positioning of the pair prism-polarizer on the pitch-side, as long as it is placed before the pitch-side Sanderson prism. Depending on its position with respect to the expanding and field lenses on the pitch-side and their focal lengths, multiple values of bundle separation  $\Delta x_2$  at the D-FLDI center plane can be achieved with the same Wollaston prism, which can be advantageous in investigations aiming at, e.g., comparing spectral amplitudes between multiple points. A novel approach following this objective with a grid of FLDIs is presented in Gragston et al. (2021a).

However, this flexibility comes at the cost of allowing the two FLDI systems to describe non-parallel trajectories between the field lenses, as their axes will cross either before or after the focal length of the pitch-side field lens for all but one specific position of the splitting prism-polarizer pair. This way, the separation between the systems  $\Delta x_2$  will vary along the probing region, which must be considered when using the duplicated FLDI setup to perform flowfield velocity measurements. Since the signal obtained on each FLDI is an integration of flowfield disturbances across the probing volume, disturbances crossing the FLDIs at stations with different values of  $\Delta x_2$  may bias the velocity measurement.

To avoid this, a parallel disposition of FLDI bundles is recommended in velocimetry applications, as highlighted in Bathel et al. (2020). In that work, a Nomarski prism was used to ensure parallelism between the FLDIs. This type of birefringent prism works similarly to the Wollaston prism used here, but redirects the output beams so that they cross at a point ahead of it. Parallelism between the two FLDIs is thus achieved by adjusting this crossing point to be at the focal length of the pitch-side field lens, i.e., to coincide with the Sanderson prism on the left in Fig. 1.

In the present work, a similar effect is achieved by combining the Wollaston prism with the convergent lens responsible for expanding the beams in the FLDI on the pitch-side. The precise position and focal length of the expanding lens

are predefined by a combination of other parameters in the FLDI, namely the focal length of the field lens, the desired distance between the field lenses and the desired maximum beam diameter. Once this is set, the position of the Wollaston prism with respect to the expanding lens is determined using geometric optics such that the image of the origin of the two output beams coincides with the location of the pitch-side Sanderson prism in the setup. The center axes of each FLDI generated using this approach are shown in Fig. 1 as dashed lines with the corresponding colors.

For system design purposes, an initial estimate of the resulting  $\Delta x_2$  as a function of the position of the optical elements and the splitting angle of the Wollaston prism can be obtained through trigonometric relations. Once all components are in place, a more precise measurement of the final  $\Delta x_2$  such as the procedure proposed in this work is essential to minimize errors in the velocity measurements.

### 3.2 Blast wave generation

The FLDI  $\Delta x_2$  measurement methodology proposed in this work requires a known and repeatable density disturbance to cross the optical axis of the FLDI systems. This is achieved in a simple manner through a spark in ambient air at rest. In contrast to past works which have successfully used laser-induced breakdown sparks to study the FLDI response (Parziale 2013; Bathel et al. 2020; Weisberger et al. 2020), an electric discharge is used here. The advantages for the purpose of the current work are high positioning flexibility with reduced cost and safety risks, while producing a blast wave with as little strength as possible with good repeatability.

The weak disturbance is preferred here because the convection velocity of an expanding blast wave varies as it propagates, but tends asymptotically to the ambient speed of sound, as seen in Sect. 2.2. The premise is to use the known value of this lower bound to obtain the separation between the FLDI bundles from the time lag between the signals. Therefore, it is advantageous that the blast wave is weak enough to degenerate into an acoustic pulse as close as possible to the source, hence minimizing the required physical space and the influence of external factors. Furthermore, the spark generation in ambient air without requiring any specific environmental conditioning is aimed at facilitating the application of the method. Only the ambient temperature is required to determine the local speed of sound.

The electric spark is obtained by means of an automotive spark plug. The distance between the electrodes of the spark plug is increased to approximately 4 mm such that the resulting blast wave produces the necessary amplitude of density fluctuations to be detected with the FLDI. A schlieren image of the spark-generated blast wave is shown in Fig. 3.

To study the evolution of the blast wave trajectory and determine the distance from the source beyond which the

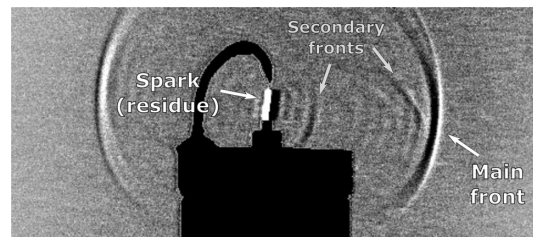


**Fig. 3** Enhanced schlieren image of the blast wave generated using an automotive spark plug

propagation velocity is  $M \approx 1$ , the spark plug setup is installed on a translating mount with 0.1 mm precision. This allows the blast wave source to move along the axis of separation between the FLDI bundles, while the FLDI setup remains untouched. The combined uncertainty of operator and hardware to control this movement was estimated as  $\pm 0.25$  mm. The origin of the mount places the center of the gap between the electrodes approximately at the middle point between the two FLDIs. This was manually adjusted in a much coarser manner, with uncertainty in the order of 1 mm. Given the sensitivity of the theoretical velocity distribution to the origin of the blast wave, the vector of measurement positions is allowed to be uniformly offset by an optimization algorithm when processing the results, as will be detailed in the next section.

Measurements were taken at 23 positions corresponding to nominal distances between spark source and FLDI probe of 3 mm to 50 mm. The spacing between adjacent probing positions was made smaller closer to the source, where the velocity gradient is larger. The spark plug was controlled to produce a single spark during the recording time, allowing the disturbances to fully dissipate between discharges. Ten blast waves were generated and recorded at each position. The lowest and highest observed time lags were discarded, and the remaining 8 were individually analyzed. The ambient temperature near the probing region was measured with a digital ambient thermometer with precision of 0.05°C before each series of measurements to calculate the ambient sound speed. When the sound speed is used in Sect. 4.2 to determine  $\Delta x_2$ , the uncertainty carried over from the temperature measurement is less than 0.01% and will therefore be neglected.

## 4 Results and discussion

### 4.1 Estimation of distances with existing methods

An example of the results following the procedure described in Sect. 2.1 is shown in Fig. 4. The data were obtained

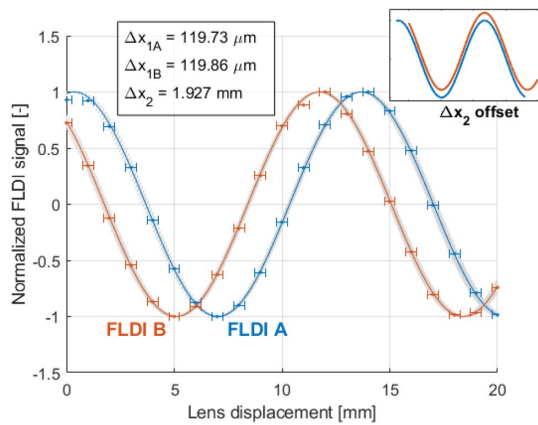


**Fig. 4** Normalized double-foci FLDI response to a moving lens. Dots with error bars denote the acquired datapoints and lines correspond to least-square fits of sine functions. Shaded areas around the sinusoids are possible fits considering randomized errors along the lens displacement points. Resulting  $\Delta x_1$  and  $\Delta x_2$  measurements are displayed in the textbox. The inset shows the result of horizontally offsetting one of the sinusoids by  $\Delta x_2$ , ideally causing the two lines to overlap. They are also vertically offset by 10% for clarity. Data corresponding to Sanderson prism deflection  $\delta = 0.59$  mm

using the D-FLDI described in Sect. 3.1 with Sanderson prism deflection  $\delta = 0.59$  mm and a lens with focal length  $f_L = 3$  m. The horizontal error bars correspond to the  $\pm 0.25$  mm combined uncertainty of operator and hardware to control the lens position, which was performed using the same supporting mount used for the spark generator described in Sect. 3.2.

The period and phase of the sine functions in the form of Eq. (1) are determined using least-squares method on the normalized FLDI output. A Monte Carlo approach is adopted to estimate a representative uncertainty for the fitted sinusoids as follows. Uniformly randomized errors on the lens displacement values within the assumed uncertainty of  $\pm 0.25$  mm are used to calculate 10,000 scenarios. The same modified lens displacement vector is used for both FLDIs in any given case, since the separation distance between them is constant and independent of this uncertainty. From the obtained distribution of periods and phases, an average sinusoid is obtained for each FLDI (blue and red lines in Fig. 4). An idea of the variation of the fits is given by the shaded area around each line, composed of 1000 different results from the Monte Carlo simulation. Values for  $\Delta x_1$  and  $\Delta x_2$  calculated using Eq. (2) with the average  $T_n$  and  $\varphi_n$  are shown in the textbox. Finally, the inset plot displays the two average sinusoids when one of them is offset in the x direction by the calculated  $\Delta x_2$ . An additional offset in the y direction is introduced for clarity, otherwise the lines are indistinguishable. The precise overlapping in terms of both

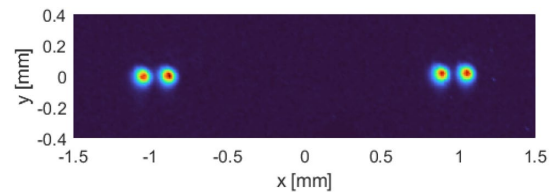


**Fig. 5** Beam profiler image of the D-FLDI of the present work. Image obtained with Sanderson prism deflection  $\delta = 0.9$  mm

phase and period is a validation of the physical assumptions of this methodology.

The distribution of period  $T_n$  and phase  $\varphi_n$  values obtained with the Monte Carlo approach are used to estimate the uncertainties for the calculated  $\Delta x_1$  and  $\Delta x_2$  given uncertainties for period  $T$  and phase difference  $\Delta\varphi = \varphi_A - \varphi_B$  yields:

$$\sigma_{\Delta x_{1n}} = \frac{\lambda_0 f_L}{T_n^2} \sigma_{T_n} \quad (7a)$$

$$\sigma_{\Delta x_2} = \sqrt{\left(\frac{\Delta\varphi}{2\pi} \sigma_{\bar{T}}\right)^2 + \left(\frac{\bar{T}}{2\pi} \sigma_{\Delta\varphi}\right)^2} \quad (7b)$$

For the example shown in Fig. 4, Eq. (7) gives  $\sigma_{\Delta x_{1A}} = 0.86 \mu\text{m}$ ,  $\sigma_{\Delta x_{1B}} = 0.75 \mu\text{m}$  and  $\sigma_{\Delta x_2} = 0.11$  mm. Hence the  $\Delta x_1$  obtained for the two FLDIs shown in the textbox in Fig. 4 is the same within the uncertainty bounds, which is expected and validates the approach of using an average  $\bar{T}$  in Eq. (2b). It is also noted that the uncertainty of  $\Delta x_2$  is proportionally much larger than that of  $\Delta x_1$ . This is a consequence of the lens displacement uncertainty having a much greater influence on the phase of the sine wave than on its period, as can be inferred from the shaded regions in Fig. 4.

Complementary to the beam distance measurements performed with the moving lens, the FLDI beams were imaged at the center plane of the D-FLDI using a beam profiler. An example of the obtained image is given in Fig. 5, for Sanderson prism deflection  $\delta = 0.9$  mm. The resolution of the beam profiler was in situ calibrated as  $10.3 \mu\text{m}$  per pixel. Distances  $\Delta x_1$  and  $\Delta x_2$  were measured by detecting the peak values of profiles resulting from averaging the pixel intensities along each vertical line of the images. Ten independent images were obtained for each Sanderson prism deflection. To achieve sub-pixel accuracy, the average pixel intensity profile of each independent image was interpolated using a shape-preserving cubic interpolation and smoothed using a moving average. The pixel difference between the peaks identified in the resulting profiles was then converted to

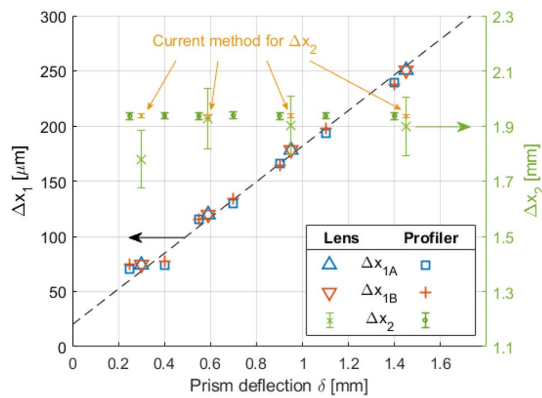


**Fig. 6** Values for FLDI  $\Delta x_1$  (left y-axis) and  $\Delta x_2$  (right y-axis) measured using the moving lens method and beam profiler images for multiple adjustments of Sanderson prism deflection  $\delta$ . The dashed line indicates the linear elastic theory prediction, vertically offset to best fit the data. The values for  $\Delta x_2$  obtained with the method suggested in this work are also shown for comparison

distances and used to calculate a mean value and standard deviation.

By changing the deflection of the Sanderson prism  $\delta$  and repeating the procedures described above, the dependency of  $\Delta x_1$  with the prism deflection  $\delta$  can be demonstrated. Figure 6 shows the results of this calibration for multiple values of  $\delta$ , with  $\Delta x_1$  plotted on the left y-axis and  $\Delta x_2$  on the right one. The expected results are that  $\Delta x_1$  linearly increases with the prism deflection  $\delta$ , while  $\Delta x_2$  remains unchanged since it is not defined by the Sanderson prism settings. The linear elastic theory estimate for  $\Delta x_1$  is obtained from Eq. (3), using the optical properties for polycarbonate mentioned in Biss et al. (2008), namely  $f_\sigma = 7.0 \text{ kN/m}$  for  $\lambda = 546.1 \text{ nm}$ , and the mechanical properties of Makrolon<sup>®</sup> following the manufacturer datasheet,  $E = 2.4 \text{ GPa}$ . A small vertical offset is introduced in the theoretical prediction to account for the trend of an apparent finite  $\Delta x_1$  with  $\delta = 0$ . This may be due to a residual stress field in the prism, as highlighted in, e.g., Fulghum (2014) and Birch et al. (2020).

The results show that  $\Delta x_1$  has a similar behavior for both FLDIs, with values that coincide for a given  $\delta$  and which are well described by the correlation obtained using linear elastic theory once an empirical estimate of residual stress offset is taken into account. Uncertainties for  $\Delta x_{1A}$  and  $\Delta x_{1B}$  for both the lens and profiler methods have similar magnitude as presented for the example above (order of  $1 \mu\text{m}$ ), and are not plotted for clarity. A comparatively low accuracy of the beam profiler results is observed for the lower end of  $\delta$  values. This is a result of inadequate pixel density of the instrument to detect beams this close together, making them harder to distinguish.

Regarding  $\Delta x_2$ , the distribution of values calculated through the moving lens method admits the definition of a horizontal line that crosses all points within their uncertainty. Such a line would confirm the expected behavior of  $\Delta x_2$  not depending on the Sanderson prism configuration. However, a noticeable fluctuation among the calculated values of  $\Delta x_2$  can be observed, even though they all yielded a similar good signal overlap as seen in the inset of Fig. 4 (not shown). Together with the relatively large error bar of each obtained value (approximately  $\pm 6\%$ ), concern is warranted as the uncertainty in  $\Delta x_2$  is directly fed through to the measurement of velocities using the D-FLDI. One way to lower this uncertainty is to collect more independent sinusoid sweeps, such as to obtain a reliable mean of  $\Delta x_2$  with an associated standard deviation. Another way is to address the large uncertainty of each calculated  $\Delta x_2$ , by reducing the influence of the lens displacement uncertainty on the sinusoidal fits. This may be accomplished by either reducing the uncertainty of each point (e.g., with careful operator action) or by using more points on each sweep. All these alternatives, however, significantly add effort to a procedure that is already inherently time-demanding.

Looking at the  $\Delta x_2$  estimates from the beam profiler images, a much more consistent distribution is observed. The uncertainty of each point is significantly smaller than the moving lens results, at  $\pm 0.6\%$ . Also, the mean values remain unchanged for different values of Sanderson prism deflection, with a mean of  $\Delta x_2 = 1.937 \pm 0.001 \text{ mm}$ . For a direct comparison, the results obtained with the method presented in this work are also highlighted in Fig. 6. Excellent agreement to the beam profiler results can be verified. The details pertaining to these measurements are presented in the next section.

#### 4.2 Estimation of distances through blast wave detection

An alternative to the procedures exemplified in Sect. 4.1 is presented in this section. A blast wave is used as a means to produce a disturbance with clear signature on the FLDI response. The main objective here is to measure  $\Delta x_2$  with low effort and increased precision, addressing the issues highlighted previously.

A sample of blast wave detection using D-FLDI is shown in Fig. 7. For ease of operation in the experimental setup, FLDI B is upstream of FLDI A with respect to the blast wave source, but equivalent results may be obtained inverting the disposition of source and probe. The D-FLDI response is minimally post-processed to values of phase difference  $\Delta\Phi$ . The time axis is arbitrarily offset to yield  $t = 0$  when the blast wave arrives at FLDI B, since the method explored in this section is independent of the blast wave travel time upstream of the first FLDI bundle. The clear shape described

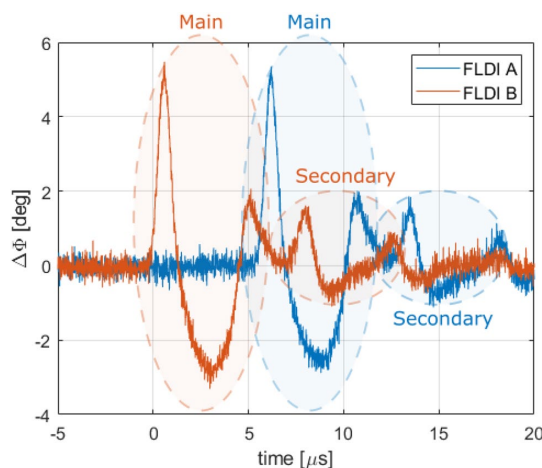


**Fig. 7** Blast wave detection using the double-foci FLDI. Spark generator is 30 mm from FLDI B, which is upstream of FLDI A. Main and secondary events are highlighted. The origin of the time axis is arbitrarily offset to match the blast wave arrival at the position of FLDI B. Data corresponding to Sanderson prism deflection  $\delta = 0.95$  mm

by the blast wave detection on each FLDI indicates that an accurate estimate of time lag can be obtained as a peak in the cross-correlation between the signals.

It is also noteworthy that the signal detected with each FLDI is almost identical but for the time lag. This is expected since the blast wave does not undergo significant changes between the closely spaced FLDI probes, unless very close to the spark source. Nonetheless, the multiplication of FLDI beams requires the addition of system components and complexity. The quality and sensitivity of the resulting double- or multi-foci FLDI may not be identical, and hard to quantify. The controlled disturbance produced with the electric spark may therefore be used as a reference to identify potential issues that may need addressing.

In Fig. 7, secondary events are observed in the time signals occurring after the passage of the main blast wave. These events correspond to interactions between the blast wave and the spark plug structure, as can also be seen in the schlieren image of Fig. 3. Events of this nature were verified to have been strong enough at certain stations to bias the cross-correlation of the signals if included. Nonetheless, they were always sufficiently separate from the main blast wave signature to be easily discarded from the signals prior to cross-correlation, hence not interfering with the results presented here.

It should be noted that cross-correlating the signals to obtain the time lags is preferred for robustness. By taking into account the full signature of the blast wave on the FLDI probes, the lag measurement becomes less sensitive to eventual flowfield non-uniformities or signal-to-noise-ratio

issues. Nonetheless, time lags may also be obtained with simpler approaches, such as measuring the time difference between the signal peaks. This is an alternative if the signature from the blast wave is not as easily isolated from secondary events as shown here. An example is if the FLDI probes are positioned with respect to the surface of a model at a certain distance which is not large enough to allow the reflected wave to arrive significantly later than the main one, nor small enough for the main and reflected wavefronts to merge together before reaching the FLDI probes (Kinney and Graham 1985).

Since the blast wave propagates with increased speed near the source and the D-FLDI is kept unchanged, the obtained time lags increase as the source is moved away from the D-FLDI. When the time lags stabilize around a certain value, an indication is obtained that the acoustic limit of the blast wave was reached, in which it propagates with  $M \approx 1$ . For a more accurate prediction of this region, Eq. (6) is used to obtain the analytic distribution of wave convection velocity. In this equation, a single unknown determines the trajectory of the wavefront, namely the energy deposited by the spark  $E_0$ , which defines  $R_0$  through Eq. (4). Since the distance between the two FLDIs is the same for all blast wave probings, the spark energy can be obtained using the detected distribution of time lags without explicit knowledge of the distance  $\Delta x_2$ , as the solution for an optimization problem as follows.

In a D-FLDI constructed as presented in this work and considering the very weak blast wave produced, the velocity gradient between the two FLDI bundles will generally be small enough to be neglected without incurring an excessive error. This way, at each probing location  $R_i$  (measured with respect to the blast wave source) the distance  $\Delta x_2$  will be given as a function of the time lag  $\Delta t_i$  as  $\Delta x_2 = U_s(R_i) \cdot \Delta t_i$ , with the blast wave velocity  $U_s$  a function of  $R_i$  (and  $E_0$ ) according to Eq. (6).

Because  $\Delta x_2$  is kept constant as the blast wave source is moved away, the product between the theoretical  $U_s$  and the experimental  $\Delta t$  must remain constant for all measurement locations  $i = 1, \dots, n$  when the correct value of  $E_0$  is used. In other words, the derivative of  $U_s(R_i) \cdot \Delta t_i$  with respect to the radial coordinate  $r$  must be zero. The numerical optimization problem hence becomes finding  $E_0$  that minimizes the objective function  $f$  composed by the quadratic sum of these derivatives:

$$f(E_0) = \sum_{i=1}^n \left[ \frac{d}{dr} (U_s(R_i) \cdot \Delta t_i) \right]^2 \quad (8)$$

The derivative in each point  $R_i$  is roughly approximated through the mean value theorem, by means of finite differences between  $R_{i-1}$  and  $R_{i+1}$ . This is a reasonable approach because the distribution of velocities and time lags along

the radial coordinate is expected to describe a well-behaved function. This is further conditioned by using for each location the average of time lags obtained with the independent measurements, denoted above with the bar over  $\Delta t_i$ .

As mentioned in Sect. 3.2, the origin of the position vector was manually adjusted to roughly place the spark generator at the middle point between the two FLDIs. However, the theoretical velocity distribution Eq. (6) is highly sensitive to the accuracy of this origin to adequately capture the region of stronger velocity gradients. Therefore, a second optimization layer was introduced in the algorithm, allowing a systematic offset of the position vector to be adjusted. This layer was placed above Eq. (8), searching for the value of position vector offset which minimized the standard deviation of the distances calculated as  $U_s(R_i) \cdot \bar{\Delta t}_i$  resulting from the inner optimization layer. This target is sustained by considering that the perfect representation of the data by the theoretical curve should yield the exact same  $\Delta x_2$  on all points. A schematic representation of the full algorithm is shown in Fig. 8. Although this double-layer procedure yields a noticeable improvement on the overlapping of experimental data and theoretical model, adequate results can also be obtained without the second (outer) optimization layer, with the resulting  $\Delta x_2$  having been observed to vary by a maximum of only 0.7%.

Once a value of energy deposition  $E_0$  is found, the blast wave velocity as a function of its radius is determined. An estimate of the separation distance between the FLDI bundles  $\Delta x_2$  can hence be obtained from any of the query points using the local velocity and the measured time lag. To demonstrate the method and provide an idea of precision, the values of  $\Delta x_2$  reported here are obtained as an average between all points collected for each Sanderson prism configuration:

$$\Delta x_2 = \frac{1}{n \cdot m} \sum_{i=1}^n \sum_{j=1}^m (U_s(R_i) \cdot \Delta t_{i,j}) \tag{9}$$

where  $i = 1, \dots, n$  denotes the measurement positions as before, and  $j = 1, \dots, m$  represents the individual measurements performed at each position. With a total number of 184 independent measurements in each series ( $n = 23$  positions,  $m = 8$  measurements at each position), the standard deviation of the  $\Delta x_2$  values is used as an estimate of uncertainty.

An example of the measurements and resulting calculated blast wave trajectory is shown in Fig. 9. The solid line represents Eq. (6) calculated using  $E_0$  obtained from minimizing Eq. (8). The dots with error bars are the means and standard deviations of Mach numbers calculated using the experimental time lags and the separation distance  $\Delta x_2$  calculated with Eq. (9). The horizontal error bars indicate the  $\pm 0.25 \text{ mm}$  position uncertainty mentioned in Sect. 3.2.

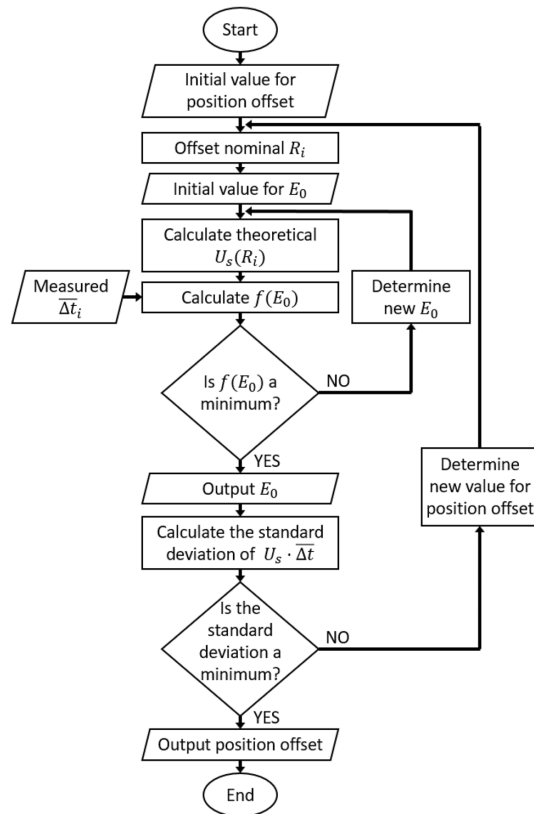
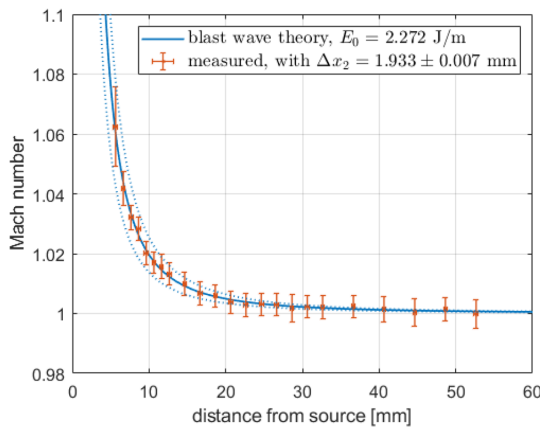


Fig. 8 Fluxogram of the double-layered algorithm to calculate the best theoretical fit to the experimental data. The  $f(E_0)$  used in the inner layer is defined by Eq. (8)

The dotted lines in Fig. 9 are the blast wave trajectories obtained with variation of  $\pm 30\%$  on the calculated  $E_0$ . The small influence of such a large difference shows that the accuracy of the energy deposition estimate is not a determinant factor for the D-FLDI parameter estimation studied here.

This procedure was repeated for the same Sanderson prism configurations used with the moving lens method. The obtained values of  $\Delta x_2$  are reported in Table 2. Two important results can be highlighted in this table. First, the obtained values for  $\Delta x_2$  are essentially the same across all different  $\delta$  (hence  $\Delta x_1$ ) as they should, and all agree with the beam profiler measurements to within 0.2% (refer to Fig. 6). Second, the standard deviation in all cases corresponds to less than 0.5% of  $\Delta x_2$ , i.e., a very consistent value of  $\Delta x_2$  is obtained across all measurement points. Hence a precise measurement of  $\Delta x_2$  can be performed by using time lags detected in a single position, as long as the blast wave local convection velocity is known.



**Fig. 9** Blast wave trajectory regressed from FLDI measurements. Solid line indicates the analytic solution using the  $E_0$  value obtained from the optimization procedure. Dotted lines indicate the solutions for  $\pm 30\%$  on the nominal  $E_0$ . Measured Mach numbers obtained from the time lags detected with D-FLDI, considering the separation distance indicated in the legend. Data corresponding to Sanderson prism deflection  $\delta = 0.59$  mm

**Table 2** Measured FLDI beam separation distances  $\Delta x_2$  for different Sanderson prism deflections  $\delta$

Sanderson prism $\delta$	Double-foci FLDI $\Delta x_2$
0.30	$1.937 \pm 0.008$
0.59	$1.933 \pm 0.007$
0.95	$1.937 \pm 0.006$
1.45	$1.935 \pm 0.004$
	Mean: 1.936

All units in mm

An adequate estimate of the velocity in the vicinity of the blast wave source can only be obtained with measurements at multiple locations, e.g., by means of the optimization procedure described here. Nonetheless, Fig. 9 shows that such an elaborate estimate is not strictly necessary. The sonic limit beyond which  $M \approx 1$  is reached still relatively close to the source, for the case investigated here in which an automotive spark plug is the source of the blast wave. Farther than approximately 20 mm from the source, the blast wave convection velocity can be approximated as  $M = 1$ , requiring no further measurements. Processing in this simplified way the collection of measurements used to obtain Table 2 yielded no more than 0.5% difference to the beam profiler mean measurement, with standard deviations ranging from 0.2% to 0.7% in the upper limit of 95% confidence interval. Even if the experimental constraints force a measurement very close to the source, Fig. 9 indicates that

assuming  $M = 1$  to calculate the beam separation distance from the signal time lags introduces no more than 3% error as close as 10 mm. Finally, if in addition to the approximation of  $M = 1$ , the time lags were obtained simply using the peaks of the signals instead of cross-correlation, as previously mentioned, the obtained differences to the beam profiler measurements were still 1% or less for distances to the spark source larger than 20 mm.

The method suggested here is therefore capable of providing a good experimental estimate of the beam separation distance  $\Delta x_2$  of a double- or multi-foci FLDI with very low effort. The acquisition of repeated blast wave measurements at some location within the sonic limit region is quick and requires little mechanical preparation, with the whole process taking only a few minutes.

As a side note, the blast wave measurements can be further used to give an approximate estimate of the internal separation distance  $\Delta x_1$  as follows. For any given distance from the source, the magnitude of the FLDI signal  $\Delta\Phi$  will be proportional to the separation distance between the interferometric pair  $\Delta x_1$ . As long as this separation is kept small relative to the waveform of the blast wave, the ratio  $\Delta\Phi/\Delta x_1$  is constant. It is an approximation of the spatial derivative of the disturbance, which remains unchanged between measurements if the source and the measurement location are the same. This way, if the separation  $\Delta x_1|_{\delta_1}$  is known for one Sanderson prism deflection  $\delta_1$ , the separation for other configurations  $\delta_k$ ,  $k = 2, 3, \dots$  can be obtained by matching the magnitude of the measured  $\Delta\Phi|_{\delta_k}$ , i.e.,  $\Delta x_1|_{\delta_k} = \Delta\Phi|_{\delta_k}/(\Delta\Phi/\Delta x_1)|_{\delta_1}$ . However, at least one known value of  $\Delta x_1$  is still required, and uncertainties are difficult to assess. Nonetheless, Fig. 4 in Sect. 4.1 has shown that linear elastic theory provides direct and reasonable estimates of this distance when a Sanderson prism is employed to produce  $\Delta x_1$ , requiring only a pre-strain offset to be adjusted. Once this is accomplished, it becomes a good practical substitute for the lens procedure if needed. The measurement of  $\Delta x_1$  through blast wave detection is therefore only recommended for verification purposes.

## 5 Conclusion

The contributions presented in this work addressed a new methodology of indirect estimation of the distance separating the probing volumes of a double-foci FLDI,  $\Delta x_2$ . A weak blast wave generated in ambient air at rest using an automotive spark plug was shown to become an acoustic pulse close to its source. The known convection velocity of this type of disturbance, namely the ambient sound speed, was used to obtain  $\Delta x_2$  from the time lag between the adjacent systems.

An analysis comprising a wide range of measurement locations showed that reliable and accurate estimates with

as little as  $\pm 0.4\%$  uncertainty ( $2\sigma$ ) can be obtained from multiple measurements in a single location, which is easily and quickly executed. Comparison to direct measurements using a beam profiler showed differences smaller than 0.5% if a single location was used farther than 20 mm from the spark source, and less than 0.2% if multiple stations are combined. The measurements were shown to be consistent throughout multiple configurations of the FLDI Sanderson prism, which controlled the unrelated separation between the interferometric pair composing one FLDI,  $\Delta x_1$ .

The existing method of indirect assessment of beam separation distances using the FLDI response to a lens with large focal length was critically evaluated. Results corroborated its excellent ability to measure  $\Delta x_1$ . However, for  $\Delta x_2$  the lens method yielded measurement uncertainties of  $\pm 6\%$ , together with a considerable variation of the mean results (up to 5%) when  $\Delta x_1$  was varied by means of Sanderson prism adjustment.

Velocimetry by means of FLDI measurements is only as accurate and reliable as the measurement of the separation distance between the FLDI systems  $\Delta x_2$ . The present method is therefore recommended as a means to obtain this value in double- or multi-foci FLDI. It preserves the low-cost benefit of the moving lens indirect approach while being much less time-consuming with improved accuracy and precision, both comparable to direct beam imaging. Additionally, it requires very little free space (20 mm length ideally, less if necessary), being more practical than a beam profiler in case of limited spatial availability such as in the proximity of model walls. Also, the non-imaging nature of this method makes it applicable to multi-point FLDI systems in which the foci are not optically separated.

Finally, it is worth noting that once the blast wave decays to an acoustic pulse, it propagates with little change between closely spaced FLDI probes. Being a simple, well-known and easily reproduced type of disturbance, it may therefore be a helpful reference for system response verification in multi-foci FLDI.

**Acknowledgements** The support given by Prof. Dr. Klaus Hannemann and Prof. Dr. Peter J. Klar is deeply appreciated. The authors also wish to acknowledge the assistance of the HEG team, in particular Ingo Schwendtke, Uwe Frenzel, Fabian Glasewald, Jan Martinez Schramm and Divek Surujhlal.

**Funding** Open Access funding enabled and organized by Projekt DEAL.

**Open Access** This article is licensed under a Creative Commons Attribution 4.0 International License, which permits use, sharing, adaptation, distribution and reproduction in any medium or format, as long as you give appropriate credit to the original author(s) and the source, provide a link to the Creative Commons licence, and indicate if changes were made. The images or other third party material in this article are included in the article's Creative Commons licence, unless indicated otherwise in a credit line to the material. If material is not included in

the article's Creative Commons licence and your intended use is not permitted by statutory regulation or exceeds the permitted use, you will need to obtain permission directly from the copyright holder. To view a copy of this licence, visit <http://creativecommons.org/licenses/by/4.0/>.

## References

- Bach GG, Lee JHS (1970) An Analytical Solution for Blast Waves. *AIAA J* 8(2):271–275. <https://doi.org/10.2514/3.5655>
- Bathel BF, Weisberger JM, Herring GC, King RA, Jones SB, Kennedy RE, Laurence SJ (2020) Two-point, parallel-beam focused laser differential interferometry with a Nomarski prism. *Appl Opt* 59(2):244. <https://doi.org/10.1364/ao.59.000244>
- Birch B, Buttsworth D, Zander F (2020) Measurements of freestream density fluctuations in a hypersonic wind tunnel. *Exp Fluids* 61:158. <https://doi.org/10.1007/s00348-020-02992-w>
- Biss MM, Settles GS, Staymates ME, Sanderson SR (2008) Differential schlieren-interferometry with a simple adjustable Wollaston-like prism. *Appl Opt* 47(3):328. <https://doi.org/10.1364/ao.47.000328>
- Ceruzzi A, Cadou CP (2019) Simultaneous Velocity and Density Gradient Measurements using Two-Point Focused Laser Differential Interferometry. In: *AIAA Scitech 2019 Forum*, American Institute of Aeronautics and Astronautics, <https://doi.org/10.2514/6.2019-2295>
- DLR (2018) The High Enthalpy Shock Tunnel Göttingen of the German Aerospace Center (DLR). *J Large-scale Res Facil* 4:A133. <https://doi.org/10.17815/jlsrf-4-168>
- Fulghum MR (2014) Turbulence measurements in high-speed wind tunnels using focusing laser differential interferometry. PhD thesis, The Pennsylvania State University
- Gragston M, Price T, Davenport K, Zhang Z, Schmisser JD (2021a) Linear array focused-laser differential interferometry for single-shot multi-point flow disturbance measurements. *Opt Lett* 46(1):154. <https://doi.org/10.1364/ol.412495>
- Gragston M, Siddiqui F, Schmisser JD (2021b) Detection of second-mode instabilities on a flared cone in Mach 6 quiet flow with linear array focused laser differential interferometry. *Exp Fluids* 62:81. <https://doi.org/10.1007/s00348-021-03188-6>
- Jewell JS, Parziale NJ, Lam KL, Hagen BJ, Kimmel RL (2016) Disturbance and Phase Speed Measurements for Shock Tubes and Hypersonic Boundary-Layer Instability. In: *32nd AIAA Aerodynamic Measurement Technology and Ground Testing Conference*, American Institute of Aeronautics and Astronautics, <https://doi.org/10.2514/6.2016-3112>
- Jewell JS, Hameed A, Parziale NJ, Gogineni SP (2019) Disturbance Speed Measurements in a Circular Jet via Double Focused Laser Differential Interferometry. In: *AIAA Scitech 2019 Forum*, American Institute of Aeronautics and Astronautics, <https://doi.org/10.2514/6.2019-2293>
- Jones DL, Goyer GG, Plooster MN (1968) Shock Wave from a Lightning Discharge. *J Geophys Res* 73(10):3121–3127. <https://doi.org/10.1029/jb073i010p03121>
- Kinney GF, Graham KJ (1985) *Explosive Shocks in Air*. Springer, Berlin Heidelberg. <https://doi.org/10.1007/978-3-642-86682-1>
- Lawson JM, Neet MC, Grossman JJ, Austin JM (2019) Characterization of a Focused Laser Differential Interferometer. In: *AIAA Scitech 2019 Forum*, American Institute of Aeronautics and Astronautics, <https://doi.org/10.2514/6.2019-2296>
- Parziale N (2013) Slender-Body Hypervelocity Boundary-Layer Instability. PhD thesis, California Institute of Technology
- Parziale NJ, Shepherd JE, Hornung HG (2013) Differential Interferometric Measurement of Instability in a Hypervelocity Boundary Layer. *AIAA J* 51(3):750–754. <https://doi.org/10.2514/1.J052013>

Sanderson SR (2005) Simple, adjustable beam splitting element for differential interferometers based on photoelastic birefringence of a prismatic bar. *Rev Sci Instrum* 76(11):113703. <https://doi.org/10.1063/1.2132271>

Siddiqui F, Gragston M, Saric WS, Bowersox RDW (2021) Mack-mode instabilities on a cooled flared cone with discrete roughness elements at Mach 6. *Exp Fluids* 62:213. <https://doi.org/10.1007/s00348-021-03304-6>

Weisberger JM, Bathel BF, Herring GC, Buck GM, Jones SB, Cavone AA (2020) Multi-point line focused laser differential interferometer for high-speed flow fluctuation measurements. *Appl Opt* 59(35):11180. <https://doi.org/10.1364/ao.411006>

**Publisher's Note** Springer Nature remains neutral with regard to jurisdictional claims in published maps and institutional affiliations.

## 3.2. Validation of computational FLDI as an analysis tool (Publication 2)

The computational FLDI (cFLDI) intended to be used in the shock tunnel investigation in the present Ph.D. project was coded in-house, based mainly on the works by Schmidt and Shepherd [75] and Lawson and Austin [78]. It needed, therefore, to be validated before it could be used as an analysis tool. With no public or commercial software available with equivalent capabilities, a reference test case needed to be studied with this validation purpose.

The blast wave propagating in a medium at rest, which had been measured in the previous publication, offered excellent qualities for that end. The measurements were clear and repeatable, meaning that setbacks usual in experiments, such as background noise level or experimental uncertainty, could be minimized. Furthermore, the flowfield generated by a weak blast wave is simple and amenable to analytic modeling, meaning a computational flowfield could potentially be obtained for the cFLDI simulation with relative ease.

However, a complete analytic model of the blast wave required an accurate measurement of the energy deposited in the medium to generate it. With the modest, low-cost setup based on a modified automotive spark plug that had been developed earlier, this was not achievable.

The solution was to use the cFLDI directly on the experimental data, instead of relying on an analytic model to produce the numerical results. In order to do that, a method to convert the line-based phase difference FLDI data into a radially distributed density flowfield was developed, based on the works by Yuldashev et al. [82] and Karzova et al. [83]. The methodology required a number of simplifying hypotheses, such as ignoring the divergence angle of the FLDI beams, approximating the differential measurement as a spatial derivative, among others. On the one hand, the set of assumptions represented a constraint to the general application of the developed methodology. On the other hand, however, it presented the opportunity to advance yet another step in the proposed usage of cFLDI, namely as a verification tool for post-processing methodologies.

The principle explored to that end was that the proposed FLDI data conversion method was independent from the cFLDI algorithm and equations. Once the numeric density flowfield was obtained, the cFLDI algorithm was able to calculate a response akin to the original experimental one. If large discrepancies had been detected, the cause could have lied either with the post-processing methodology, or with the cFLDI algorithm, or even both. However, if good agreement was observed, then a reasonable conclusion is that both the conversion method and the cFLDI had worked well, since they are mutually independent.

Nevertheless, such simultaneous validation without any additional verification is not ideal. To address this issue, two additional checks were performed on the numeric flowfield obtained with the proposed post-processing methodology. First, a wall-mounted, fast response pressure transducer was employed to measure the acoustic pressure behind the blast wave in a subset of distances from the source. Second, the relation between the compression phase period and the peak overpressure of the waveforms across the entire data set was verified against an analytic model

from the linear theory of sound in gases. Combined, the results indicated that the obtained waveforms are indeed typical of weak blast waves, and that their magnitude was in close agreement with the experiments, lending credibility to the proposed post-processing methodology.

As for the cFLDI results, the analysis has shown that the simplification hypotheses require that certain constraining conditions are met. The main one is a maximum FLDI differentiation distance of 20% the length of the compression front of the blast wave. Once these constraints were respected, the cFLDI data correlated with the experiments to within 0.5% when the full signal was considered. The maximum point-wise discrepancy was observed at the location with peak signal magnitude, with difference below 3%. These results further demonstrate that the proposed post-processing methodology is sound, and show that the cFLDI is capable of converting the numeric flowfield back to the experimental FLDI data, within a reasonable deviation.

The work that has led to this article was supervised by A. Wagner. The post-processing methodology was conceptualized and developed by me. The experimental setup was designed by I. Schwendtke and me. The experimental investigation was conducted by me. The cFLDI computational code was implemented by me. Analyses of the data were conducted by me and A. Wagner. The manuscript was written by me and edited by A. Wagner. The article is Open Access under a Creative Commons Attribution (CC BY) license (<http://creativecommons.org/licenses/by/4.0/>). It was published in *Review of Scientific Instruments*, **2023**, *94* (4), 045102. (DOI: <https://doi.org/10.1063/5.0132874>)

**Copyright © 2023 Authors**

# Focused laser differential interferometry post-processing methodology for flowfields with circular symmetry

Cite as: Rev. Sci. Instrum. 94, 045102 (2023); doi: 10.1063/5.0132874  
Submitted: 31 October 2022 • Accepted: 13 March 2023 •  
Published Online: 3 April 2023



View Online



Export Citation



CrossMark

Giannino Ponchio Camillo<sup>a)</sup>  and Alexander Wagner<sup>b)</sup> 

## AFFILIATIONS

German Aerospace Center (DLR), Institute of Aerodynamics and Flow Technology, Göttingen, Germany

<sup>a)</sup> Author to whom correspondence should be addressed: [Giannino.PonchioCamillo@dlr.de](mailto:Giannino.PonchioCamillo@dlr.de)

<sup>b)</sup> Electronic mail: [Alexander.Wagner@dlr.de](mailto:Alexander.Wagner@dlr.de)

## ABSTRACT

An analytic methodology is presented to reconstruct the pressure waveform of flowfields with circular symmetry from the phase shift detected with Focused Laser Differential Interferometry (FLDI). A weak blast wave generated by an electric spark in ambient air is investigated with the proposed approach. Values of separation distance between the differentiating foci of the FLDI  $\Delta x$  of 76, 120, 175, and 252  $\mu\text{m}$  are employed to probe the flowfield at locations between 3 and 50 mm from the spark source. In a subset of these distances, reference measurements of peak pressure obtained with a surface pressure sensor indicate good agreement with the reconstructed data when small separation distances are used. Further analysis of FLDI reconstructed data is conducted using theoretical correlations for N-waves in terms of the distribution of pressure peak amplitude and compression phase as the wave front propagates. Agreement with theory is verified for all differentiation separation distances except the largest, for which peak pressure comparison shows a 10% loss of measured vs predicted value. A computational FLDI is employed to scrutinize the simplifying hypotheses supporting the waveform reconstruction approach. The direct comparison between experimental and computational FLDI output reveals additional discrepancies for intermediate  $\Delta x$  values but very good agreement for the smallest  $\Delta x$ . The proposed methodology is thus verified to be reasonable, upon appropriate minimization of the FLDI differentiation distance. A parametric analysis using computational FLDI indicates the adequate value of FLDI  $\Delta x$  to be 20% or less of the flowfield characteristic length in terms of density gradient.

© 2023 Author(s). All article content, except where otherwise noted, is licensed under a Creative Commons Attribution (CC BY) license (<http://creativecommons.org/licenses/by/4.0/>). <https://doi.org/10.1063/5.0132874>

## I. INTRODUCTION

Focused Laser Differential Interferometry (FLDI) is a non-invasive measurement technique that measures flowfield density fluctuations. Its distinct spatial and temporal resolutions render it especially suited for ground-based experimental investigation of hypersonic flowfields. Attention to this technique has been growing steadily within the community since Refs. 1 and 2. This is evidenced by the increasing number of laboratories implementing the FLDI technique in recent years.<sup>3–8</sup>

Owing to the broad bandwidth of the FLDI and its robustness to external noise, the evaluation of the frequency spectrum of FLDI data using only simplified post-processing approaches has been proven to already offer valuable information about the probed

flowfields.<sup>9–13</sup> Nonetheless, a rigorous conversion of FLDI data into flowfield quantities such as density fluctuation is required in order to fully explore the capabilities of the technique and allow quantitative evaluations. However, this task is made difficult by some of the key features of the FLDI. The ability of the FLDI to dampen frequencies away from its focus and the finite differentiation it performs must be considered when attempting to convert the FLDI output back into flowfield variables.

The extraction of quantitative density data while respecting the complexity of the FLDI response has been explored by means of transfer function analysis.<sup>2,14</sup> This methodology has been initially shown for special types of flowfields such as uniformly distributed turbulence or Gaussian jets.<sup>2</sup> Agreement between pitot-based pressure fluctuations and FLDI data processed with transfer

functions has also been experimentally demonstrated in a Mach 6 free stream.<sup>15</sup> Recent efforts have included the deduction of transfer functions for more complex flowfields, encompassing two and three-dimensional sinusoidal disturbances, either infinitesimally thin, uniform within a finite volume, or modulated by a Gaussian intensity profile.<sup>16,17</sup> A sensitivity function for the FLDI has been developed using transfer functions and verified using a turbulent air jet<sup>18,19</sup> and wind-tunnel disturbances.<sup>20</sup> A solution for the inverse FLDI problem for single-direction, continuous-frequency waves has been proposed and experimentally verified against supersonic free stream pitot data.<sup>21</sup>

These efforts represent significant advancements toward a better understanding of the FLDI technique and the proper treatment of the data it offers. Nonetheless, at each instant in time, the FLDI output from a three-dimensional density field consists of a single scalar value as a result of successive integrals and differences of flowfield quantities. Therefore, assumptions about the topology of the flowfield are inevitable when trying to reverse this problem.<sup>22</sup> The flowfield models recently explored in Refs. 16–22 are able to represent many practical applications, such as turbulent jets, free stream turbulence, and acoustic radiation, among others. Still, they must be adjusted according to the flowfield at hand and might not offer the easiest solution for all kinds of flowfields. Furthermore, if the flowfield model must be adjusted manually in a case-by-case fashion, it is important to have a way to independently verify the obtained results.

One such way is to numerically simulate the FLDI response using a ray-tracing scheme,<sup>23</sup> which is able to reproduce how the flowfield variations are perceived by the FLDI beams. This computational FLDI (cFLDI) has been shown to produce accurate quantitative results against experiments for a static laminar jet<sup>24</sup> and a complex shock-dominated dynamic flowfield.<sup>25</sup> The cFLDI has since been employed to further study the technique. For example, the dependence between the FLDI sensitivity length and the beam divergence angle has been verified using parametric analysis.<sup>26</sup> The ability of the FLDI instrument to see through unwanted signals at the edges of the probing volume, such as the wall boundary layers or the nozzle shear layer in hypersonic wind-tunnels, has also been explored.<sup>27</sup> Furthermore, cFLDI simulated on the DNS solution of a wind-tunnel boundary layer has been investigated as a means to inform constraints for the FLDI application.<sup>28</sup>

This type of insight is allowed by the proven physical fidelity of the cFLDI, which, therefore, places it as a tool to explore methodologies that aim at obtaining quantitative information from FLDI data but are only feasible by assuming model parameters or adopting certain simplifying hypotheses. Once the flowfield is reconstructed from real FLDI measurements, a simulated FLDI response may be obtained with the high-fidelity ray-tracing algorithm; then, a comparison between the real and simulated FLDI data allows for assessing the validity of any assumptions or simplifications involved in the post-processing method.

The goal of the present work is to contribute toward the inclusion of circularly symmetric flowfields in the subset of special cases for which FLDI data can be fully regressed into flowfield quantities through analytic approaches. A number of assumptions will be necessary to reach this objective. In light of the physical accuracy of cFLDI demonstrated in Refs. 24 and 25, simulations using an implementation of the FLDI ray-tracing algorithm are employed

to support the analysis of the results obtained with the analytic approach.

The object of study to apply and analyze the proposed methodology is a weak blast wave generated by an electric spark in ambient air at rest, using a setup detailed in a previous study by the present authors.<sup>8</sup> The study of blast waves pertains to various applications ranging from explosive detonations to sonic booms.<sup>29,30</sup> A review of the diagnostic tools currently available for the experimental study of such flows is summarized in Ref. 31. In that work, laser interferometry was suggested as a solution to overcome the bandwidth and sensitivity limitations of consolidated techniques such as dynamic pressure transducers and condenser microphones. The FLDI presents similar capabilities with further advantages such as adjustable sensitivity and simplicity, and may, therefore, be of interest to related investigations.

The contents of this paper are summarized as follows: Experimental measurements of a weak spark-generated blast wave are collected using FLDI at multiple distances from the spark source. A methodology is presented to obtain the spherical distribution of quantitative acoustic pressure from such measurements, following a series of simplifying assumptions. No other instruments of similar capability were available to produce detailed reference measurements for comparison with the FLDI data. Therefore, the obtained results are verified using multiple complementary approaches. In a first step, peak pressures are compared to direct measurements using a fast piezoelectric pressure transducer, performed at locations allowed by the geometric constraints of the experimental setup. Next, the obtained waveforms are compared with analytic correlations involving compression phase duration and peak pressure for propagating acoustic pulses. Finally, the FLDI response to the reconstructed flowfield is simulated with the ray-tracing scheme and compared to the original experimental data. The simplifying assumptions necessary for the flowfield reconstruction methodology are analyzed in light of observed discrepancies to help identify eventual constraining parameters that control the fidelity of the reconstruction. The emphasis is given to a single location along the blast wave trajectory, namely, 30 mm from the spark, although the procedure is applicable to any given location.

## II. THEORETICAL BACKGROUND

### A. Blast waves

A blast wave in a fluid at rest can be originated by a localized instantaneous release of energy. The change in local pressure and temperature propagates away from the origin of the event at the speed of sound in the immediate medium. Because the speed of sound is larger in regions with higher temperatures, those portions of the disturbance propagate faster than those in their vicinity. A discontinuity is hence formed as a shock wave front,<sup>29</sup> which propagates supersonically with respect to the undisturbed fluid.

In the case of radially propagating blast waves, the strength of the shock wave front will progressively become weaker due to volume divergence, dissipation, and molecular relaxation. Eventually, the blast wave becomes so weak that it propagates approximately at the sound speed of the non-disturbed gas, becoming an acoustic wave. This process is accompanied by changes in the pressure signature, best described in terms of acoustic pressure, i.e., the overpressure with respect to the undisturbed field. The blast wave is

marked by a sharp and narrow compression phase (positive acoustic pressure), followed by a longer and smoother expansion phase (negative acoustic pressure). As the blast wave propagates, the amplitude of the positive phase decreases and the trailing edge of the negative phase becomes sharper due to the slightly higher local sound speed. The pressure waveform then describes a so-called N-wave.

Close to the blast wave source, the spark-generated blast wave is best approximated as a cylindrical shock due to the finite length of the spark. In the acoustic limit region, which is evaluated in more detail here, the distance to the cylindrical source is an order of magnitude higher than the length of the spark. In such a case, the flowfield generated by a point-source is a better representation of the local blast wave disturbance than the one generated by an infinite line. Therefore, a point-source hypothesis is considered in this work.

For the spherical propagation of N-waves, Ref. 32 presented analytic expressions from the linear theory of sound in gases (weak-shock theory) amenable to experimental comparisons, having also approximated an electric spark as a point-source downstream of a few spark lengths from the discharge. The methodology presented therein consisted of calculating the acoustic pressure peaks behind the shock,  $P$ , expected from theory, given measurements of compression phase duration,  $T$ , over several distances from the N-wave source. In the present work, both peak pressure and compression phase duration will be obtained directly from FLDI measurements. The cited methodology will, therefore, be employed to verify whether the obtained  $(T, P)$  pairs are physically consistent with the expected behavior of an N-wave.

The equations and procedures from Ref. 32 pertinent to the present work are briefly reproduced next. A different variable notation than presented in that work is used here for clarity. The compression phase duration  $T$  of the N-wave when the spherical wave front has propagated through a distance  $R$  from its origin can be written in terms of its value at an arbitrary reference propagation distance (subscript 0) as

$$T = T_0 \sqrt{1 + \sigma_0 \ln(R/R_0)}. \quad (1)$$

The non-dimensional parameter  $\sigma_0$  in this equation is a function of the N-wave compression phase duration and peak acoustic pressure at the reference distance, as well as the undisturbed medium pressure  $P_{\text{amb}}$ , sound speed  $c_{\text{amb}}$ , and specific heat ratio  $\gamma$  as

$$\sigma_0 = (\gamma + 1)R_0 P_0 / (2\gamma P_{\text{amb}} c_{\text{amb}} T_0). \quad (2)$$

It is noted in Ref. 32 that through Eq. (1),  $T^2$  as a function of  $\log R$  describes a straight line with slope equal to  $\sigma_0 T_0^2 \ln 10$ . This slope may be obtained from a dataset of measured compression phases  $T$  at multiple locations  $R$ . Since the reference location (subscript 0) is arbitrary, the slope evaluates  $\sigma$  for any  $T$ . Finally, Eq. (2) defines the peak pressure  $P$  from weak-shock theory, which corresponds to the experimentally measured  $T$ .

### B. Focused laser differential interferometry

Laser interferometry is achieved by combining two coherent monochromatic beams presenting equal intensity and linear polarization in the same direction, after having traveled through different optical paths. The interference resulting from their superposition

causes the combined light intensity to be modulated by any difference in phase between the beams. This difference in phase is accumulated along the entirety of the paths described by the beams. The intensity of the recombined beam is detected as a scalar value, resulting from integrating the light intensity changes across the face of the beam at the detector. A differential interferometer is obtained when the beams go through the same medium, separated by a small distance.

In the special case of a focused laser differential interferometer (FLDI), the two beams are focused to a point within the probed volume. These two defining characteristics are responsible for making the sensitive volume of the FLDI dependent on the wavelength of the disturbances in the probed flowfield, with high-frequency content being rejected away from the focal plane. If the wavelength of the flowfield fluctuation in a certain portion of the beams is too small relative to their cross-section size, the contribution of those disturbances to the final signal is averaged out through integration at the face of the detector. For a thorough discussion about this, see Ref. 2.

For the reconstruction of spherical blast waves from FLDI detection presented in this work, a simplified approach that disregards the FLDI wavelength-dependent sensitivity is adopted. The validity of this assumption is verified with the assistance of a computational model that fully represents the real apparatus. This is made possible by observing that the series of processes involved in the interaction between the probed flowfield and the FLDI beams is challenging to reverse but straightforward to reproduce. Simplifying hypotheses can, therefore, be evaluated by comparing the high-fidelity simulated FLDI output of the reconstructed field with the experimental FLDI data that originated it.

The computational FLDI used in this work is based on the ray-tracing model of Ref. 23 and is similar in terms of implementation and application to the recent validation work of Ref. 25. A summary of the pertinent concepts and equations used in this work is given next.

A Cartesian coordinate system is defined with the  $z$  axis parallel to the optical axis (direction of propagation of the beams), the  $x$  axis parallel to the direction of separation between the beams, and the origin at the midpoint between the FLDI foci. Each beam is discretized into a finite number of rays, parameterized in a convenient auxiliary coordinate system to account for the focusing of the beams in a computationally effective manner. The FLDI used in this work presents a Gaussian, circular beam cross-section. Therefore, a polar coordinate system  $(\tilde{r}, \theta)$  is used to distribute the rays around a center point in the cross-section with  $0 \leq \theta < 2\pi$  and  $0 < \tilde{r} \leq \tilde{r}_{\text{max}}$ . The radial coordinate  $\tilde{r}$  is non-dimensionalized with respect to the local Gaussian beam radius  $w(z)$ ,

$$w(z) = \sqrt{w_0^2 \left( 1 + \left[ \frac{\lambda_0 z}{\pi w_0^2} \right]^2 \right)}, \quad (3)$$

where  $\lambda_0$  is the light wavelength and  $w_0 = \lambda_0 / \pi \theta_d$  is the waist of the beam at the focal plane ( $z = 0$ ), with  $\theta_d$  the beam divergence angle. An upper limit for the non-dimensional radial coordinate of  $\tilde{r}_{\text{max}} = 2$  (two times the local Gaussian beam radius, in dimensional coordinates) is adopted.<sup>23</sup>

A greatly simplified exemplary computational mesh is illustrated in the Cartesian space in Fig. 1. For clarity, only a region very

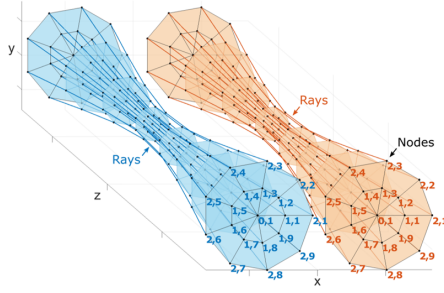


**FIG. 1.** Illustrative cFLDI mesh, very coarse for clarity. A pair of beams of an FLDI very near its center plane are shown in different colors, each denoting one plane of orthogonal polarization. Lines connecting the nodes of individual rays are marked. The labels of nodes on the front plane are numbered as coordinate pairs: radial coordinate and angle coordinate.

close to the focus of the system is shown. The pair of orthogonally polarized beams is displayed in different colors. The spatial discretization is performed through the definition of nodes as the  $(\tilde{r}, \theta)$  pairs at each  $z$ -plane and rays connecting all nodes with the same non-dimensional coordinates across all  $z$ -planes. The discretization of each beam is identical except for an offset in the  $x$  direction.

The rays shown in Fig. 1 are treated as pairs to perform the differential operations. Each ray in one of the beams has a correspondent counterpart in the other, as labeled on the front plane of the figure. Flowfield density values are interpolated to the FLDI nodes at each instant in time. The total number of  $z$  planes is even, so that all rays undergo a quadrant inversion in  $\theta$  as they cross  $z = 0$  to account for image inversion through the focus.<sup>25</sup> This is performed internally in the algorithm and is not shown in Fig. 1.

Fluctuations in density  $\rho$  in the flowfield crossing the rays shown in Fig. 1 cause their optical paths to vary due to changes in the local refraction index  $n$ . A difference in the optical paths traveled by two monochromatic and coherent light rays causes a difference in phase  $\Delta\phi$  between them.<sup>33</sup> These effects are combined as

$$\Delta\phi = \frac{2\pi K}{\lambda_0} \left( \int_{C_1} \rho(s_1) ds_1 - \int_{C_2} \rho(s_2) ds_2 \right), \quad (4)$$

with  $K$  the Gladstone–Dale constant for the light wavelength  $\lambda_0$ ,  $C_1$  and  $C_2$  defining the spatial path traveled by each beam, and the field density parameterized as  $\rho(s_i)$ , with  $s_i$  the spatial variable that describes  $C_i$ .

Equation (4) is valid for each corresponding pair of light rays that compose the two beams of one FLDI. Upon recombination and projection of the two beams back to a common polarization plane, the resulting light intensity of each ray is modulated by the phase difference  $\Delta\phi$  as<sup>33</sup>

$$I = I_1 + I_2 + 2\sqrt{I_1 I_2} \cos \Delta\phi, \quad (5)$$

where  $I_1$  and  $I_2$  are the intensities of the separate rays, and  $I$  is the intensity of the recombined ray.

The output of the FLDI is given by the average of the intensities of all rays, weighted according to the intensity profile of the beam. For a Gaussian beam, the normalized intensity profile is described by  $\tilde{I}_0(\tilde{r}) = 2\pi^{-1} \exp(-2\tilde{r}^2)$ . If the undisturbed orthogonally polarized pair is adjusted to present an initial phase difference of  $\pi/2$  and an equal intensity distribution  $\tilde{I}_0/2$ , the normalized intensity at the face of the detector  $D$  becomes,

$$\tilde{I}_D = \iint_D (\tilde{I}_0(\tilde{r}, \theta) + \tilde{I}_0(\tilde{r}, \theta) \sin \Delta\phi(\tilde{r}, \theta)) d\tilde{r} d\theta, \quad (6)$$

with  $\Delta\phi(\tilde{r}, \theta)$  evaluated using Eq. (4) for each ray. Experimental FLDI data are usually given in terms of an equivalent phase shift  $\Delta\Phi$  that represents the normalized intensity  $\tilde{I}_D$  of Eq. (6). With the light intensity normalization chosen such that the integral of  $\tilde{I}_0$  over  $D$  is unity, the equivalent phase shift  $\Delta\Phi$  becomes

$$\Delta\Phi = \sin^{-1} \left( \iint_D \tilde{I}_0(\tilde{r}, \theta) \sin \Delta\phi(\tilde{r}, \theta) d\tilde{r} d\theta \right). \quad (7)$$

In the present work, all integrals are numerically calculated using trapezoidal integration. Equations (4) and (7), when used with an appropriate computational mesh, fully represent the FLDI probing a given flowfield. The cFLDI mesh is kept fixed in space, which implies ignoring any steering of the rays caused by local gradients of refraction index. Nonetheless, the effect of this simplification on the accuracy of cFLDI simulations is negligible. This has been confirmed in Ref. 25, in which a complex experimental shock-dominated flowfield was accurately represented by cFLDI simulation using that same constraint.

It is noteworthy that, when performing cFLDI simulations, the operation of interpolating flowfield data to FLDI nodes presents a marked influence on computational cost. For the analysis of a spherically symmetrical disturbance such as the spark-generated blast wave of the present work, the magnitude of the field disturbance at any location is simply described in terms of the radial variable  $r$  of a spherical coordinate system. By shifting the origin of the FLDI Cartesian system to coincide with the source of the disturbance, the coordinates of each FLDI node  $(x_i, y_i, z_i)$  are simply represented in that system as  $r_i = \sqrt{x_i^2 + y_i^2 + z_i^2}$ . This way, the density value at each node is efficiently interpolated from the field disturbance data.

### C. Reconstruction of spherical waveforms from FLDI data

Figure 2 illustrates the principle of the flowfield investigation in this work. The generated disturbance flowfield is approximated as spherical, such that at any given instant it is fully described by the spherical coordinate  $r$ , with origin coincident with the location of the disturbance source. The interferometric pair of the FLDI is parallel to the Cartesian  $z$  and crosses  $x$  at a distance  $x_0$  to the disturbance source. The separation distance between the orthogonally polarized beams is  $\Delta x$ . In this section, a methodology to obtain the radial distribution of acoustic pressure based on measured FLDI data is presented.

The problem of interpreting data from spherically diverging acoustic N-waves using experimental techniques that probe along straight lines was addressed in detail in Refs. 31 and 34. A similar procedure will be adopted here, with a few additional assumptions

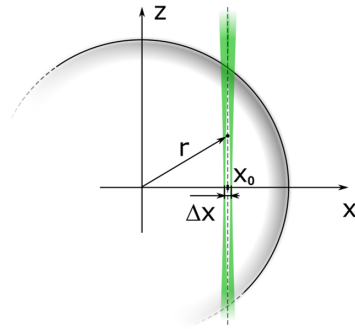


FIG. 2. Schematic of one FLDI bundle (green) probing a circular disturbance (gray). Relevant Cartesian and spherical coordinates are shown. Dimensions not to scale.

and considerations specific to the FLDI. Simplifying hypotheses are adopted and critically evaluated later in this work with the support of experiments and computational FLDI.

First, the line integrals in Eq. (4) are expressed in spherical coordinates. The FLDI coordinate system is defined such that the center lines of the paths  $C_1$  and  $C_2$  are parallel to the Cartesian  $z$  axis. The volume described by the FLDI beams is assumed to be slender enough that the problem can be simplified to the two dimensions shown in Fig. 2 and that the small divergence angle of the beams can be neglected within the reconstruction method.

It is noteworthy that with these assumptions, the method described here is applicable in cases of circular symmetry around a point, such as a sphere, and also around an axis, such as a cone or a cylinder with the probing direction perpendicular to their center axis. The integration paths  $s_i$  in Eq. (4) are hence defined by a constant  $x$ , i.e.,  $s_i = s_i(x_i, z)$  and  $ds_i = dz$ . A line of constant  $x = x_i$  is written in spherical coordinates as  $r = \sqrt{x_i^2 + z^2}$ , yielding  $dz = r dr / \sqrt{r^2 - x_i^2}$ . Finally, considering that the disturbance field is symmetric around  $z = 0$  and that  $r|_{z=0} = x_i$  and  $r|_{z=\infty} = \infty$ , each integral in Eq. (4) becomes

$$\int_{-\infty}^{\infty} \rho(x_i, z) dz = 2 \int_{x_i}^{\infty} \frac{\rho(r) r}{\sqrt{r^2 - x_i^2}} dr. \quad (8)$$

This integral is now analyzed in light of the problem at hand. The flowfield surrounding the blast wave is assumed to be initially at rest. Hence, although the upper limit of the integral in Eq. (8) is infinite, the integration length of practical significance will be defined by the blast wave radius. Furthermore, except for very close to the origin of the blast wave, the acoustic disturbance defined by it will be largely concentrated in the inner vicinity of its radius at any instant in time, and zero everywhere else. With these two observations, it is reasonable to consider  $z \ll x_i$  within the relevant integration length in Eq. (8). Finally, for a small displacement  $\Delta x$ , consequently,  $x + \Delta x \approx x$ ,  $\Delta r \approx \Delta x$ , and  $r + \Delta r \approx r$ . By defining the location of each FLDI beam as  $x_i = x_0 \pm \Delta x/2$  (see Fig. 2), Eq. (8) can be approximated for each beam as

$$\int_{x_0 - \frac{\Delta x}{2}}^{\infty} \frac{\rho(r) r}{\sqrt{r^2 - (x_0 - \frac{\Delta x}{2})^2}} dr \approx \int_{x_0}^{\infty} \frac{\rho(r - \frac{\Delta r}{2}) r}{\sqrt{r^2 - x_0^2}} dr, \quad (9)$$

$$\int_{x_0 + \frac{\Delta x}{2}}^{\infty} \frac{\rho(r) r}{\sqrt{r^2 - (x_0 + \frac{\Delta x}{2})^2}} dr \approx \int_{x_0}^{\infty} \frac{\rho(r + \frac{\Delta r}{2}) r}{\sqrt{r^2 - x_0^2}} dr.$$

With the integrals now having the same integration limits, Eq. (4) is rewritten as

$$\Delta\phi = \frac{2\pi K}{\lambda_0} \left[ 2 \int_{x_0}^{\infty} \left( \rho\left(r - \frac{\Delta r}{2}\right) - \rho\left(r + \frac{\Delta r}{2}\right) \right) \frac{r}{\sqrt{r^2 - x_0^2}} dr \right]. \quad (10)$$

It is possible to isolate the density difference in the integrand of Eq. (10) by means of an Abel transform, following Refs. 31 and 34,

$$F(x) = 2 \int_x^{\infty} \frac{f(r) r}{\sqrt{r^2 - x^2}} dr, \quad (11a)$$

$$f(r) = -\frac{1}{\pi} \int_r^{\infty} \frac{dF(x)}{dx} \frac{dx}{\sqrt{x^2 - r^2}}. \quad (11b)$$

An expression describing the radial distribution of density differences as a function of phase differences measured along a secant line is thus obtained,

$$\rho\left(r - \frac{\Delta r}{2}\right) - \rho\left(r + \frac{\Delta r}{2}\right) = -\frac{\lambda_0}{2\pi^2 K} \int_r^{\infty} \frac{d\Delta\phi(x)}{dx} \frac{dx}{\sqrt{x^2 - r^2}}. \quad (12)$$

Note that Eq. (12) requires knowledge of the spatial distribution of phase differences. However, the FLDI system outputs a time-resolved phase difference at a fixed spatial location, namely the optical axis of the FLDI system. This can be addressed by assuming that the waveform probed by the FLDI travels with a uniform velocity. Indeed, the weak spark-generated blast wave analyzed here is produced with the same experimental setup as in Ref. 8, in which it was verified to present little variation from  $M = 1$  as close as 20 mm from its source. Furthermore, the hypothesis of uniform propagation velocity was tested in Ref. 31 by means of numerically simulating blast wave convection using the generalized Burger's partial differential equation. Terms accounting for non-linearity, dissipation, and relaxation processes were included, and the results revealed maximum errors close to 1% for the estimates of peak pressure and positive phase duration.

Through this assumption, a time-resolved  $\Delta\phi(t)$  is converted into a spatially-resolved  $\Delta\phi(x)$  by using

$$x = x_0 - (t - t_0)c_0, \quad (13)$$

where  $c_0$  is the convection velocity and  $t_0$  is the time corresponding to a reference coordinate  $x_0$ , which may be conveniently defined without loss of generality.

With the radial distribution of differences in density obtained from Eq. (12), an estimate of field amplitudes is obtained as follows. Assuming that the density field is composed of small disturbances, the local density can be expressed as the sum of a mean value and a fluctuating component,  $\rho(r) = \bar{\rho} + \rho'(r)$ . Since the mean component is the same for all values of  $r$ , the left-hand side of Eq. (12) is equivalent to the difference of fluctuations  $\rho'(r - \frac{\Delta r}{2}) - \rho'(r + \frac{\Delta r}{2})$ . Next, if

$\Delta r$  is small with respect to the length scale of fluctuations, the spatial derivative of  $\rho'$  at some radial coordinate  $r_i$  can be approximated as

$$\frac{d\rho'(r_i)}{dr} \approx -\left(\frac{\rho'(r_i - \frac{\Delta r}{2}) - \rho'(r_i + \frac{\Delta r}{2})}{\Delta r}\right). \quad (14)$$

Finally, expanding the radial density fluctuation  $\rho'(r)$  into a Taylor series at some radial coordinate  $r_i$  and neglecting higher-order terms,

$$\rho'(r) = \rho'(r_i) + \frac{d\rho'(r_i)}{dr}(r - r_i). \quad (15)$$

Without its higher-order terms, the accuracy of this expansion will quickly deteriorate as  $r$  becomes distant from  $r_i$ . Nonetheless, the FLDI measurements are capable of providing a very fine mesh of  $d\rho'/dr$  values due to their high temporal resolution, and the distribution of  $r_i$  can be chosen accordingly. A reasonable estimate of  $\rho'(r)$  can be obtained by using Eq. (15) sequentially, with each point  $\rho'(r_i)$  defining its neighbor  $\rho'(r_{i+1})$ . Remembering that the density fluctuations are confined to the volume described by the blast wave radius at any given time, i.e.,  $\rho'(+\infty) = 0$ , this is best done in the reverse direction, starting from the most outside point

$$\rho'(r_i) = \rho'(r_{i+1}) - \frac{d\rho'(r_i)}{dr}(r_{i+1} - r_i). \quad (16)$$

As seen in Sec. II A, blast wave data are commonly presented in the literature in terms of acoustic pressure amplitudes. As such, it will be more convenient to express the FLDI measurements as pressure fluctuations rather than density. For the small, isentropic disturbances analyzed here, density and pressure fluctuations are related through the local sound speed as

$$p' = \rho' c_0^2. \quad (17)$$

In summary, the complete set of simplifying hypotheses detailed in the preceding paragraphs is listed below:

- (a) FLDI
  - i. Divergence angle of the beams is neglected.
  - ii. Finite differentiation approximates a spatial derivative.
- (b) Flowfield
  - i. Symmetric around a center point or axis.
  - ii. Negligible density gradients outside the wave front radius at any instant.
  - iii. The wave front travels with uniform velocity within the relevant probing time.
  - iv. Isentropic within the relevant probing volume.

It is worth noting that the flowfield reconstruction methodology presented here and the numerical representation of the FLDI detailed in Sec. II B only share Eq. (4). That equation refers to a general physical principle of the behavior of light through a transparent medium of variable density. Therefore, the methods of computational FLDI simulation and flowfield reconstruction from FLDI data may be regarded as mutually independent.

### III. METHODS

#### A. Experimental setup

The experimental arrangement employed in this work is the same as that used in Ref. 8. Information relevant to flowfield reconstruction and simulation is repeated here for clarity.

The FLDI system was designed to operate in the HEG shock tunnel.<sup>35</sup> The laser source is an Oxxius LCX-532S DPSS with a nominal wavelength of 532.3 nm. The corresponding Gladstone–Dale constant for this wavelength is  $K = 0.227 \times 10^{-3} \text{ m}^3/\text{kg}$ . The orthogonally polarized pair of beams is produced and later recombined using a pair of Sanderson prisms,<sup>36</sup> allowing different beam separation distances  $\Delta x$  to be produced. Four values of  $\Delta x$  are analyzed, namely 76, 120, 175, and 252  $\mu\text{m}$ . The beams are approximately Gaussian with a maximum diameter of 45 mm at the field lenses, which are 3.8 m apart.

The photodetector is a Thorlabs DET36A2 of nominal bandwidth 25 MHz connected to an amplifier and recorder with a 50  $\Omega$  termination. The signal is recorded with DC-coupling and a sampling rate of 100 MHz. The conversion of the voltage produced by the photodetector into the FLDI phase difference is performed following Ref. 37. Prior to measurements, the undisturbed response of the FLDI is adjusted to the region of maximum sensitivity.

The probed flowfield is generated by the electric spark of an automotive spark plug with a 4 mm separation between its electrodes. The resulting weak blast wave propagates with approximately the ambient sound speed at distances larger than 20 mm from its origin, as analyzed in Ref. 8. The flowfield topology is shown in Fig. 3, with a series of superimposed schlieren images. In addition to the blast wave propagating radially, Fig. 3 also shows a secondary wave that propagates diagonally upward. This is a reflection of the main wave front off the structure of the spark generator and will be considered in Sec. IV.

A diagram of the experimental setup is shown in Fig. 4. The spark generator can be moved with respect to the fixed FLDI depicted in Figs. 4(a) and 4(b) along the axis of beam separation, such that measurements can be taken and analyzed at multiple distances from the source, represented as  $R$  in the frames of the figure. Measurements are taken at 23 positions with nominal distances between the source and probing volume of 3–50 mm. The spacing between the probing positions is smaller near the source, and position uncertainty is estimated at  $\pm 0.25$  mm. A single spark is generated for each measurement, with the disturbances allowed to fully dissipate before the next one. Despite the careful adjustment

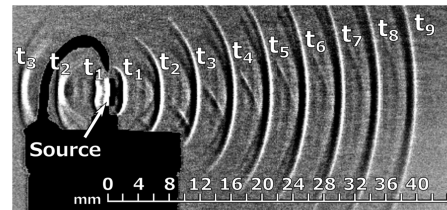
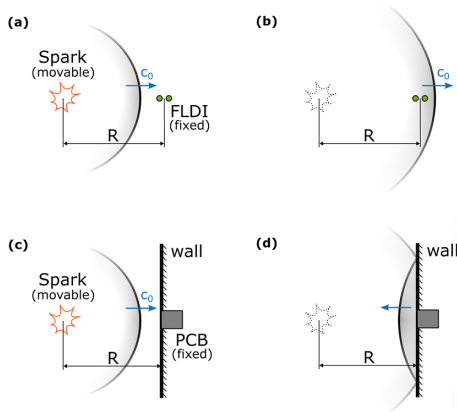


FIG. 3. Superposition of enhanced schlieren images of the blast wave generated using an automotive spark plug. The wave fronts at each instant in time are marked with the label  $t_i$ , with  $t_i - t_{i-1} = 16.7 \mu\text{s}$ . Scale at the bottom in mm.



**FIG. 4.** Diagram of the experimental setup employed to acquire blast wave measurements. (a) and (b) Depict two moments of a given measurement with FLDI, before and after the blast wave reaches the probing location, respectively. (c) and (d) Depict the corresponding moments of a measurement using the wall-mounted PCB sensor. In (d), the blast wave front has reflected off the wall on which the PCB is mounted.

and operation of the spark generator, eventual variations in flowfield generation have been observed during the tests. One possible reason is random changes in the spark breakdown path, which shift the origin and slightly alter the strength of the blast wave. Furthermore, although the experiments are conducted in a protected environment, it is not completely sealed, which may allow eventual small non-uniformities to be present in the surrounding medium. To minimize the effects of such eventual variations in flowfield generation, ten measurements are repeated at each position. The ambient sound speed is calculated using ambient temperature values obtained near the probing region before each series of measurements.

A separate series of blast wave measurements are conducted using a wall-mounted fast response piezoelectric pressure sensor PCB 132A32, as depicted in Figs. 4(c) and 4(d). The measurement approach is repeated from the FLDI measurements using the same movable spark generator setup. Starting at 16 mm from the source, the same nominal distances between the blast wave source and probing device are used. Measurements closer than this lower bound were hindered by geometric constraints. The pressure magnitudes obtained with the sensor are used as a reference for comparisons with the data post-processed from FLDI measurements. Due to the interaction between the flowfield and the wall, depicted in Fig. 4(d), a full waveform comparison is not possible. Nonetheless, the peak magnitude of overpressure detected at the wall upon reflection of the weak blast wave should be twice the overpressure of the incident wave.<sup>29</sup>

### B. Computational FLDI

A mesh convergence analysis must be conducted before using the computational FLDI to perform flowfield evaluations. The discretization of the beam cross-section variables  $\tilde{r}$  and  $\theta$  follows a

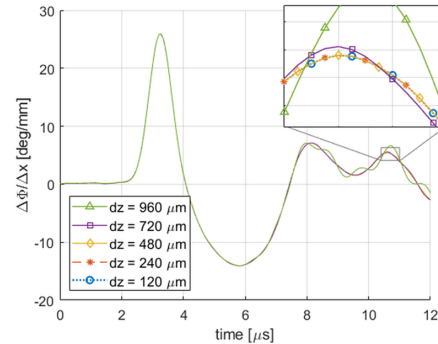


**FIG. 5.** Computational FLDI results of a blast wave using different mesh densities in the  $z$  direction. The mesh in  $z$  is defined by the uniform distance between two adjacent planes, denoted  $dz$ . Symbols are shown only in the detail inset for clarity.

mutually dependent approach such that each mesh cell has an aspect ratio close to unity,<sup>23</sup> and  $z$  is discretized in uniform steps. A single waveform, based on experiments and representative of the data that will be detailed in Sec. IV C, is used to generate computational FLDI results with different meshes.

Figure 5 shows the simulation results for different discretization steps in  $z$ . The cFLDI solution is sensitive to this parameter in later moments of the simulation when the radial propagation of the disturbances causes a more varied distribution of field properties along the FLDI optical axis. Mesh-independent results for the discretization in  $z$  are obtained with a spacing of  $480 \mu\text{m}$  and below. The value of  $480 \mu\text{m}$  has been chosen for the subsequent evaluations.

Simulations were performed varying the number of divisions in the cross-section coordinate  $\theta$ , shown in Fig. 6. Slight mesh-dependent variations are observed for the peak absolute values of the difference  $\Delta\Phi$ . These regions correspond to the largest flowfield gradient magnitudes, which require fine meshes to be sufficiently resolved. Since the radial discretization is linked to the steps in  $\theta$ , the refinement of this parameter has a strong impact on the computational requirement of the simulation. Between 144 and 576 divisions in  $\theta$ , the relative maximum difference in the simulated signal was only 0.5%. Therefore a number of 144 divisions were chosen as a balance between mesh convergence and computational cost. The corresponding number of divisions in the radial direction was 176.

The waveform used in this analysis corresponds to measurements obtained 30 mm away from the spark source, which is the location to be explored in detail in Sec. IV C. Due to the varying flow topology crossing the FLDI beams at each location, a similar mesh convergence study as presented here must be repeated accordingly if different locations are to be simulated.

## IV. RESULTS AND DISCUSSION

### A. Experimental data and processing

Figure 7 shows exemplary time-resolved experimental signals obtained at a number of probing locations and all four system configurations. The signals are minimally post-processed to yield phase

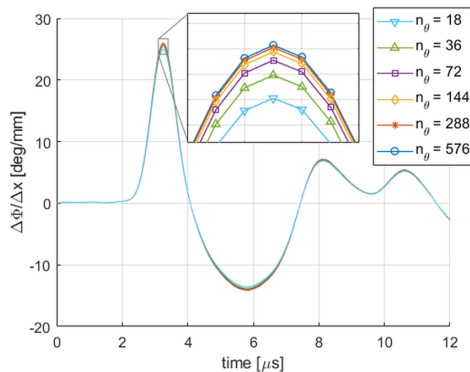


**FIG. 6.** Computational FLDI results of a blast wave using different beam cross-section meshes. The mesh in  $\theta$  is defined by the number of divisions around the circumference  $n_\theta$ , and the discretization in the radial direction is such that the aspect ratio of each cell remains close to 1. Symbols are shown only in the detail inset for clarity.

differences  $\Delta\Phi$  and divided by the corresponding differentiation distance  $\Delta x$  to allow direct magnitude comparison.

The experimental signals from all probing locations were passed through a Savitzky–Golay filter for noise reduction and processed using the procedure detailed in Sec. II C to obtain pressure waveforms. The compression phase duration was noted to be the most sensitive parameter to non-uniformities in blast wave generation. Since the blast wave correlations presented in Sec. II A depend on the global behavior of the wave as it travels away from the source, for each measurement location, the waveforms with the highest and lowest values of compression phase duration were excluded as outliers. The remaining eight waveforms were combined into an average

pressure profile, representative of the respective location, for further analysis.

Figure 8 shows the spatial evolution of pressure waveforms  $p'(r)$  detected with the FLDI for all four system configurations. Note that the spatial waveforms in Fig. 8 travel from left to right, presenting a reversed profile along the  $x$  axis compared to the temporal traces in Fig. 7 [see Eq. (13)]. Each distinct line in Fig. 8 corresponds to the blast wave detection at a given location as the spark generator was consecutively moved away from the optical axis of the FLDI. The waveforms are spatially distributed such that they cross the respective measurement location with half their peak pressure. Where available, the reference peak pressures measured with the wall-mounted PCB pressure sensor are also shown, divided by a factor of two as mentioned in Sec. III A.

The typical blast wave profile with a sharp and strong compression front followed by a longer and less intense expansion region is observed in the vicinity of the spark generation. As the wave front propagates radially, the N-wave shape becomes evident, with approximately symmetric compression and expansion phases. The inset in Fig. 8 shows in detail the waveform obtained for  $R = 30$  mm as an example. Small differences between the lines for each  $\Delta x$  can be seen, which will be further explored in Sec. IV C with aid from computational FLDI. The positive pressure seen at the trailing edge of the waveforms (e.g., near the left-hand edge of the inset) is a secondary wave that stems from the reflection of the main wave front on the structure of the spark generator. This is seen as an oblique trace propagating diagonally upward in the flow topology shown in Fig. 3. The remainder of the secondary wave is cut off from the waveforms in Fig. 8 for clarity.

Concerning the reference peak magnitudes obtained with the wall-mounted PCB, the pressure data reconstructed from FLDI measurements present an overall good agreement. Downstream of  $\sim 30$  mm, a consistent small difference in peak magnitudes is apparent, with the PCB data always higher. This may be an effect of the trailing secondary wave mentioned earlier. Referring again to Fig. 3, this secondary wave front follows the main one closely along the center line in the vicinity of the 30 mm station. While the FLDI is still

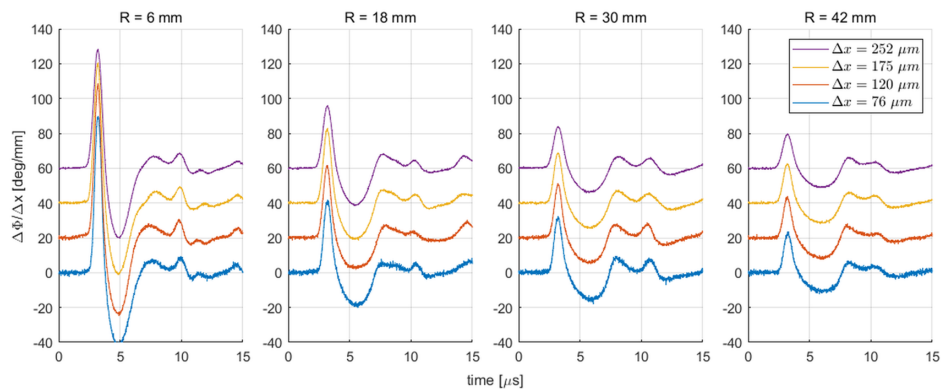


**FIG. 7.** Time signals obtained from FLDI measurements of spherical blast waves using multiple FLDI differentiation distances  $\Delta x$ , minimally post-processed. Each line is the average of ten overlapping time signals independently obtained at the same location and with the same  $\Delta x$ .

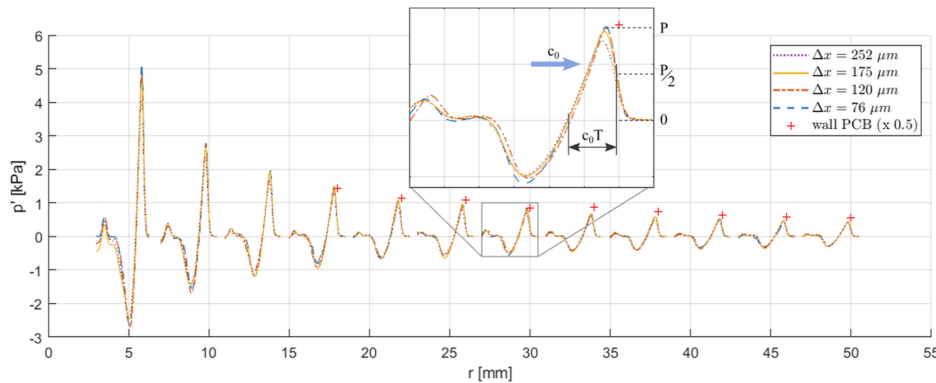


**FIG. 8.** Waveforms obtained from FLDI measurements of spherical blast waves using multiple FLDI differentiation distances  $\Delta x$ . The blast wave source is located at  $r = 0$ . Each profile is the average of eight waveforms independently obtained at the same location and with the same  $\Delta x$ . The displayed results are a subset of the complete dataset, selected for clarity such that consecutive waveforms do not overlap. The waveforms are aligned to their respective measurement location using half the peak pressure along the front of the wave. Corresponding reference peak pressures measured with a wall-mounted PCB pressure sensor are also shown where available.

capable of a clear detection of the main wave front, the interaction between the flowfield and the wall in the case of the pressure sensor favors the combination of the two waves, biasing the measured peak overpressures.

The physical analysis of the flowfield reconstructed from FLDI data can be continued by looking at the complete waveforms obtained. In addition to the peak pressure  $P$ , they also allow extracting the compression phase duration  $T$ , as illustrated in the inset of Fig. 8. To account for the finite thickness of the wave front, the value of half the peak pressure is used as a reference to obtain the compression phase duration as shown. The relationship between these two features, as expected from weak-shock theory, Eqs. (1) and (2), is analyzed next.

**B. Analysis through weak-shock theory**

The distributions of compression phase duration  $T$  from the reconstructed waveforms are shown in Fig. 9. Data for all analyzed  $\Delta x$  are shown, with an offset of one grid line between each adjacent dataset. Information obtained from the averaged pressure profiles is shown using empty symbols with dashed lines. The values obtained from each individually performed measurement are shown as filled small symbols on the background for completeness. The least-squares linear fits of  $T^2$  vs  $\log R$  for each case are shown as solid lines.

The sets of values from individual waveform regressions shown in Fig. 9 display an evident scatter toward the larger evaluated distances. This is attributed to a combination of two factors. First, small variations in the strength of the generated spark across the repetitions may yield pronounced accumulated differences as the wave propagates further away from the source. Second, as the amplitude of the detected signal becomes smaller, an eventual weak signal offset, either positive or negative, preceding the arrival of the wave front may bias the results of the integration procedure for waveform reconstruction, Eq. (12). The average of signal magnitude in a  $10 \mu s$

range before the first signal rise is used to offset the zero level, in an attempt to avoid this. However, low signal-to-noise ratios reduced the accuracy of the offset in some cases. This is further evidenced by the fact that scatter is larger for smaller  $\Delta x$  values, in which case overall smaller signal amplitudes are produced. The biasing effect is small, as will be verified next with the fluctuation of peak pressures in this region. However, its influence on the evaluation of compression phase duration may be significant. A change in peak pressure will cause a proportional change in the compression phase duration (refer to the inset in Fig. 8). With the compression phase duration

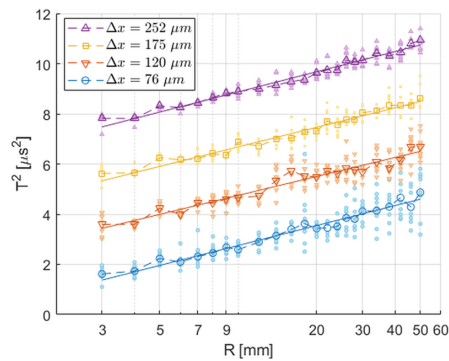


**FIG. 9.** Distribution of compression phase duration of spherical blast waves detected with FLDI using multiple differentiation distances  $\Delta x$ . Data are cascaded along the y axis with a positive offset of  $2 \mu s^2$  for each increasing  $\Delta x$  for clarity. Empty large symbols with dashed lines correspond to the mean waveforms, while filled small symbols in the background correspond to each independently regressed waveform. Linear fits for the distributions are shown as solid lines.

becoming ever larger as the wave propagates further, a small relative change in peak pressure may yield a noticeable change in the compression phase duration in terms of absolute values.

The observed scatter highlights the importance of performing repeated measurements across the probed distances. By considering the averaged waveform to obtain representative values for each location, the influence of the detailed factors is greatly reduced. This is verified by the generally low deviation between the data from averaged waveforms and a straight line, as expected from Eq. (1), and the similar slope independently obtained for each case.

Figure 10 shows the peak pressure data obtained for each case. Again, the datasets are cascaded for clarity, and values for the mean and individual waveforms are shown as empty symbols with dashed lines and filled small symbols, respectively. The comparatively low scatter of the values based on individual waveforms confirms that the non-uniformities mentioned earlier have a small effect on the peak pressures.

The complete dataset of reference peak pressures obtained with the wall-mounted PCB sensor is also shown, and repeated accordingly for each FLDI configuration. The logarithmic scale of Fig. 10 highlights the agreement between peak pressures measured with FLDI and the wall-mounted PCB for  $R \leq 30$  mm. The PCB measurements beyond that location present a vertical offset. Nonetheless, they remain described by a straight line, as would be the case with a slightly stronger blast wave. This is evidence of the combination between the main and trailing wave fronts downstream of  $R = 30$  mm, mentioned previously.

Proceeding with the analysis of the FLDI measurements, the slopes obtained from Fig. 9 are used to determine a  $\sigma_0$  for each measured value of  $T$  (refer to Sec. II A) from the averaged waveforms. The corresponding values of peak pressure  $P$  expected from the weak-shock theory are then calculated for each measurement position using Eq. (2). The resulting distribution for each case is

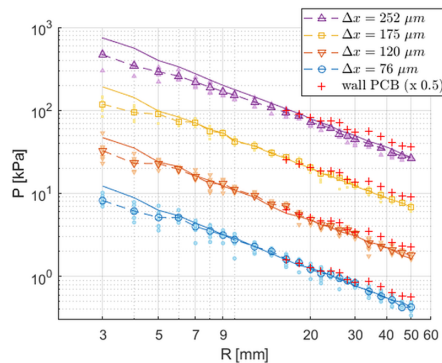


**FIG. 10.** Distribution of peak pressures of spherical blast waves, detected with the FLDI using multiple differentiation distances  $\Delta x$ . Data are cascaded along the y axis with a positive offset in factors of 4 for each increasing  $\Delta x$  for clarity. Empty large symbols with dashed lines correspond to the mean waveforms, while filled small symbols in the background correspond to each independently regressed waveform. The distributions of peak pressures expected from weak-shock theory based on mean  $T$  are shown as solid lines. Reference peak pressures measured with a wall-mounted PCB pressure sensor are also plotted where available.

shown with a solid line in Fig. 10. For the waveforms reconstructed from FLDI measurements to be physically consistent, the solid and dashed lines in Fig. 10 must overlap.

A pronounced disagreement is noticed in the vicinity of the blast wave source for  $R < 6$  mm. This may be due to a poor approximation of the blast wave as spherical in this region since the spark length is  $\sim 4$  mm. In the case of a purely spherical blast wave, e.g., generated using laser induced breakdown as in Ref. 38, it could be expected that pressures in the close vicinity of the blast wave source would be higher,<sup>39</sup> rising to match the theoretical predictions. The predictions themselves would not be expected to change, given that the slopes in Fig. 9 are a global parameter and the compression phase durations shown in that same figure seem to follow a constant slope all the way through.

Away from the blast wave source, Fig. 10 shows an overall good agreement between measured and expected values for the three lower  $\Delta x$  values, in contrast to the consistent offset observed for  $\Delta x = 252 \mu\text{m}$ . To quantify this offset, the point-wise ratios between the peak pressures measured on the FLDI waveforms  $P$  and the corresponding value expected from the weak-shock theory  $P_{\text{ws}}$  are calculated. The ratios for  $R < 6$  mm are discarded for all cases for the reason mentioned earlier. Table I shows the mean and standard deviation values of  $P/P_{\text{ws}}$  observed for each case. For the three lower values of  $\Delta x$ , the distribution of  $P/P_{\text{ws}}$  is close to and varies across unity, indicating a reasonable match between the measured pressure peaks and the weak shock predictions. Conversely, for  $\Delta x = 252 \mu\text{m}$ , a 10% offset is obtained on average, with the predicted values always greater than the measurements.

It is noted that only the separation distance  $\Delta x$  between the interferometric pair of the FLDI differentiates the four cases. These results indicate that the post-processing approach detailed in Sec. II C is able to yield physically consistent waveforms as long as the constraints imposed by the simplifications thereby listed are adequately considered. A value of  $\Delta x = 252 \mu\text{m}$  likely violates simplification (a).ii, namely, the approximation of the finite difference performed by the FLDI to a spatial derivative. This is analyzed in further detail in Secs. IV C and IV D through cFLDI calculations.

### C. Computational FLDI simulation

As seen in Sec. II C, the reconstruction of spherically propagating pressure waveforms using FLDI measurements is made possible through a series of approximations. In the following, the quality of the obtained waveforms is assessed by means of cFLDI to produce time-resolved phase difference  $\Delta\Phi(t)$  simulations based on the reconstructed flowfield  $p'(r)$ . These computational results are

**TABLE I.** Compilation of ratios between peak pressures  $P$  measured from averaged waveforms and the corresponding values expected from the weak-shock theory  $P_{\text{ws}}$ , for each FLDI configuration. The mean and standard deviation values obtained from the distribution for  $R \geq 6$  mm.

$\Delta x$	Mean $P/P_{\text{ws}}$
76 $\mu\text{m}$	$0.992 \pm 0.055$
120 $\mu\text{m}$	$1.033 \pm 0.065$
175 $\mu\text{m}$	$1.009 \pm 0.045$
252 $\mu\text{m}$	$0.894 \pm 0.054$

compared with the original experimental data. An accurate reconstruction must produce overlapping simulated results, meaning this cycle between measured or simulated  $\Delta\Phi$  and reconstructed  $p'$  may go on indefinitely without any loss of information.

This approach is made possible by recalling that the methods of flowfield reconstruction and cFLDI simulation are entirely independent from each other, as seen in Sec. II. Since the ray-tracing cFLDI is physically accurate, a match between the simulation of a flowfield reconstructed from experiments and the experimental data that originated it implies that the reconstruction is also accurate (provided the possibility of non-unique solutions can be neglected). Any deviation between computed and experimental data is, therefore, an indication of flaws in the flowfield reconstruction procedure.

Figure 11 illustrates how the cFLDI perceives the passage of the blast wave. The wave front is marked with a darkened surface, and the FLDI beams are painted according to the instantaneous local density distribution. Due to the small time of interaction between the FLDI and the disturbance carried by the blast wave, the shape of the disturbance is assumed to be frozen in time and moving radially with a constant velocity. The temporal resolution for the computational FLDI calculations is chosen to be 20 MHz, based on a convergence analysis similar to the one presented for the mesh discretization in Sec. III B.

Careful evaluation of the reconstructed flowfield was conducted at  $R = 30$  mm for all four  $\Delta x$  values. The observations presented next are specific to this probing location, but the methodology is general.

An averaged experimental time-resolved phase difference  $\Delta\Phi$  was obtained for each differentiation distance  $\Delta x$ , and processed into a spatially resolved pressure flowfield to be simulated with cFLDI. The approach with averaged experimental data has the benefit of smoothing out eventual flowfield imperfections while keeping the signal main features. A clear reference is thus obtained to compare the computational results after completing

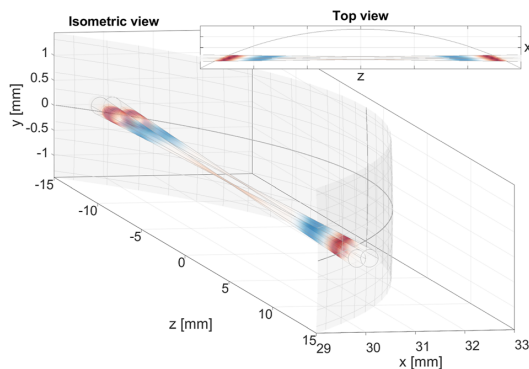


**FIG. 11.** Illustration of the computational FLDI of a blast wave, in isometric and top views. Colors are contours of density perturbation within the FLDI domain, with positive and negative variations indicated as tones of red and blue, respectively. The FLDI bundle is positioned 30 mm away from the blast wave source, with beams  $252 \mu\text{m}$  apart in this example. At the moment of this snapshot, the blast wave radius is  $\sim 32.7$  mm. The wave front is marked by a darkened surface.

the reconstruction–simulation cycle, improving the detection of eventual differences stemming from the reconstruction procedure.

Figure 12 shows the comparison between experimental and computed data. Results are displayed as the ratio between phase difference  $\Delta\Phi$  and beam separation  $\Delta x$ . With such scaling, all lines are ideally identical regardless of FLDI configuration since the same disturbance field is probed at the same location across the cases. A vertical offset of  $20^\circ/\text{mm}$  is used between adjacent cases for clarity. The time origin in each case is arbitrarily defined such that the peak signals are aligned to facilitate visual comparison. The gray lines in the main plot show the original experimental data in each case, with colors denoting the cFLDI output of the corresponding reconstructed pressure waveforms.

The experimental signals across all four cases are verified to present a similar general form. All time series show the detection of the main wave front starting at  $\sim 2.5 \mu\text{s}$  and the previously mentioned secondary wave front close to  $10 \mu\text{s}$ . The most noticeable difference is more apparent noise as  $\Delta x$  is smaller, which is a consequence of the overall lower signal amplitudes obtained with a small differentiation distance. The signals displayed as  $\Delta\Phi/\Delta x$  represent a finite difference approximation of a spatial derivative. Considering the reduction of non-uniformities through averaging repeated measurements, the flowfield is essentially the same for all cases. Therefore, all experimental signals are ideally the same in terms of  $\Delta\Phi/\Delta x$ , as long as  $\Delta x$  is small enough. The experimental lines in Fig. 12 show this to be the case for  $\Delta x = 76$  and  $120 \mu\text{m}$ . For the higher  $\Delta x$ , a reduction in peak value and a damping of gradients are observed, especially for  $\Delta x = 252 \mu\text{m}$ . Those are indications that the finite difference operated by the FLDI is not performed across a small enough spatial interval to adequately represent a spatial derivative in this flowfield.

More insight can be gained from the cFLDI results. The colored lines in the main plot of Fig. 12 show that all four cases are mostly

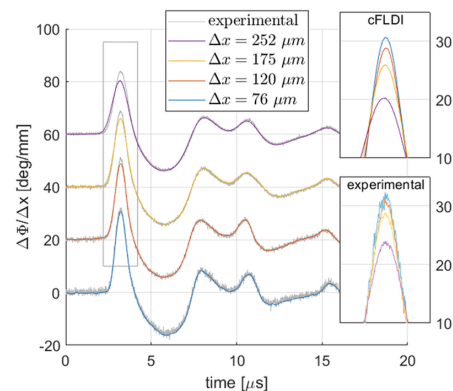


**FIG. 12.** Comparison of FLDI response to spherical blast waves, detected at 30 mm from the source using multiple FLDI differentiation distances  $\Delta x$ . Magnitudes are the ratio of phase difference to beam separation distance, offset in multiples of  $20^\circ/\text{mm}$ . Time origins are arbitrarily defined. The gray lines correspond to experimental measurements; colors represent the cFLDI response to the reconstructed disturbance field. The insets on the right refer to the box in the main plot with the vertical offsets removed, offering a direct comparison between the peak values of each experimental and cFLDI dataset.

well reproduced. The exceptions concern the sharp signal rise upon blast wave arrival. For  $\Delta x = 252$  and  $175 \mu\text{m}$ , a damping of gradient and reduction of peak value are again observed, more evidently for the former. This corroborates the previous observations concerning the experimental results. At this point, flowfield feature losses due to inadequate FLDI configuration have taken place twice: once when the experimental measurements were performed and again when the computational FLDI responses were simulated. The computational FLDI results in Fig. 12 also evidence small differences in peak values for  $\Delta x = 120 \mu\text{m}$  (and very small for  $\Delta x = 76 \mu\text{m}$ ).

Table II evaluates these disagreements. For each  $\Delta x$ , the relative peak signal difference and the zero-lag cross-correlation between experimental and computational FLDI for the main wave front (between 1 and  $10 \mu\text{s}$  in Fig. 12) are given. The cross-correlation is normalized by the auto-correlation of the experimental signal, such that both shape and amplitude differences result in a departure from unity. The listed values evidence the influence of  $\Delta x$  on the ability to return the reconstructed flowfield back into FLDI data. For the smallest evaluated  $\Delta x$ , good agreement is confirmed, with a loss in peak value of less than 3% and the overall time signal from the FLDI simulation correlating with the experimental one at 0.5%.

These observations allow the definition of two types of inaccuracies. First, on the ability of the FLDI as an instrument to detect strong gradients due to finite differentiation. Second, on the effect of simplifications adopted in Sec. II C to allow reconstruction of the blast wave flowfield from FLDI measurements. The former is seen in the raw experimental data as the signals present loss of features if  $\Delta x$  is above a certain threshold ( $\Delta x > 120 \mu\text{m}$ , in this case) and is unrelated to the post-processing methodology. The latter is verified when the physically accurate computational FLDI fails to reproduce the experimental signal from which the flowfield was obtained, therefore being of relevance in this work.

Interestingly, the cFLDI indicates a noticeable peak signal loss for  $\Delta x = 120 \mu\text{m}$  even though the experimental signal used to reconstruct the waveform was seemingly sufficiently resolved, as indicated by the nearly identical experimental  $\Delta\Phi/\Delta x$  for  $\Delta x = 120$  and  $76 \mu\text{m}$ . Furthermore, it is noted that the differences observed in Fig. 12 and reported in Table II are mostly subtle for all cases other than  $\Delta x = 252 \mu\text{m}$ . It is evidenced that the comparison between measured and expected values of the reconstructed waveforms performed in Sec. IV B was only able to identify flaws for the highest  $\Delta x$ , despite the cFLDI results presenting discrepancies against the experimental data for other  $\Delta x$  values as well. This highlights the contribution of

**TABLE II.** Quantitative comparison between experimental FLDI data and the cFLDI output to the reconstructed disturbance field. Values concern the spherical blast wave detected 30 mm from its source using multiple FLDI differentiation distances  $\Delta x$ . The peak signal difference is relative to the experimental signal, and the cross-correlation coefficient is normalized by the auto-correlation of the experimental signal.

$\Delta x$	Relative peak signal difference (%)	Normalized cross-correlation coefficient
$76 \mu\text{m}$	2.74	0.9950
$120 \mu\text{m}$	6.12	0.9849
$175 \mu\text{m}$	9.20	0.9704
$252 \mu\text{m}$	14.48	0.9556

the cFLDI analysis to verify post-processing approaches, especially in the absence of parallel, reliable measurements to provide further support. These results are analyzed in more detail next, in view of the methodology proposed in Sec. II C and the list of simplifying hypotheses presented in its closing paragraph.

#### D. Analysis of post-processing simplifications

It is first noted that agreement between experimental and computational results presented in Sec. IV C was obtained for at least one  $\Delta x$  while all other FLDI parameters remained unchanged. This indicates that simplifications such as neglecting the divergence of the beams and their finite volume, hypothesis (a).i, do not significantly interfere with the field reconstruction for a blast wave and FLDI setup with the dimensions presented here. An investigation of this hypothesis can be performed through the cFLDI simulation of a hypothetical instrument in which only one of the beams crosses the disturbance field, the other remaining unaffected as if it was a reference beam. In the case of this single beam FLDI, the output of Eq. (12) from Sec. II C is used directly in Eq. (17) without the steps concerning the conversion of density differences into density fluctuation magnitude. This is similar to the Mach-Zehnder interferometer simulation in Ref. 31, with the additional capability of having a full three-dimensional beam in the present cFLDI. By comparing the input flowfield with the flowfield reconstructed from this single beam instrument output, it is possible to assess the effects pertaining to beam divergence in an isolated manner. The comparison between an input flowfield and the reconstruction from a single beam FLDI simulation using different beam divergence angles is shown in Fig. 13. The acoustic pressure of the blast wave at  $R = 30 \text{ mm}$  is used as the reference flowfield. The results confirm that the effect of beam divergence angle for the FLDI setup used in the experiments is negligible, while for much larger angles, it would become relevant. In the case reported here, the effect observed in Fig. 13 is caused by an interaction between the wave front and the

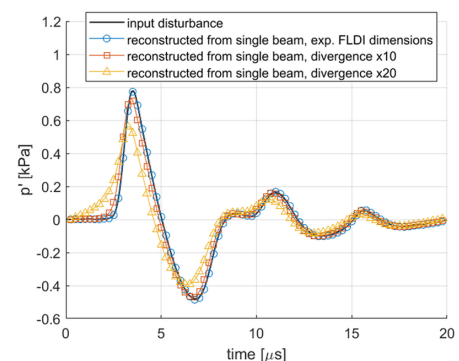


**FIG. 13.** Input blast wave acoustic pressure distribution in time, compared to reconstructed values from single beam computational FLDI simulations. Three different beam divergence angles are used in the simulations, namely, the divergence corresponding to the experimental setup in the present work ( $\sim 0.7^\circ$ ), 10 times this value, and 20 times this value.

wide radius of the FLDI beams away from the focal plane before the blast wave reaches the FLDI focus.

Next, regarding the loss of accuracy as  $\Delta x$  becomes larger, an oversimplification regarding the finite beam separation, hypothesis (a).ii, is evidenced. This finite distance was disregarded when approximating the integral limits in Eq. (9) and the derivative in Eq. (14). These approximations can be analyzed separately as follows.

The approximation of the derivative through finite differences is a central hypothesis in the reconstruction method since the density value at each instant depends on the preceding value and the derivative following Eq. (16). An error in the finite difference approximation would misrepresent the local gradient, which in turn would introduce a local magnitude offset that would propagate to all subsequent points. In addition, recall that the flowfield reconstruction is performed spatially from outside the blast wave toward the inside. Hence, in the temporal simulated data in Fig. 12, the accumulated offset would become more significant at later times as the inner portions of the blast wave reach and travel through the FLDI location. Figure 12 shows that even for the largest  $\Delta x$ , the disagreement between experimental and computational results is limited to the first instants after blast wave arrival, with accurate reproduction later on. Therefore, the finite difference approximation is verified to be reasonable. This observation concerns the flowfield reconstruction method alone, even when the instrument itself might be ill-conditioned to perform the detection as mentioned for the larger values of  $\Delta x$  in the present case.

Conversely, the approximation of the integral limit can be particularly inaccurate in the brief moments following blast wave arrival. During this time interval, the disturbance field affects exclusively the upstream beam, and the combination of the integrals from Eq. (4) through the approximation described in Eq. (9) is not valid. A representative distribution of derivatives in this region is still obtained, but the precise conversion to radial quantities in Eq. (12) is affected. Evidently, the time interval in which this misrepresentation is observed (and hence its effect) increases with increasing beam separation  $\Delta x$ . Figure 12 shows that for the blast wave measurements presented here, the influence of the misrepresentation is negligible for  $\Delta x = 76 \mu\text{m}$ , while for  $\Delta x \geq 120 \mu\text{m}$  it is not.

A parametric study was conducted using the experimental data and the cFLDI to evaluate this effect. For every probing location and FLDI configuration, a pressure waveform was reconstructed from the experiment. By including multiple probing locations, waveforms of different characteristics are considered, as previously illustrated in Fig. 8. Each waveform was simulated in a cFLDI using several values of  $\Delta x$ , encompassing smaller, identical, and larger values than the experimental ones.

Figure 14 displays an overview of the observed results. On the y axis of the figure, the difference in the simulated FLDI peak value with respect to each experimental counterpart is represented as a percentage of loss. The abscissa shows the cFLDI differentiation distance  $\Delta x$  used in each simulation, normalized by the width of the compression front of the simulated waveform. Here, the width of the compression front refers to the first rising portion of the traveling pressure waveform, objectively defined as twice the distance between the waveform maximum pressure  $P$  and  $P/2$  upstream of it, as annotated in the inset of Fig. 8. This normalization parameter is proposed to represent a region of strong gradients with a length across which

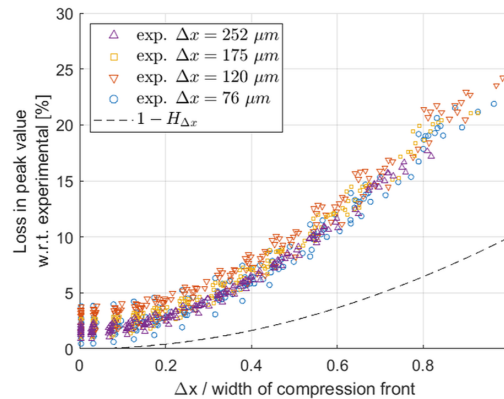


**FIG. 14.** Compilation of peak signal comparisons from parametric cFLDI analysis, performed over multiple probing locations and with different FLDI configurations. The y axis shows the percentage of loss on the peak of the cFLDI signal in terms of  $\Delta\Phi/\Delta x$  with respect to the original experimental FLDI measurement used to obtain the computational flowfield. The x axis shows the value of FLDI differentiation distance  $\Delta x$ , normalized by the width of the compression front of each simulated pressure waveform. A reference value of expected loss due to finite differentiation is also given as  $1 - H_{\Delta x}$ , with  $H_{\Delta x}$  being the transfer function corresponding to the finite difference.

the approximation of identical integral limits would not hold well. With the variation of FLDI differentiation distance reaching magnitudes comparable to a flowfield length scale, it becomes important to monitor losses caused by finite differentiation as well. This effect and that of the integral limit approximation overlap as functions of the differentiation distance and, therefore, cannot be analyzed separately. Nonetheless, an important distinction between these two effects is that the finite difference is physical, while the integral limit approximation pertains only to the flowfield reconstruction method. As such, the former is present in both experimental and computational FLDI, but the latter is exclusive to the cFLDI simulation. The transfer function describing the effect of finite differentiation distance as a function of wavenumber is given in Refs. 2 and 21 as  $H_{\Delta x}(k) = \text{sinc}(\Delta x \cdot k/2)$ . The transfer function is used to calculate the loss in FLDI response magnitude expected for multiple values of  $\Delta x \cdot k$ , or  $\Delta x \cdot 2\pi/\lambda$  in terms of disturbance wavelength, which is shown in Fig. 14. The width of the compression front used as the normalization parameter in the figure is assumed to be 1/4 of the wavelength of an equivalent sinusoidal disturbance.

It is first noted that for all cases, the loss in peak value is larger than the expected damping due to finite differentiation. This confirms that the approximation of the integral limit is the most constraining factor in the present flowfield reconstruction method. The results show a monotonic relationship between the cFLDI differentiation distance  $\Delta x$  and the ability of the simulated setup to reproduce the experimental signal, with lower values of  $\Delta x$  producing the best results. Furthermore, the width of the compression front of the probed waveform as a normalizing factor for  $\Delta x$  was able to approximately collapse this relationship, regardless of experimental FLDI configuration or probing location (the latter associated

with different widths of the compression front, recall Fig. 8). The apparent larger spread of the points pertaining to the smaller experimental  $\Delta x$  is related to the lower signal-to-noise ratio in those cases, which introduces larger uncertainties in the determination of reference magnitudes. It is verified that for values of  $\Delta x$  less than 0.2 times the width of the flowfield compression front, the loss in the simulated value becomes a minimum, subject to other factors that may become dominant.

This general rule may be applied to the cases evaluated before, concerning the probing location of 30 mm away from the spark source, for verification. Using as a reference the experimental data obtained with  $\Delta x = 76 \mu\text{m}$ , the obtained compression front width was  $\sim 0.32$  mm. It is noted that  $\Delta x = 76 \mu\text{m}$  is close to 0.2 times this value, whereas  $\Delta x = 120, 176, \text{ or } 252 \mu\text{m}$  are much higher, with losses indicated by Fig. 14 that are compatible with the ones reported in Table II.

## V. CONCLUSION

This work presented a new, analytic post-processing methodology to extract quantitative information from Focused Laser Differential Interferometry (FLDI) measurements of flowfields possessing circular symmetry. In the absence of complementary experimental data for complete direct comparisons, a physically accurate computational FLDI was employed as a tool to assess the accuracy of the approach. Constraining conditions were identified, and the methodology was confirmed to be reasonable if these conditions are met.

The methodology was applied and analyzed in FLDI measurements of spark-generated spherical weak blast waves, using multiple FLDI differentiation distances and probing locations. In a first verification effort, the reconstructed pressure waveforms agreed with predictions from weak-shock theory at distances larger than 6 mm from the spark source, below which the approximation of a spherical blast wave used by the theoretical model is not adequate. The agreement was observed for all but the largest differentiation distance, namely,  $\Delta x = 252 \mu\text{m}$ , which showed consistently lower peak pressure values. Where allowed by experimental constraints, reference peak pressure values were obtained using a wall-mounted fast response piezoelectric pressure sensor. Comparisons between these references and the peak pressure magnitudes of the reconstructed waveforms provided similar observations.

An in-depth analysis of the reconstructed flowfield using cFLDI simulations helped identify further inaccuracies not captured in the theoretical comparisons, in terms of both peak signal amplitude and gradient damping. The simplification of equal integration lengths between the two beams composing the FLDI interferometric pair was identified as the most critical in the post-processing operations. Nonetheless, very good agreement was obtained between the computational FLDI for  $\Delta x = 76 \mu\text{m}$  applied to the reconstructed flowfield and the experimental FLDI which gave origin to it. Differences were evaluated as less than 3% restricted to the close vicinity of the peak signal, and cross-correlation between the signals including all features agreed to 0.5%. The proposed post-processing methodology was hence verified to be sound, as long as a small enough  $\Delta x$  is employed. This threshold was evaluated by means of a parametric analysis using the cFLDI, as 20% or less of the length of

the compression front, which represents a reference of strong spatial variation of density in the flowfield studied here.

It must be highlighted that the quantitative results presented in this work are specific to the blast wave flowfield investigated herein. Flowfields with different features or length scales might have different sensitivities to either  $\Delta x$  or other FLDI system properties. Nonetheless, the methodology of using cFLDI to evaluate such sensitivities can be extrapolated to different investigations. The approach detailed here is therefore recommended for any particular application, to ensure proper consideration of limiting constraints and obtain accurate post-processing output. The depth of insight offered by cFLDI as exemplified in this work is a strong argument for encouraging the widespread application of such simulations as an instrument of analysis.

## ACKNOWLEDGMENTS

The support given by Professor Dr. Klaus Hannemann and Professor Dr. Peter J. Klar is deeply appreciated. The authors also wish to acknowledge the assistance of the HEG team, in particular Ingo Schwendtko, Uwe Frenzel, Fabian Glasewald, Jan Martinez Schramm, and Divek Surujhlah.

## AUTHOR DECLARATIONS

### Conflict of Interest

The authors have no conflicts to disclose.

## Author Contributions

**Giannino Ponchio Camillo:** Methodology (lead); Writing – original draft (lead). **Alexander Wagner:** Supervision (lead); Writing – review & editing (lead).

## DATA AVAILABILITY

The data that support the findings of this study are available from the corresponding author upon reasonable request.

## REFERENCES

- <sup>1</sup>N. Parziale, “Slender-body hypervelocity boundary-layer instability,” Ph.D. thesis, California Institute of Technology, Pasadena, CA, 2013.
- <sup>2</sup>M. R. Fulghum, “Turbulence measurements in high-speed wind tunnels using focusing laser differential interferometry,” Ph.D. thesis, The Pennsylvania State University, PA, 2014.
- <sup>3</sup>J. S. Jewell, N. J. Parziale, K.-L. Lam, B. J. Hagen, and R. L. Kimmel, “Disturbance and phase speed measurements for shock tubes and hypersonic boundary-layer instability,” in *32nd AIAA Aerodynamic Measurement Technology and Ground Testing Conference* (American Institute of Aeronautics and Astronautics, 2016).
- <sup>4</sup>A. Ceruzzi and C. P. Cadou, “Simultaneous velocity and density gradient measurements using two-point focused laser differential interferometry,” in *AIAA Scitech 2019 Forum* (American Institute of Aeronautics and Astronautics, 2019).
- <sup>5</sup>E. K. Benitez, J. S. Jewell, and S. P. Schneider, “Focused laser differential interferometry for hypersonic flow instability measurements with contoured tunnel windows,” in *AIAA Scitech 2020 Forum* (American Institute of Aeronautics and Astronautics, 2020).

- <sup>6</sup>B. F. Bathel, J. M. Weisberger, G. C. Herring, R. A. King, S. B. Jones, R. E. Kennedy, and S. J. Laurence, "Two-point, parallel-beam focused laser differential interferometry with a Nomarski prism," *Appl. Opt.* **59**, 244–252 (2020).
- <sup>7</sup>M. Gragston, T. Price, K. Davenport, Z. Zhang, and J. D. Schmisser, "Linear array focused-laser differential interferometry for single-shot multi-point flow disturbance measurements," *Opt. Lett.* **46**, 154–157 (2021).
- <sup>8</sup>G. P. Camillo and A. Wagner, "A low-effort and inexpensive methodology to determine beam separation distance of multi-foci FLDI," *Exp. Fluids* **63**, 53 (2022).
- <sup>9</sup>N. J. Parziale, J. E. Shepherd, and H. G. Hornung, "Observations of hypervelocity boundary-layer instability," *J. Fluid Mech.* **781**, 87–112 (2015).
- <sup>10</sup>E. K. Benitez, S. Esquieu, J. S. Jewell, and S. P. Schneider, "Instability measurements on an axisymmetric separation bubble at Mach 6," in *AIAA AVIATION 2020 FORUM* (American Institute of Aeronautics and Astronautics, 2020).
- <sup>11</sup>Y. Xiong, T. Yu, L. Lin, J. Zhao, and J. Wu, "Nonlinear instability characterization of hypersonic laminar boundary layer," *AIAA J.* **58**, 5254–5263 (2020).
- <sup>12</sup>K. J. Hopkins, H. Porat, T. J. McIntyre, V. Wheatley, and A. Veeraragavan, "Measurements and analysis of hypersonic tripped boundary layer turbulence," *Exp. Fluids* **62**, 164 (2021).
- <sup>13</sup>F. Siddiqui, M. Gragston, and R. D. W. Bowersox, "Measurement of wall-cooling effects on hypersonic boundary-layer transition using focused laser differential interferometry," *AIAA J.* **60**, 6214–6224 (2022).
- <sup>14</sup>G. S. Settles and M. R. Fulghum, "The focusing laser differential interferometer, an instrument for localized turbulence measurements in refractive flows," *J. Fluids Eng.* **138**, 101402 (2016).
- <sup>15</sup>B. Birch, D. Buttsworth, and F. Zander, "Measurements of freestream density fluctuations in a hypersonic wind tunnel," *Exp. Fluids* **61**, 158 (2020).
- <sup>16</sup>A. Hameed and N. J. Parziale, "Focused laser differential interferometry transfer functions for complex density disturbance fields," in *AIAA AVIATION 2021 FORUM* (American Institute of Aeronautics and Astronautics, 2021).
- <sup>17</sup>A. Hameed and N. J. Parziale, "Focused laser differential interferometric investigation of turbulent jet spectra," *J. Spacecr. Rockets* **59**, 1565–1573 (2022).
- <sup>18</sup>A. P. Ceruzzi and C. P. Cadou, "Interpreting single-point and two-point focused laser differential interferometry in a turbulent jet," *Exp. Fluids* **63**, 112 (2022).
- <sup>19</sup>A. P. Ceruzzi, "Development of two-point focused laser differential interferometry for applications in high-speed wind tunnels," Ph.D. thesis, University of Maryland, College Park, MD, 2022.
- <sup>20</sup>A. Ceruzzi, C. Neisess, B. McManamen, and C. P. Cadou, "Investigation of focused laser differential interferometry (FLDI) sensitivity function," in *AIAA Scitech 2021 Forum* (American Institute of Aeronautics and Astronautics, 2021).
- <sup>21</sup>J. M. Lawson, "Focused laser differential interferometry," Ph.D. thesis, California Institute of Technology, Pasadena, CA, 2021.
- <sup>22</sup>J. M. Lawson, M. C. Neet, J. W. Hofferth, and J. M. Austin, "Supersonic freestream density fluctuations from focused laser differential interferometry and pitot-probe measurements," *AIAA J.* **60**, 5173–5186 (2022).
- <sup>23</sup>B. E. Schmidt and J. E. Shepherd, "Analysis of focused laser differential interferometry," *Appl. Opt.* **54**, 8459–8472 (2015).
- <sup>24</sup>J. M. Lawson, M. C. Neet, I. J. Grossman, and J. M. Austin, "Static and dynamic characterization of a focused laser differential interferometer," *Exp. Fluids* **61**, 187 (2020).
- <sup>25</sup>J. M. Lawson and J. M. Austin, "Focused laser differential interferometer response to shock waves," *Meas. Sci. Technol.* **32**, 055203 (2021).
- <sup>26</sup>E. K. Benitez, M. P. Borg, C. Rhodes, and J. S. Jewell, "Optical-axis spatial sensitivity of a simulated focused laser differential interferometer," *AIAA J.* **1–14** (2023).
- <sup>27</sup>E. K. Benitez and J. S. Jewell, "Simulated focused laser differential interferometry of time-varying signals," in *AIAA SCITECH 2022 Forum* (American Institute of Aeronautics and Astronautics, 2022).
- <sup>28</sup>E. K. Benitez, M. P. Borg, J. Luke Hill, M. T. Aultman, L. Duan, C. L. Running, and J. S. Jewell, "Quantitative focused laser differential interferometry with hypersonic turbulent boundary layers," *Appl. Opt.* **61**, 9203–9216 (2022).
- <sup>29</sup>G. F. Kinney and K. J. Graham, *Explosive Shocks in Air*, 2nd ed. (Springer Berlin Heidelberg, New York, 1985).
- <sup>30</sup>A. D. Pierce, *Acoustics*, 3rd ed. (Springer International Publishing, Switzerland, 2019).
- <sup>31</sup>P. Yuldashev, M. Karzova, V. Khokhlova, S. Ollivier, and P. Blanc-Benon, "Mach-Zehnder interferometry method for acoustic shock wave measurements in air and broadband calibration of microphones," *J. Acous. Soc. Am.* **137**, 3314–3324 (2015).
- <sup>32</sup>W. M. Wright, "Propagation in air of  $N$  waves produced by sparks," *J. Acous. Soc. Am.* **73**, 1948–1955 (1983).
- <sup>33</sup>M. Born and E. Wolf, *Principles of Optics*, 7th ed. (Cambridge University Press, Cambridge, UK, 1999).
- <sup>34</sup>M. M. Karzova, P. V. Yuldashev, V. A. Khokhlova, S. Ollivier, E. Salze, and P. Blanc-Benon, "Characterization of spark-generated  $N$ -waves in air using an optical schlieren method," *J. Acous. Soc. Am.* **137**, 3244–3252 (2015).
- <sup>35</sup>Deutsches Zentrum für Luft- und Raumfahrt (DLR), "The High Enthalpy Shock Tunnel Göttingen of the German Aerospace Center (DLR)," *J. Large-Scale Res. Facil.* **4**, A133 (2018).
- <sup>36</sup>S. R. Sanderson, "Simple, adjustable beam splitting element for differential interferometers based on photoelastic birefringence of a prismatic bar," *Rev. Sci. Instrum.* **76**, 113703 (2005).
- <sup>37</sup>J. M. Lawson, M. C. Neet, I. J. Grossman, and J. M. Austin, "Characterization of a focused laser differential interferometer," in *AIAA Scitech 2019 Forum* (American Institute of Aeronautics and Astronautics, 2019).
- <sup>38</sup>B. F. Bathel, J. M. Weisberger, G. C. Herring, R. Jagannathan, C. T. Johansen, S. B. Jones, and A. A. Cavone, "Analysis of the amplitude response of a two-point and a multi-point focused laser differential interferometer," in *AIAA Scitech 2021 Forum* (American Institute of Aeronautics and Astronautics, 2021).
- <sup>39</sup>G. G. Bach and J. H. S. Lee, "An analytical solution for blast waves," *AIAA J.* **8**, 271–275 (1970).

### 3.3. Hypersonic turbulent boundary layer investigation using FLDI (Publication 3)

As a result of the two published works shown so far, a carefully measured quad-foci FLDI setup and a validated computational FLDI algorithm were available to perform shock tunnel investigations. The experimental setup was developed from the beginning with the large dimensions necessary for application in the High-Enthalpy Shock Tunnel Göttingen (HEG) [84]. The necessary distance between the field lenses and the focus of the system was approximately 1.9 m, to account for the width of the test section and the swing-opening access windows.

The flowfield of interest to the present work was a turbulent boundary layer over a  $7^\circ$  half-angle conical model with cold walls under hypersonic free stream conditions of Mach 7.4 and unit Reynolds number  $4.2 \times 10^6 \text{ m}^{-1}$ .

In preparation for the experiments, the FLDI had been test-run on previous HEG campaigns to identify and improve upon practical constraints. One noteworthy effort was to design the quad-foci FLDI such that all four beams described parallel trajectories across the probed volume. This requires proper consideration of the combined behavior of the multiple optical components that are employed to produce the multi-foci FLDI, which is not observed in many works. The adopted solution has been reported by other authors [62, 71], namely to ensure that all beams cross the optical axis at the position of the Sanderson prism on the emitting side. Ensuring beam parallelism across the test section improves the accuracy of convection velocity measurements, which could otherwise be biased by variable separation distances between the pairs of FLDI probes used for velocimetry. Furthermore, it was observed that the signal cross-correlation profile around the peak value was significantly narrower when using parallel beams, in comparison to preliminary tests where this condition had not yet been enforced. The narrow cross-correlation profile around the peak value improves the precision of the measurements, as uncertainty can be inferred from the width of this profile.

Another topic that received special attention concerned maximizing the frequency bandwidth of the system, which presents competing limitations. On the side of the measurement instrument, the differentiation distance of the FLDI beams imposes a minimum wavelength in space, which translates to a maximum frequency in time, that can be resolved, determined by the Nyquist theorem. However, by lowering this distance, signal magnitudes become weaker, with impact on the side of signal acquisition, which must consider the signal-to-noise ratio (SNR). This is addressed by boosting the acquired signal through amplification, which is achieved by either adding a large termination resistance on the system's photodetector or using an external amplifier. The former has the negative effect of decreasing the frequency bandwidth of the photodetector itself, in terms of time response. Therefore, the use of an external high-bandwidth signal amplifier was preferred.

It must be noted that two different sampling limits are imposed: a spatial one determined by the FLDI differentiation distance, and a temporal one determined by the acquisition system. Furthermore, in order to adequately capture not only the frequency of the flowfield fluctuations but also their magnitudes, it is a good practice to employ a sampling rate at least a few times higher than the Nyquist

limit. A configuration was used for the present experiments in which the boundary layer FLDI signal was larger than the noise floor up to nearly 10 MHz. The spatial sampling limit was equivalent to approximately 22 MHz, the photodiodes were used with a nominal bandwidth of 25 MHz, and the data acquisition rate was 100 MHz.

For the computational flowfield, a Large-Eddy Simulation (LES) of the cone under the experimentally obtained HEG free stream conditions was calculated [85], in a cooperation between the Institute of Aerodynamics and Flow Technology at DLR and the Compressible Flow and Acoustics lab of the School of Mechanical Engineering at the Purdue University (USA). A total volume of flowfield with  $1280 \times 128 \times 112$  grid points (streamwise  $\times$  wall-normal  $\times$  azimuth) was simulated for a total time of 1.43 ms. A slice of  $40 \times 128 \times 112$  grid points was extracted with 14 ns temporal resolution to be used in the cFLDI simulations. This extracted volume spanned  $\sim 10$  mm in the streamwise direction starting at 824.6 mm from the nose of the cone along its axis,  $\sim 40$  mm in the wall-normal direction starting flush with the model wall, and  $18^\circ$  total azimuth, totaling approximately  $15 \text{ cm}^3$  of flowfield. With these dimensions, the straight line of the FLDI describes a secant on the circular boundaries of the boundary layer with intersections inside the simulated volume at and above 80% of the boundary layer thickness.

Concerning the frequency bandwidth of the numeric flowfield, the temporal resolution was initially chosen to be of the same order of magnitude as the experiments. Other factors have showed to be more constraining, namely the spatial resolution and an explicit spatial filtering required for numerical stability. The mesh refinement was such that the smallest detectable disturbances were equivalent to approximately 4 MHz. However, the spatial filtering to ensure stability of the computations lowered this limit to 1 MHz. For the experimental and numerical direct comparisons in the present work, this was the upper limit that was used. It should be noted that it is possible to use the results of the present work to optimize future computational efforts, to allow expanding this frequency limit in a cost-effective manner.

In the third publication, experimental measurements of convection velocity and frequency spectra performed with FLDI inside and above a turbulent hypersonic boundary layer are shown, as well as experimental and numerical comparisons of FLDI data under the same flowfield conditions. With regard to the experiments, the convection velocities of density disturbances measured in the free stream are consistent with previous data in the literature, corresponding to neighboring Mach numbers and based on pressure disturbances. Inside the boundary layer, literature data was scarce and available only for different flowfield conditions, with lower Mach numbers and higher wall temperatures. Still, the measured convection velocities showed similar magnitudes relative to free stream as those reports, even though the distribution across the boundary layer was different. The experimental frequency distributions evidenced regions with clear power laws in agreement with those expected for pressure fluctuations. Considering the numeric data, a careful analysis of the valid frequency bandwidth in which to perform the comparisons was conducted and explained in detail. In that analysis, a transfer function of the FLDI spatial filtering effect was used. The chosen equation is commonly presented in the literature, but further detail about it is seldom given. A demonstration of the transfer function is, therefore, given in Appendix B. Within the bounds identified by the analysis, the computational and experimental FLDI compared well. It was also verified that a simplified approach to replace the complete cFLDI algorithm with a line integral

in the numeric flowfield was able to produce similar results. The relevance of these observations is to confirm that experimental FLDI data may be used in combination with computational studies of hypersonic turbulence without the need for complex experimental post-processing strategies, or even sophisticated cFLDI algorithms, once some conditions are met. This represents a positive outlook for future studies to develop and test turbulence models for hypersonic flowfields, turbulence production strategies in high-fidelity computations, among other applications.

Conceptualization of the ideas leading to this publication was performed by me, A. Wagner, C. Scalo, and T. Toki. The objectives and planning of the experimental campaign were defined by me. Preparation of the experimental model and operation of the shock tunnel were conducted by I. Schwendtke, U. Frenzel, and F. Glasewald. The optical measurement techniques, namely schlieren and FLDI, were prepared and adjusted by me. The experimental investigation was performed by me and A. Wagner, with assistance from D. Surujhlal and J. M. Schramm. RANS computations of the nozzle flowfield were performed by M. Laureti. The LES development and computations were performed by T. Toki and E. Gil Torres. Curation of the data used in the paper was conducted by me concerning FLDI, and T. Toki concerning LES. Development of the cFLDI software was conducted by me. The methodology of analyses was developed by me. Analyses of the experimental and numerical data were conducted by me, with technical discussions involving the coauthors. Supervision of the work was conducted by A. Wagner and C. Scalo. The manuscript was written by me, and edited by the coauthors. The article is Open Access under the terms and conditions of the Creative Commons Attribution (CC BY) license (<http://creativecommons.org/licenses/by/4.0/>). It was published in *Aerospace*, **2023**, *10* (6), 570. (DOI: <https://doi.org/10.3390/aerospace10060570>)

**Copyright © 2023 by the authors.**

Article

# Combined Experimental and Numerical Investigation of a Hypersonic Turbulent Boundary Layer by Means of FLDI and Large-Eddy Simulations

 Giannino Ponchio Camillo <sup>1,\*</sup> , Alexander Wagner <sup>1,\*</sup> , Takahiko Toki <sup>2</sup>  and Carlo Scalo <sup>2</sup> 
<sup>1</sup> German Aerospace Center (DLR), Institute of Aerodynamics and Flow Technology, 37073 Göttingen, Germany

<sup>2</sup> School of Mechanical Engineering, Purdue University, West Lafayette, IN 47907, USA

\* Correspondence: giannino.ponchiocamillo@dlr.de (G.P.C.); alexander.wagner@dlr.de (A.W.)

**Abstract:** This work investigates a hypersonic turbulent boundary layer over a  $7^\circ$  half angle cone at a wall-to-total temperature ratio of 0.1,  $M_\infty = 7.4$  and  $Re_{\infty m} = 4.2 \times 10^6 \text{ m}^{-1}$ , in terms of density fluctuations and the convection velocity of density disturbances. Experimental shock tunnel data are collected using a multi-foci Focused Laser Differential Interferometer (FLDI) to probe the boundary layer at several heights. In addition, a high-fidelity, time-resolved Large-Eddy Simulation (LES) of the conical flowfield under the experimentally observed free stream conditions is conducted. The experimentally measured convection velocity of density disturbances is found to follow literature data of pressure disturbances. The spectral distributions evidence the presence of regions with well-defined power laws that are present in pressure spectra. A framework to combine numerical and experimental observations without requiring complex FLDI post-processing strategies is explored using a computational FLDI (cFLDI) on the numerical solution for direct comparisons. Frequency bounds of  $160 \text{ kHz} < f < 1 \text{ MHz}$  are evaluated in consideration of the constraining conditions of both experimental and numerical data. Within these limits, the direct comparisons yield good agreement. Furthermore, it is verified that in the present case, the cFLDI algorithm may be replaced with a simple line integral on the numerical solution.

**Keywords:** hypersonic turbulence; hypersonic boundary layer; double-foci FLDI; LES; high-enthalpy shock tunnel



**Citation:** Camillo, G.P.; Wagner, A.; Toki, T.; Scalo, C. Combined Experimental and Numerical Investigation of a Hypersonic Turbulent Boundary Layer by Means of FLDI and Large-Eddy Simulations. *Aerospace* **2023**, *10*, 570. <https://doi.org/10.3390/aerospace10060570>

Academic Editor: Kung-Ming Chung

Received: 20 May 2023

Revised: 17 June 2023

Accepted: 19 June 2023

Published: 20 June 2023



**Copyright:** © 2023 by the authors. Licensee MDPI, Basel, Switzerland. This article is an open access article distributed under the terms and conditions of the Creative Commons Attribution (CC BY) license (<https://creativecommons.org/licenses/by/4.0/>).

## 1. Introduction

In the design of aerospace vehicles, the state of the boundary layer is of great importance. Turbulent boundary layers can increase the heat transfer into the vehicle by an order of magnitude compared to the laminar state, demanding an increasing mass budget dedicated to the heat management to ensure the integrity of the vehicle. The increasing skin friction degrades the vehicle performance due to higher viscous drag. Additionally, the pressure fluctuations in the high-speed turbulent boundary layer can cause vibration loads on the vehicle's structure. Despite these negative effects, the occurrence of turbulence is, in many cases, inevitable or even desired, e.g., in applications involving mixing flows, as found in scramjets [1].

However, hypersonic turbulence is still not fully understood and turbulence modeling still results in large uncertainties [2]. Furthermore, experimental data on hypersonic boundary layers, particularly above cold walls, are very limited, hampering the development and verification of new turbulence models. However, insights into pressure and density fluctuations through the boundary layer are important for the closure of Reynolds stresses in the transport equations [3–5], which are necessary for Reynolds-Averaged Navier–Stokes (RANS) turbulence modeling. Without experimental data, the validity of the established low-speed RANS models applied to hypersonic flows remains uncertain [6,7]. In addition, the relevance of the power spectrum of field quantities also extends to Large-Eddy

Simulation (LES) models [8]. Roy et al. [2] underlined the need to compare numerical data based on turbulence models and experimental data, recommending to preferably use non-intrusive measurement techniques to obtain off-wall data. The latter motivates the present study.

Another active field of research is the quantification and identification of free stream disturbances in hypersonic wind tunnels. In [9], it is highlighted that the orientation of the plane-wave disturbances, and thus the type of instability, is important to the boundary layer transition process. Such orientation can be estimated through convection velocity measurements. As noted in [10], the entropy, vorticity, and acoustic modes of disturbance fields are independent. The entropy and vorticity modes convect as frozen patterns along streamlines, while the acoustic modes can cross streamlines and do not convect as a frozen pattern with the local mean velocity. Shock tunnel free stream disturbances have been demonstrated to be mainly acoustic [9–11], and to convect with a Mach-number-dependent ratio with respect to the free stream [4,12]. No general rule for such dependence has yet been proposed, and the compilation of a database to support this is still underway. Duan et al. [4] analyzed pressure signals at different streamwise stations in a Direct Numerical Simulation (DNS) of a turbulent boundary layer at Mach 5.86. The disturbances both in the boundary layer and in the free stream were verified to present little change as they propagated, which could be an indication of frozen waves. In the boundary layer, this was corroborated by propagation speeds similar to the mean velocity. However, they observed that the convection speeds in the free stream were significantly lower than the local mean velocity, contradicting the hypothesis of frozen waves and suggesting the acoustic mode instead.

Towards a better understanding of high-speed turbulence, the comparison between numerical and experimental data is a powerful approach that allows the assessment of hypotheses and complementary analyses. In recent years, a rise in reports on the Direct Numerical Simulation (DNS) of high-speed turbulent flows was observed [4,5,13–25], as well as advancements in theoretical approaches [26,27]. Concerning the experimental aspect, the high velocity and small physical scales of high-speed turbulent boundary layers are a great challenge to measurement techniques. Hot-wire and particle image velocimetry (PIV) have been able to advance the knowledge of the behavior of velocity fluctuations in high-speed turbulent boundary layers [12,28,29]. However, the same cannot be said about pressure disturbances, as highlighted in [4,30]. Pressure measurements are traditionally confined to surface-mounted transducers, making experimental data inside the boundary layer still scarce. Furthermore, the finite area of surface sensors defines a limit to the smallest detectable scales [30,31], and the high frequencies associated with hypersonic turbulent fields are beyond the bandwidths of conventional transducers. In [21], the importance of evaluating the disturbance spectrum up to this upper limit is highlighted in the context of enabling the better use of wind tunnel boundary layer data and their extrapolation to the flight environment.

In recent years, the lack of experimental off-wall and high-bandwidth data has been gradually addressed with the advancements in Focused Laser Differential Interferometry (FLDI). FLDI is a non-intrusive technique capable of measuring flowfield density disturbances along a line-of-sight with an extreme bandwidth and increased sensitivity near the focal plane [32,33]. These characteristics make FLDI a powerful measurement technique for shock tunnel investigations, with many researchers having employed it to probe the free stream [10,11,34–36] and laminar boundary layers [37–43]. Nonetheless, the application of the technique to hypersonic turbulent boundary layers remains largely unexplored.

One of the main challenges pertaining to FLDI resides in the interpretation of its output. The focusing of the beams has an effect on the sensitivity of the instrument with respect to the fluctuation wavenumbers [33,44,45]. While this property is fundamental to allow the FLDI to see through the noisy shear layer surrounding the core flowfield in conventional shock tunnels, the transformation of the line-of-sight-integrated measurements into flowfield quantities is not straightforward. Solutions for specific cases such

as a uniform flowfield and a free jet by means of transfer functions have been presented in [33]. More recently, transfer functions for cases with higher complexity have been developed [46]. In [47], a framework for the interpretation of FLDI measurements is proposed by defining a sensitivity function, which depends on the FLDI setup parameters and an estimate of the average disturbance amplitudes along the optical axis. In [10], the inverse FLDI problem is solved for single-direction, continuous-frequency waves. These recent advancements represent a leap forward in terms of FLDI post-processing. Nonetheless, assumptions about the flowfield are inevitable, due to the inherent loss of information associated with the transformation of a three-dimensional flowfield input into a single scalar FLDI output. In more complex flowfields, this can be an obstacle to fully taking advantage of the FLDI capabilities.

A promising solution to counteract the drawbacks of the instrument is to compare the experimental FLDI data to the equivalent data gathered using computational FLDI (cFLDI; not to be confused with cylindrical-lens FLDI, referred to in the literature with a capital "C" as CFLDI) with spatially well-resolved CFD results. This has been explored with a laminar jet [45] and a complex dynamic flowfield containing shock waves [48]. In these works, computational FLDI was confirmed to be able to extract information from the numerical flowfield directly comparable with experiments. This ability was applied in [49], where cFLDI was used to check the validity of simplifying hypotheses adopted in a post-processing approach for FLDI measurements in circular flowfields. Computational FLDI has also been used to perform parametric studies on the FLDI response to single-frequency disturbances [50]. Furthermore, the ability of FLDI to probe through a noisy surrounding field has been investigated using cFLDI, with the simulation of single-frequency waves [51] and a DNS of a turbulent boundary layer above a wind tunnel model wall [52]. Further applications for this methodology include, for example, verification of the correlations between DNS calculations and a shock tunnel flowfield, or the validation of numerical models of physical phenomena against experimental data.

In the present work, a high-speed turbulent boundary layer over a conical model with cold walls is investigated experimentally and numerically, focusing on the frequency spectra and the convection velocities, by means of multi-foci FLDI readings. Comparisons between experimental FLDI data and a time-resolved LES computation calculated under equivalent flowfield conditions are conducted. The measurements comprise several probing locations in the wall-normal direction, inside the boundary layer and in the near-field above it. The analyses aim at complementing the existing database, while also exploring the framework of direct comparison between the experimental and numerical flowfields in terms of FLDI quantities. Therefore, details are given concerning the experimental and numerical setups, as well as the constraints of the comparisons. Furthermore, evidence is provided that the FLDI instrument is capable of seeing through the shock tunnel nozzle shear layer.

The paper is organized in the following manner. Section 2 details the experimental and numerical setups, including the shock tunnel conditions, measurement techniques, LES solver and cFLDI algorithm. The experimental and numerical results are presented in Section 3 and discussed in further detail in Section 4. Finally, Section 5 summarizes the main findings of the present work.

## 2. Materials and Methods

### 2.1. Experimental Setup

The experimental data in this paper were obtained in the High-Enthalpy Shock Tunnel Göttingen (HEG) of the German Aerospace Center [53]. The HEG is a free-piston-driven shock tunnel capable of generating flowfield conditions equivalent to hypersonic flight in the atmosphere, in terms of pressure and heat flux loads. Test times are in the order of milliseconds, meaning that the walls of the test model remain cold during the test time unless active wall heating is employed.

A total of seven identical shock tunnel runs with free stream Mach number 7.4 and unit Reynolds number  $4.2 \times 10^6 \text{ m}^{-1}$  were conducted. Table 1 details the observed free

stream conditions. The HEG free stream conditions were derived following a calibration procedure detailed in [53].

**Table 1.** Average HEG free stream conditions in this work, with corresponding standard deviations in parentheses. Static conditions were computed with the TAU code and extracted at the center of the nozzle exit plane.

$p_0$ [MPa]	$T_0$ [K]	$h_0$ [MJ/kg]	$M_\infty$ [-]	$Re_m$ [ $\times 10^6 \text{ m}^{-1}$ ]	$p_\infty$ [Pa]	$T_\infty$ [K]	$\rho_\infty$ [g/m <sup>3</sup> ]	$u_\infty$ [m/s]	$T_w/T_r$ [-]
19.0 (1.8%)	2609 (1.0%)	3.14 (1.2%)	7.4 (0.1%)	4.2 (0.8%)	2074 (2.0%)	252.1 (1.3%)	28.6 (0.9%)	2367 (0.5%)	0.11 (1.0%)

In the interest of allowing the flowfield investigated in this work to be fully reproduced, further detail is provided in Appendix A. Spatially resolved properties are given therein, based on a RANS solution of the nozzle flow obtained under the experimental conditions measured in the present investigation. By using the dataset from Appendix A, the spatial distribution of the free stream properties upstream of the conical shock produced by the model can be reproduced within 0.1% error.

The investigated model is a 7° half angle at a 0° angle-of-attack and with a nose tip radius of 0.1 mm. The model is instrumented with a line of 21 Medtherm coaxial type E thermocouples. These sensors are distributed along a streamwise line on the surface of the cone, facing the region probed with the optical techniques to be detailed. Heat flux measurements derived from thermocouple data are used to monitor the state of the boundary layer. Figure 1 shows the measured heat flux levels across all seven shock tunnel runs. It is verified that the independent runs are able to produce flowfields that are consistently similar. The experimental standard deviations at any given location are similar across all runs. For clarity, they are suppressed for all but one run in Figure 1. The rise in the heat flux values from approximately 400 mm to a higher plateau downstream of 600 mm, accompanied by larger standard deviations, indicates the transition of the boundary layer to a turbulent state. Due to the strong similarity between all runs, the measurements obtained across the full shock tunnel campaign are combined to build a comprehensive overview of the turbulent boundary layer, as will be further detailed in this work. The figure also compiles the surface heat flux distribution obtained in the computational flowfield analyzed in this work, together with a previous experimental distribution obtained in HEG [54], which was used as a reference to set up the computations.

Additional instrumentation pertinent to the analyses in this work includes a Z-type high-speed schlieren and a quad-foci Focused Laser Differential Interferometer (FLDI).

The schlieren system uses a Phantom v2012 camera and a Cavilux 640 nm laser source, with the knife edge oriented parallel to the surface of the cone. The images are acquired with a sampling rate of 57 kHz, which provides more than 100 frames within the shock tunnel steady-state time. The visualization area is approximately 40 × 15 mm (streamwise × wall-normal) centered around the FLDI probing location, with a spatial resolution of approximately 24 pixels/mm.

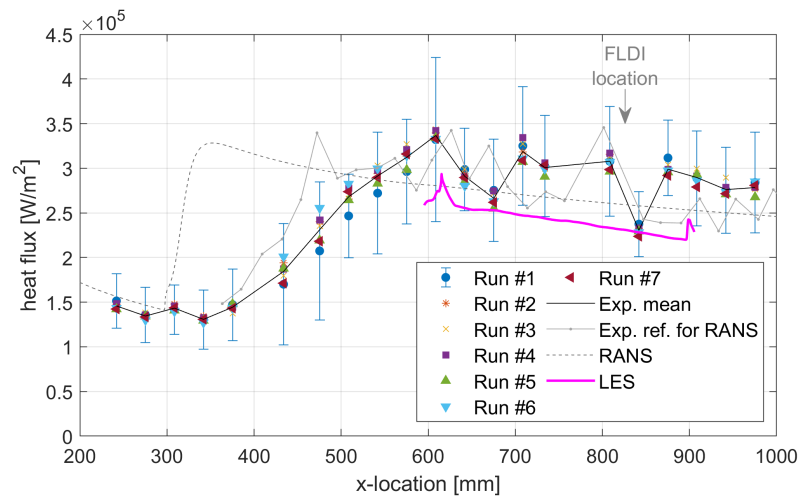


**Figure 1.** Surface heat flux density distributions along the model for all seven shock tunnel runs. For clarity, the experimental standard deviations are suppressed for all but one run, and mean values across all runs are shown with a black solid line. The  $x$  coordinate is measured along the axis of the cone. Additionally shown are the distribution obtained in the LES used in the present work; the laminar and turbulent distributions in the precursor RANS simulation; and a previous experimental distribution obtained in HEG [54], which was used to define the boundary layer trip location in the RANS simulation.

The schlieren images are primarily used to estimate the  $u_{99}$  boundary layer thickness in each run. This is performed by noting that the location of the maximum curvature of the wall-normal density distribution presents some proximity to that of 99% of the velocity magnitude. High-speed conical laminar boundary layers on a cold wall under different HEG free stream conditions have been computed using the TAU code in past works [55,56]. Analyses of these computations have revealed that the locations of maximum curvature in density and 99% of the velocity magnitude are within 5% of each other. It will be seen in the computational results in Section 3 of the present work that this relationship is degraded in the turbulent boundary layer, with a difference of around 14%. This value gives rise to measurement uncertainty, which should not be neglected, and it is therefore taken into account when analyzing the present results. It will be shown in Section 3.1 that the obtained boundary layer thickness estimates are still accurate enough for the purposes of this work.

Schlieren is used to estimate the boundary layer thickness as follows. The schlieren knife edge parallel to the model surface yields illumination proportional to the first derivative of the flowfield density along the wall-normal direction. Hence, the differences in pixel intensity along this same direction are representative of the second derivative of density, and the maximum curvature is a peak in these values. A reference schlieren flow topology image is obtained in each run as the average of all frames within the experimental steady-state time. For every column in the image (wall-normal direction), a vector of pixel intensity differences is obtained. The new image containing the distribution of the wall-normal differences in pixel intensity is then smoothed with a moving average of 200 pixels across the columns (streamwise direction). In this final image, the peak value along each column is marked as an approximation of the local  $u_{99}$  boundary layer thickness. Finally, a linear regression is found using least squares considering all the points obtained across the full schlieren field of view. The boundary layer thickness at the probing location is calculated by evaluating the linear fit.

The estimates of the boundary layer thickness will be used in Sections 3 and 4 to non-dimensionalize the FLDI probing positions in both the experimental and computational cases. Table 2 shows the  $u_{99}$  boundary layer thickness  $\delta$  obtained in each run in this work

using the schlieren method above, together with the relative positions of the FLDI probes, to be detailed next.

**Table 2.** Measured boundary layer thickness  $\delta$  (approximate of  $u_{99}$ ) and relative wall-normal positions of FLDI probes  $y_F$  in each shock tunnel run.

Run #	$\delta$ [mm]	$y_{F,lower}/\delta$	$y_{F,upper}/\delta$
1	5.10	$0.069 \pm 0.015$	$1.821 \pm 0.074$
2	5.37	$0.283 \pm 0.024$	$1.953 \pm 0.051$
3	$5.23^1$	$0.447 \pm 0.033$	$2.141 \pm 0.064$
4	5.21	$0.568 \pm 0.043$	$2.294 \pm 0.091$
5	5.27	$0.839 \pm 0.033$	$2.533 \pm 0.059$
6	5.21	$1.167 \pm 0.041$	$2.885 \pm 0.070$
7	5.18	$1.471 \pm 0.042$	$3.199 \pm 0.078$

<sup>1</sup> There was no schlieren in this specific run; value obtained as the average of all others.

The experimental FLDI setup employed in this work is a quad-foci FLDI, with four independent probes in a  $2 \times 2$  arrangement along the perpendicular streamwise and wall-normal directions. The streamwise pairs are used to obtain convection velocity estimates. The wall-normal splitting allows measurements of velocity and frequency spectra at two distances from the model wall simultaneously in each shock tunnel run.

The main characteristics of the quad-foci FLDI are listed in Table 3, in which  $\lambda$  is the laser wavelength,  $D_{4\sigma}$  is the maximum beam width at the field lenses and  $d$  is the distance between the field lenses and the focus of the system. The separation between the interferometric pairs is denoted by  $\Delta x_1$  and measured by analyzing the response of the system to a weak lens, as described in [33,57]. The separation between the independent FLDI probes in the streamwise direction,  $\Delta x_2$ , is measured using the weak blast wave approach described in [58]. Finally, the separation between independent FLDI probes in the wall-normal direction,  $\Delta y$ , is measured by means of direct imaging using the schlieren camera with a semi-transparent stopper at the focus of the FLDI.

**Table 3.** Quad-foci FLDI setup information.

$\lambda$ [nm]	$D_{4\sigma}$ [mm]	$d$ [m]	$\Delta x_1$ [ $\mu\text{m}$ ]	$\Delta x_2$ [mm]	$\Delta y$ [mm]
532.3	45	1.920	$89.94 \pm 1.14$	$1.937 \pm 0.006$	$\approx 8.9$

In order to allow simultaneous schlieren measurements in every run, the FLDI is used with an angle of  $2^\circ$  with respect to the spanwise direction. This angle is considered when calculating the convection velocities. Nonetheless, the  $2^\circ$  yaw represents a maximum streamwise difference of only 2.3 mm between the right and left edges of the intersection between the FLDI axis and boundary layer under the conditions investigated in this work. Therefore, the angle will be disregarded in the interpretation of the frequency spectra in Section 4.

The splitting and recombination of beams for interferometry is obtained using a pair of Sanderson prisms [59], which is calibrated using the lens approach detailed in [33,57]. The Sanderson prism is oriented such as to split the interferometric pair in the streamwise direction. The selected interferometry distance  $\Delta x_1$  seen in Table 3 is chosen so as to maximize the frequency bandwidth of the instrument, while still presenting a sufficient signal-to-noise ratio, based on previous HEG tests under similar conditions. The Nyquist frequency of the FLDI in the flowfield conditions investigated in this work is estimated as approximately 10 MHz.

The FLDI laser source is an Oxixus LCX-532S DPSS. The beam intensity is detected using a Thorlabs DET36A2 photodetector of nominal bandwidth 25 MHz. The photodetectors are connected with  $50 \Omega$  termination to an SRS SR445A DC-350 MHz preamplifier with  $25\times$  amplification. The resulting signals are recorded on an AMOtronics transient recorder

with DC coupling and a 100 MHz sampling rate. Conversion of the recorded voltage into the FLDI phase difference is performed following [60]. Prior to each shock tunnel run, the FLDI is adjusted to half the maximum output value, for optimal sensitivity.

The duplication of the FLDI probe in the streamwise direction is achieved using a  $2^\circ$  Wollaston prism, as detailed in [58]. In the wall-normal direction, a second pair is obtained using the combination of a non-polarizing beamsplitter cube and a convergent lens of focal distance 400 mm near the laser source, as shown in Figure 2. A half-waveplate is used before the streamwise splitting to adjust the beams to similar power levels, such that all instruments present similar signal-to-noise ratios. The optical setup is such that the two FLDI probes that are closer to the model wall are slightly more powerful than the other two, but the powers of each streamwise pair of probes are identical.

The attention given in [58] to the production of parallel FLDI probes aiming at reliable convection velocity correlations is retained here. Therefore, the additions illustrated in Figure 2 are conceived such that all beams cross the center axis of the instrument at the focal distance of the field lens, where the Sanderson prism is located.

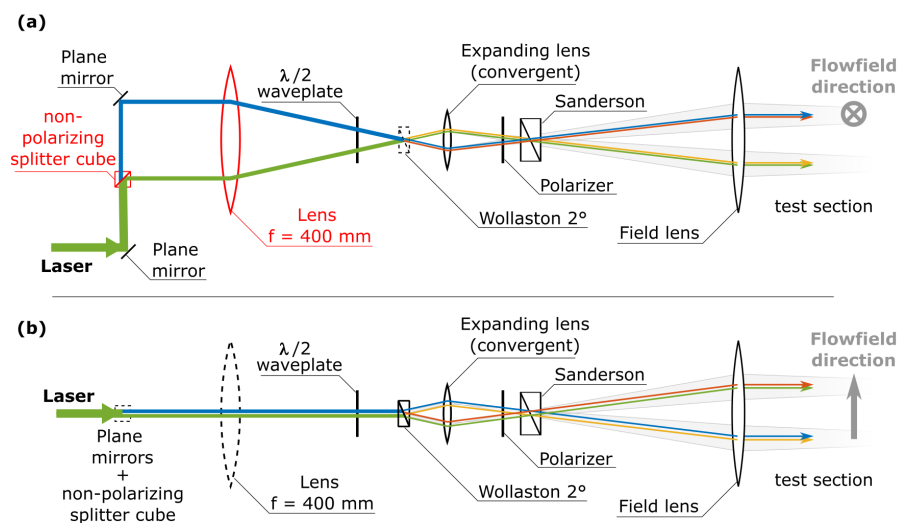


**Figure 2.** Emitting side schematic of quad-foci FLDI with parallel beams in the probing region. Optical components responsible for the wall-normal system duplication are highlighted in red. Beam colors denote the center lines of independent FLDI probes (beam splitting for interferometry at the Sanderson prism not shown, for clarity). Parallel lines represented in close proximity to one another are overlapped in reality. Optical components that do not affect the beam paths in each view are represented using dashed lines. (a) Side view. (b) Top view.

In all shock tunnel runs, the FLDI setup is positioned 825 mm downstream of the cone tip, measured along its axis. As highlighted in Figure 1, this location is approximately 200 mm downstream of the boundary layer transition region. This distance is chosen such that a turbulent boundary layer with well-developed features is probed.

In the wall-normal direction, the FLDI position is varied between runs, to compose a broad picture of the spectra and convection velocity distributions. The locations are listed in Table 2, comprising 5 stations fully inside the boundary layer, 4 stations between one and two times the boundary layer thickness and another 5 above this. Measurement of the wall-normal locations is performed by imaging a semi-transparent stopper at the focus of the FLDI with the schlieren camera, using additional lenses for improved resolution and a calibration target to provide a dimensional reference. The associated level of uncertainty (see Table 2), while not negligible, is considered tolerable when using the measured quantities as approximate wall-normal probing locations.

Frequency spectra from the FLDI measurements are calculated using Welch's method with segments of  $2^{14}$  points and 50% overlap, on a 2 ms time window during steady state. The velocity estimates are obtained through cross-correlation between the streamwise-separated pairs of FLDI probes, using the same 2 ms time window, but divided into 20 segments of 0.1 ms each with no overlap. This is done so that small fluctuations within the steady state are detectable, and the experimental uncertainty may be calculated.

## 2.2. Computational Tools

### 2.2.1. LES Solver

In the LES, Favre-filtered Navier–Stokes equations are solved via a six-order compact finite difference code originally developed by [61] and now under continued development at Purdue. The Quasi-Spectral Viscosity (QSV) approach [62] is used for turbulence closure. The time integration is carried out via a four-stage third-order strong stability preserving (SSP) Runge–Kutta scheme [63]. To ensure stability, the conservative variables are filtered using the sixth-order compact filter described by [64], with a filter coefficient of 0.495.

Only the turbulent region under the shock is simulated in the present LES. The computational domain, illustrated in Figure 3, extends from  $596 \leq x \leq 903$  mm, with  $x$  measured along the cone wall. The azimuthal extent of the domain is 18 degrees. The domain height is 29 mm at the inlet and 44 mm at the outlet. The number of grid points is  $N_x \times N_y \times N_{\theta_1} = 1280 \times 128 \times 112$ . Mean profiles at the inlet are given by a RANS simulation with the Spalart–Allmaras (SA) model [65]. The transition location for the RANS calculation is chosen by matching the experimentally observed beginning of the transition process. The heat flux profile of the RANS calculation shown in Figure 1 is different from experimental data around  $x = 400$  mm because the SA model does not reproduce the intermittency of the transition process. However, the magnitudes agree well with the experiment in the turbulent region. At the wall, an isothermal and a no-slip boundary condition are imposed with a wall temperature of 300 K. The flow properties at the upper boundary are analytically derived via the Taylor–Maccoll inviscid solution [66]. To generate realistic inflow turbulence, turbulent fluctuations are extracted at  $x = 834$  mm and imposed at the inflow by a rescaling method [67]. The recovery length, investigated in [68], has been found to be sufficiently short so as not to affect the region where cFLDI is carried out. At the outlet, a homogeneous Neumann condition is imposed for all flow quantities. In addition, sponge layers are used at the inlet, outlet and upper boundaries. The lengths of the sponge layers at the inlet and outlet are 3% of the total computational domain extent in the streamwise direction. At the upper boundary, it is 5% of the wall-normal extent.

### 2.2.2. Computational FLDI

The direct comparisons between experimental and numerical results in Section 4 will be performed using the FLDI output of phase difference,  $\Delta\Phi$ . The means to obtain this quantity on the LES is through computational FLDI (cFLDI). This algorithm is based on the ray-tracing model presented in [44], with further improvements detailed in [48]. A detailed description of the cFLDI algorithm used in the present work is presented in [49]. That work also validates the implemented cFLDI, using measurements on the flowfield generated by a weak blast wave. A summarized overview is presented next, for clarity.

The cFLDI algorithm simulates the behavior of light rays crossing a transparent volume containing density gradients. Variations in local density  $\rho$  cause changes in the refraction index of the medium, which is perceived by the light rays as a change in the optical path. When two monochromatic and coherent light rays travel different optical paths, a phase difference  $\Delta\phi$  between them is produced [69]. This is the phenomenon by which FLDI extracts information from a given flowfield.

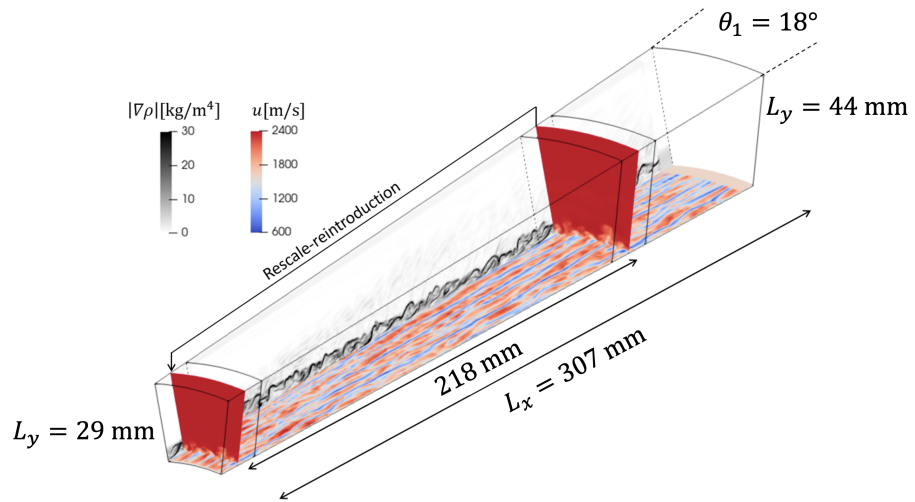


**Figure 3.** Schematic of the present QSV-LES of a hypersonic boundary layer over a cone with rescaling. Streamwise velocity contours are shown in wall-parallel direction and cross-flow planes show streamwise velocity fields; magnitude of the flow density gradient is shown in a side plane.

In the cFLDI, the two orthogonally polarized beams that compose one FLDI instrument are discretized into a finite number of rays. Each ray in one beam has a corresponding pair in the other. After crossing the full probing volume, every pair of rays will present a phase difference between them, caused by the slightly different density fields. This phase difference is

$$\Delta\phi = \frac{2\pi K}{\lambda_0} \left( \int_{C_1} \rho(s_1) ds_1 - \int_{C_2} \rho(s_2) ds_2 \right), \quad (1)$$

where  $\lambda_0$  is the laser light wavelength,  $K$  is the Gladstone–Dale constant ( $K = 0.227 \times 10^{-3} \text{ m}^3/\text{kg}$  for  $\lambda_0 = 532 \text{ nm}$ ) and  $C_i$  are the spatial paths traveled by the beams, parametrically described by  $s_i$ .

When the light rays are recombined on the receiving side of the FLDI, the phase difference between them modulates the light intensity. The FLDI instrument is always configured such that the resulting intensity is a mean value plus a fluctuating component, which is modulated by  $\sin(\Delta\phi)$ , for maximum sensitivity. Finally, the light intensity detected by the FLDI instrument is a scalar value corresponding to the combination of all light rays, weighted by the beam intensity distribution across its area. The FLDI in this work uses circular beams with an approximately Gaussian intensity distribution. Therefore, rays are described using radial  $r$  and angular  $\theta$  coordinates, and the beam intensity profile is given by  $\tilde{I}_0(\tilde{r}) = 2\pi^{-1} \exp(-2\tilde{r}^2)$ . The *tilde* denotes normalized variables, such that the integral of  $\tilde{I}_0$  over the full area of the beam is unity. The radial coordinate follows the normalization by the local  $1/e^2$  beam radius suggested in [44], with  $\tilde{r} = 2$  containing 99.99% of the beam energy.

The equivalent phase shift  $\Delta\Phi$  corresponding to the integrated light intensity detected by the FLDI is hence given by

$$\Delta\Phi = \sin^{-1} \left( \iint_D \tilde{I}_0(\tilde{r}, \theta) \sin(\Delta\phi(\tilde{r}, \theta)) d\tilde{r} d\theta \right), \quad (2)$$

with  $\Delta\phi(\tilde{r}, \theta)$  given by Equation (1).

Equation (2) provides a scalar value that is directly comparable to the experimental output of the FLDI instrument, minimally post-processed to convert the voltage into a phase difference.

In the ray-tracing approach described above, the mesh used in the cFLDI presents a particular shape as the number of nodes is fixed in the cross-section of the beam, and the area across which they are distributed assumes a minimum value at the focus of the system. As such, it becomes necessary to interpolate the numerical flowfield density values on the cFLDI nodes. Linear interpolation is performed in the LES rectangular coordinates to allow the use of fast algorithms. The LES system is defined such that the  $y$  planes run parallel to the cone wall, with the  $z$ -coordinate being the azimuthal angle,  $\theta_1$  (not to be confused with the FLDI angular coordinate,  $\theta$ ). In this reference system, FLDI draws a curved path, as shown in Figure 4.

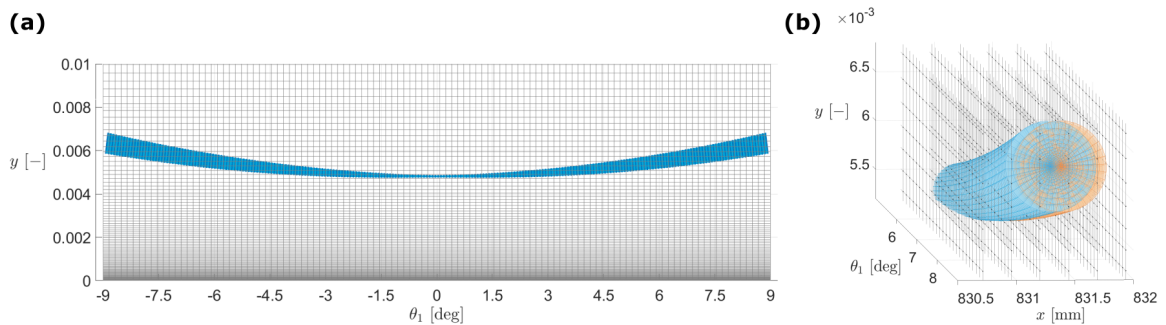


**Figure 4.** Illustration of the computational meshes, in LES rectangular coordinates. (a) Front view, FLDI: blue dots, LES: gray lines. (b) Isometric view in the vicinity of the edge of the LES domain, FLDI: blue and orange lines, LES: gray lines and dots.

A mesh dependence analysis is performed before using cFLDI for comparisons between the numerical and experimental flowfields. The analysis is performed in a concise way, by selecting a probing height and a subset of the simulated time domain that are representative of the worst-case scenario. The strongest density fluctuations are observed in the upper portion of the boundary layer, between 3 and 6 mm from the model wall. Without loss of generality, the height of 4 mm and the time span of  $0.8 \leq t \leq 0.9$  ms are chosen.

The cFLDI is discretized into uniformly distributed planes along its optical axis  $z$ . For the cross-section coordinates  $(\bar{r}, \theta)$ , the angular step  $\Delta\theta$  is defined by the number of equally distributed points along the circumference  $n_\theta$ . The approach suggested in [44] is adopted, by which  $\Delta\bar{r}$  is calculated as a function of  $\Delta\theta$  such that each mesh cell conserves an aspect ratio close to unity.

Looking first at the discretization along the optical axis of the cFLDI, the LES mesh presents a  $\Delta z_{LES} = 286 \mu\text{m}$  at the Cartesian center plane. Comparison of the cFLDI simulations using  $\Delta z_{cFLDI} = 2 \cdot \Delta z_{LES}$  down to  $\Delta z_{cFLDI} = \Delta z_{LES}/4$  has shown negligible variation. Conservatively, a  $\Delta z_{cFLDI} = \Delta z_{LES}/2$  is kept, to ensure that any fluctuations resolved by the LES will be adequately interpolated in the cFLDI.

For the cross-section coordinates, several values for  $n_\theta$  were evaluated. Figure 5 shows the obtained results. The cFLDI values are given in terms of density derivatives, which are obtained in a simple fashion using the known integration length provided by the LES domain to convert FLDI  $\Delta\Phi$  into a  $\Delta\rho$  estimate. This is done so that a broad comparison may be drawn between the cFLDI output and a similar quantity that may be easily extracted from the LES, namely the  $d\rho/dx$  integrated along a  $z_{LES}$  line of constant  $y_{LES}$ . This represents a straight horizontal line in Figure 4a, at the same height as the focus of the FLDI. Figure 5 shows that this simplified quantity and the cFLDI output are not the same, but have similarities. This will be further explored in Section 3.

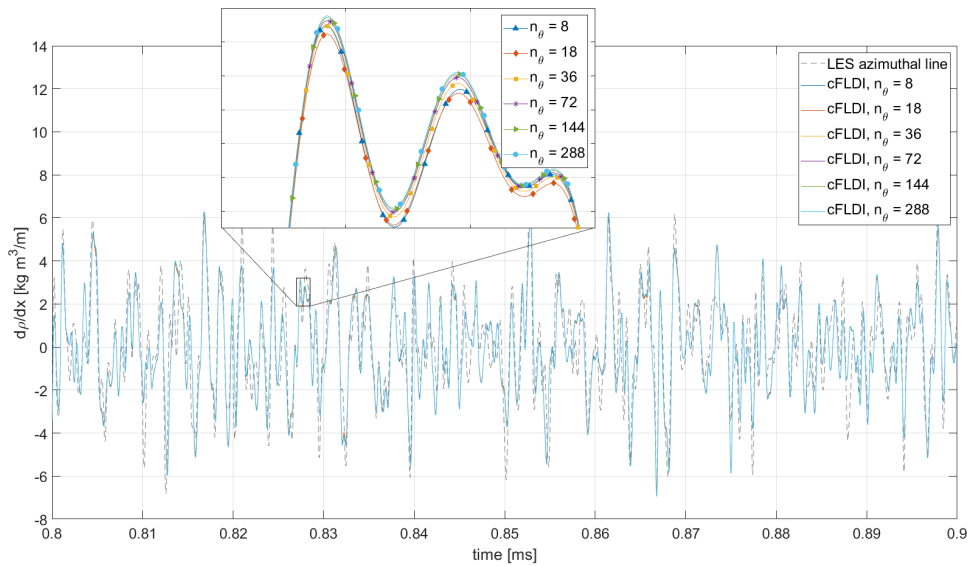


**Figure 5.** Overview of the convergence analysis. The large plot shows the evaluated cFLDI cases, and the results from a simple line integral along the LES azimuthal direction. The detail shows the observed differences between the different cFLDI meshes.

Figure 5 shows that all the evaluated values of  $n_\theta$  produce similar outputs. This is not surprising, given that the cFLDI mesh is naturally significantly finer than the LES one, particularly in the streamwise direction. Nonetheless, small differences can be seen in the detail. Using the finest evaluated mesh ( $n_\theta = 288$ ) as a reference, a zero-lag cross-correlation between its results and those from the remaining meshes is used to select the  $n_\theta$  to be used in the analyses in this work. With  $n_\theta \geq 72$  (four times coarser), a cross-correlation value larger than 0.99 is obtained. It is therefore selected as representing a converged mesh, each beam containing  $89 \times 72 \times 236$  points ( $\bar{r} \times \theta \times z$ ). This mesh is illustrated in Figure 4b, together with the LES points.

### 3. Results

#### 3.1. Experimental Data

The frequency spectra measured with FLDI in the experiments are compiled in Figure 6. The two gray lines correspond to the FLDI response shortly before flow arrival, as a reference of the noise floor of each streamwise pair of probes. The noise floor levels are slightly different due to the small power difference between the wall-normal pairs mentioned in Section 2.1. Flowfield measurements obtained across all shock tunnel runs are shown with different colors.

Two well-defined groups of spectra are seen in the figure. First, measurements obtained above approximately two times the boundary layer thickness present little variation, collapsing together. This reiterates the repeatability of the multiple-run experiments and indicates an upper limit for the turbulent boundary layer influence. These results are in agreement with the hot-wire measurements of supersonic turbulent boundary layers in [12], where it is observed that fluctuations in the free stream do not become constant up to two boundary layer thicknesses away from the wall. Moreover, in the DNS investigation of a Mach 14 turbulent boundary layer in [18], the spectral distribution of pressure disturbances is very similar, between 1.57 and 3.63 times the boundary layer thickness. Additionally, in the cFLDI investigation of a Mach 5.86 turbulent boundary layer DNS in [52], the RMS of the phase difference is observed to be constant only above 1.56 times the boundary layer thickness.

The second group of spectra in Figure 6 concerns measurements fully inside the boundary layer. They present uniformly higher levels than the free stream, with the probe closest to the model wall ( $y/\delta_{u99} = 0.069$ ) detecting marginally smaller amplitudes than the others. Although the coarse distribution of the measurement locations does not allow a precise observation, the region of maximum fluctuation in energy seems consistent with the 75% of the boundary layer thickness verified in the hot-wire measurements of the Mach 7.2 turbulent boundary layer in [28].

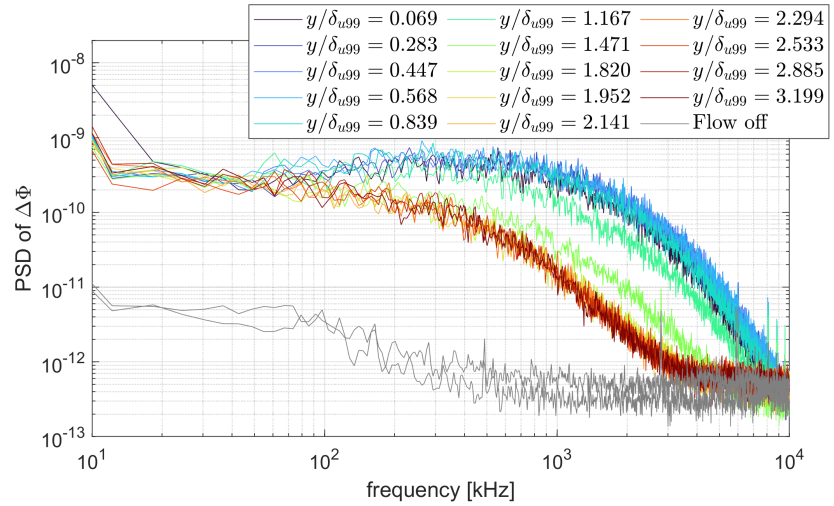


**Figure 6.** Experimentally measured spectra of FLDI output  $\Delta\Phi$ . Data along a common wall-normal axis starting at the wall, with positions normalized by the thickness of the boundary layer measured in each respective run. The gray lines are flow-off references, obtained from the FLDI response before flow arrival.

Below 100 kHz, all measurements register similar amplitudes. However, this is not to be interpreted as a flowfield characteristic. In this frequency range, the corresponding wavelengths are comparable to the maximum FLDI beam width in the test section, for the setup used in this work. Therefore, it is possible that contributions from the noisy shear layer surrounding the core flow are the cause of the overlap. This is to be further discussed in Section 4. Conversely, the higher end of the spectrum shows that the FLDI is capable of detecting disturbances with magnitudes above the noise floor, up to nearly 10 MHz. This is both a testament to the capability of the technique and an indication of the scales of energy-carrying density disturbances. At approximately 2 km/s, 10 MHz corresponds to a disturbance wavelength of 200  $\mu\text{m}$ .

In the simplified case of neglecting the FLDI wavenumber-dependent sensitivity, the straightforward conversion of the FLDI phase differences into arbitrary units of density is possible. In this simplification, the phase differences  $\Delta\Phi$  are proportional to the density differences  $\Delta\rho$  (or, in the limit, its derivative  $d\rho$ ). Therefore, the spectra of phase differences  $S_{\Delta\Phi}(\omega)$  and density  $S_\rho(\omega)$  are related as  $S_{\Delta\Phi}(\omega) \propto \omega^2 S_\rho(\omega)$  [70]. Caveats of this approach will be presented with the discussion in the next section. The results of this simplified conversion using  $\omega^2$  deconvolution are presented in Figure 7, together with lines representing reference power slopes. The density power spectra from Figure 7a are repeated in Figure 7b with the compensation of  $-11/3$  power to facilitate the visualization of the slopes. In Figure 7b, the rise in the free stream spectra starting at 3 MHz corresponds to the effect of the power compensation on the noise floor and should be ignored.

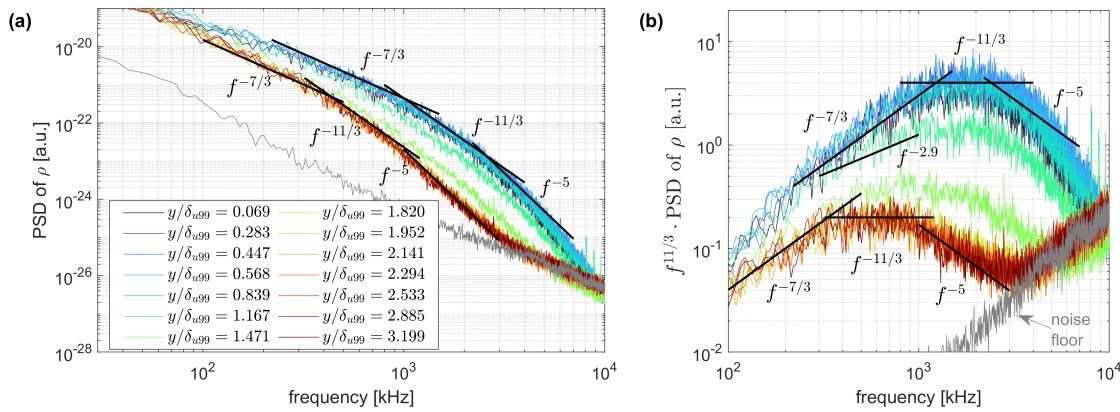


**Figure 7.** Spectra of density, calculated using  $\omega^2$  deconvolution from experimental FLDI measurements. Data along a common wall-normal axis starting at the wall, with positions normalized by the thickness of the boundary layer measured in each respective run. (a) Spectra. (b) Spectra compensated for  $f^{-11/3}$  slope.

The convection velocity measurements obtained from the cross-correlation of signals from the FLDI streamwise pairs are shown in Figure 8. Prior to cross-correlation, the FLDI signals are high-pass-filtered as shown in the legend. This will be further discussed in Section 4.1. Estimated uncertainties of the probing location are represented with vertical bars. They take into account both uncertainties pertaining to the measurement of the location of the FLDI probes with respect to the model wall and the uncertainty of the experimental measurement of the boundary layer thickness. The former are shown in Table 2, while the latter was estimated upon inspection of the LES results to be shown in Section 3.2. The resulting probing location uncertainties are within reasonable bounds to allow the verification of the overall behavior of the convection velocities across the boundary layer. The horizontal uncertainty bars represent the standard deviation of the 20 independent calculations on experimental data using 0.1 ms time windows, as mentioned in Section 2.1. The measurements are verified to generally present little fluctuation within steady-state time, at less than 1% inside the boundary layer and around 1.5% in the free stream. The exception is the point at approximately 1.5 times the measured boundary layer height, which presents a 5% fluctuation. This is attributed to the intermittent passage of turbulent spots at this height, which could be observed in the schlieren images (not shown here).

The convection velocities are verified to be larger than the mean velocity close to the wall and smaller everywhere else. This is in agreement with the convection velocities in a Mach 7.2 turbulent boundary layer presented in [28], in which the limiting height for this inversion was measured to be approximately 15% of the boundary layer thickness. Moreover, in [28], the maximum convection velocities were approximately  $0.9 \cdot u_\infty$ , similar to the results presented here, although, near the wall, the measured values were as low as  $0.6 \cdot u_\infty$ . This discrepancy may be caused by the combination of two factors. First, the wall-to-recovery temperature ratio influences the convection velocity magnitudes near the wall, as seen in the velocity distributions from [4,19] plotted in Figure 8. In [28], this ratio is approximately 0.5. Second, it is possible that the integrating characteristic of the FLDI, to be further explored in Section 4, may bias the results very close to the model wall.

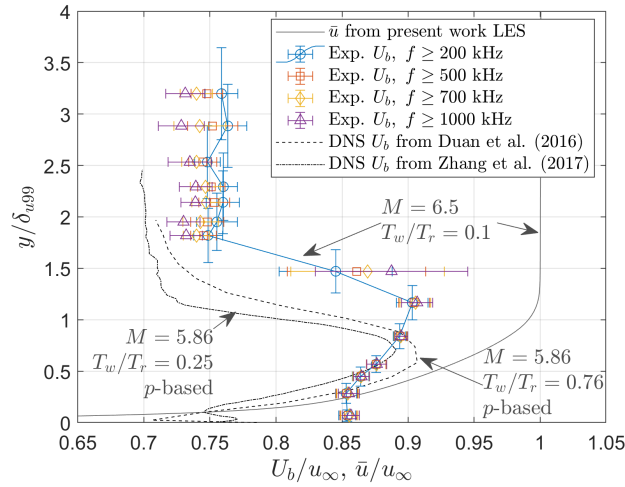


**Figure 8.** Measured convection velocities  $U_b$  across the hypersonic turbulent boundary layer. Measurement locations are indicated as distances to the model wall, normalized with the boundary layer thickness in each run. Uncertainty bars of measurement locations combine the uncertainties of position and boundary layer thickness measurements, shown for a single dataset for clarity. Velocities are normalized with the nominal flowfield velocity at the edge of the conical boundary layer. The mean velocity profile  $\bar{u}$  from the LES in the present work is shown as a reference. Experimental  $U_b$  measurements based on density disturbances, high-pass-filtered over given frequencies. DNS data from [4,19] based on pressure disturbances on a flat plate with lower free stream Mach number are plotted for comparison.

The velocity results shown in Figure 8 allow an estimation of the convection velocity of the density fluctuations in the free stream above the conical boundary layer. The average of these measurements in the case of the lowest high-pass frequency (200 kHz) is plotted in Figure 9 against the bulk velocity of pressure fluctuations available in the literature. In the figure,  $M_r = (u_\infty - U_b)/a_\infty$ , with  $a_\infty$  denoting the speed of sound in free stream conditions. The region below the line where  $M_r = 1$  pertains to disturbances convecting supersonically with respect to the free stream. The convection velocity measured in the present work, which falls within such a region, together with previous investigations, offers further evidence of the dominance of ‘Mach-wave-type’ acoustic radiation in the supersonic free stream [4,9,12,71].

### 3.2. LES Data

The time-resolved numerical solution was simulated for a total flowfield time of 1.43 ms. In the conditions studied in this work, the rescaling–recycling flowthrough time is approximately 0.1 ms. The mean boundary layer profiles are observed to undergo significant changes during the first cycles of rescaling–recycling. The steady-state time of the turbulent boundary layer is assessed by analyzing the wall shear stress over time, shown in Figure 10. A smoothed signal is shown on top of the raw data, to facilitate qualitative observations. The low-frequency, high-amplitude variations until approximately 0.4 ms are evidence of the settling process. Conservatively, the time range below  $t = 0.43$  ms, marked with a dashed vertical line in the figure, is considered to be a transient settling time and is therefore discarded from the present study. The remaining simulated time, which comprises a total of 1 ms within  $0.43 < t \leq 1.43$  ms, is detailed and analyzed next.

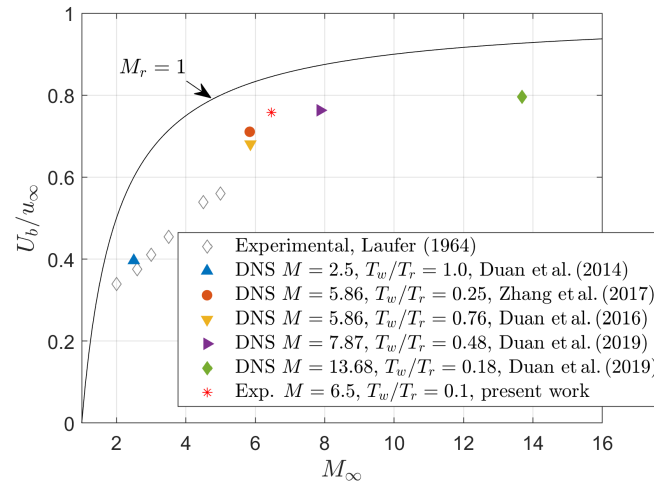


**Figure 9.** Comparison of free stream convection velocities for a wide range of Mach numbers. Literature data refer to convection velocity of pressure disturbances, from experiments [12] and DNS [4,9,19,21].

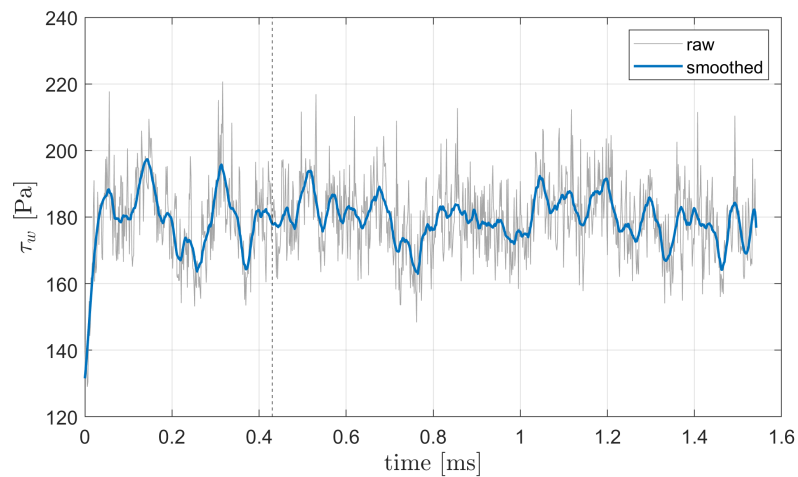


**Figure 10.** LES wall shear stress over time. Raw and smoothed data are shown. The vertical dashed line at  $t = 0.43$  ms marks the beginning of the time range considered for analysis in the present study.

An illustration of the computational flowfield is shown in Figure 11, with a slice of time-varying density contours as they travel across a reference location. The slice has a constant wall-normal distance inside the boundary layer and a fixed streamwise position, with the azimuthal direction represented in the figure’s  $y$ -axis and time along the  $x$ -axis. A subset of the total time is shown, for clarity. This representation illustrates how the flowfield is perceived by an observer at a fixed position, such as the FLDI.

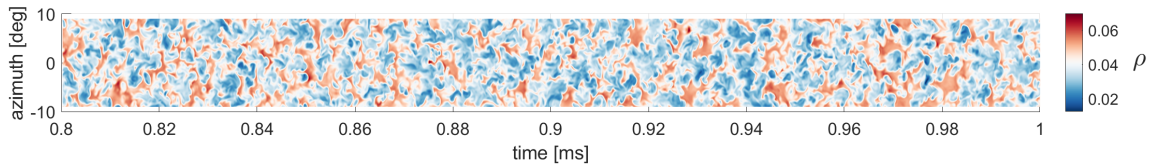


**Figure 11.** LES time-resolved contours of density on a slice of constant wall-normal coordinate  $y = 4$  mm, with the LES azimuthal direction along the  $y$ -axis and time along the  $x$ -axis. A subset of the computational steady-state time is shown.

Figure 12 shows the LES mean distributions of streamwise velocity, density, pressure and temperature, averaged over both time and the azimuthal coordinate. The boundary layer thickness  $\delta_{u99}$  based on 99% of the free stream velocity is annotated, as well as the location where the second difference in density is the maximum. As mentioned in Section 2.1, the latter is the quantity used to estimate the experimental boundary layer thickness from schlieren observations. Figure 12 shows that there is a difference between this and the true  $\delta_{u99}$  of approximately 14%. This mismatch between the two quantities is considered when estimating uncertainties for the experimental measurements shown in Section 3.1.

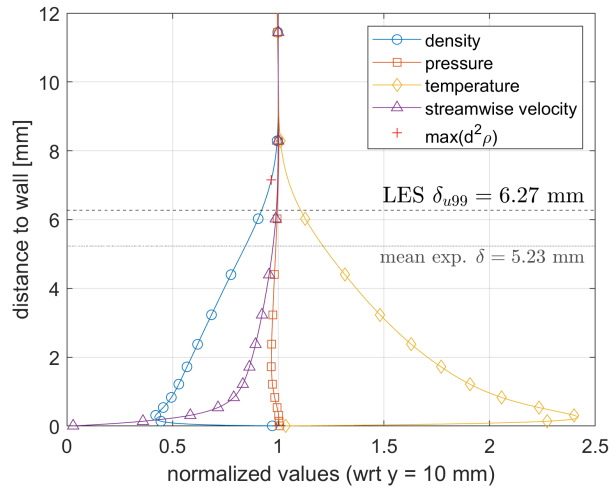


**Figure 12.** Mean boundary layer profiles from LES. Values correspond to azimuthal averages, normalized by their values at  $y = 10$  mm. The boundary layer thickness  $\delta$  corresponding to 99% of the streamwise velocity magnitude is annotated. The location of the maximum second difference in density is highlighted with a “+” sign. The mean value of the experimentally measured boundary layer thicknesses is also represented for reference.

Nonetheless, when comparing the boundary layer thickness in the LES (Figure 12) and experiments (Table 2), a difference of nearly 20% is observed. Despite this difference, the numerical boundary layer is obtained such that turbulence is fully developed and the heat flux magnitude is comparable to the experimental data. Therefore, when comparing experiments and computations in Section 4, the wall-normal coordinate is normalized by the boundary layer thickness in each case.

The frequency spectra of the azimuthally averaged density at the same relative positions as the experimental FLDI probes are compiled in Figure 13. To calculate the spectra, the time-resolved LES flowfield data are first averaged along the azimuthal direction. Then, the time-varying density values at a given distance from the wall are extracted and the spectral estimate is computed. The time-resolved azimuthal average of density represents

the simplest approximation of the FLDI. Differences may be observed between these spectra and the corresponding experimental data in Figure 7. In the low-frequency range up to approximately 100 kHz, the experimental data follow  $-7/3$  power, while the LES data do not, starting to present this slope for larger frequencies only. Furthermore, the LES boundary layer data roll off from the  $-11/3$  power slope shortly above 1 MHz, while the experimental counterparts seem to follow this slope until at least 2.5 MHz. These differences will be analyzed in Section 4.

Since the FLDI outputs a spatial differential measurement, the spectra of the first differences in density  $d\rho$  along the streamwise direction are plotted in Figure 14. This is a more directly comparable quantity to FLDI measurements. The differential density is extracted from the LES flowfield using values from adjacent grid planes in the streamwise direction.

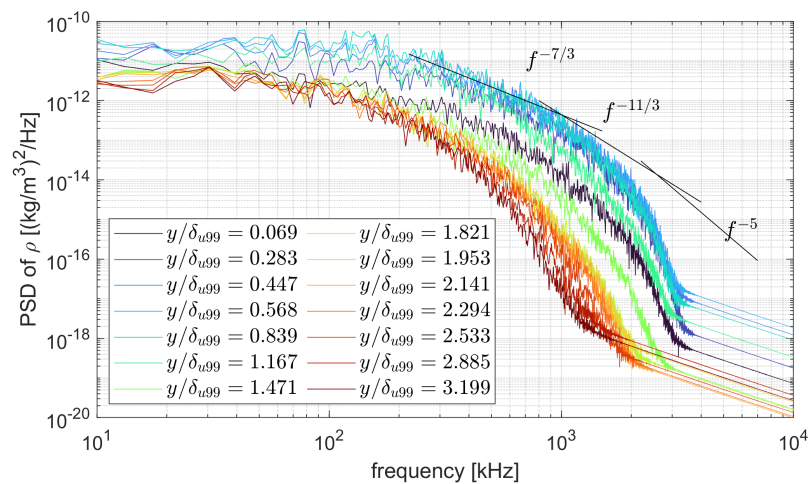


**Figure 13.** Power spectral distribution of azimuthally averaged LES density, at wall-normal locations corresponding to the experimental probes.

Similarities to the experimental results previously shown in Figure 6 can be seen, such as the increased magnitudes when inside the boundary layer and the two distinct groups of spectra. Nonetheless, similarly to the density spectra, differences can be observed in terms of roll-off, especially for frequencies above 1 MHz. This is both an effect of the streamwise resolution of the numerical grid, which limits the wavelength that can be resolved, and the artificial damping necessary to provide stability to the numerical solution. The identification of such constraints is the main goal of Section 4.3.

Convection velocities are calculated on the numerical flowfield for comparison with the experiments. Time-resolved data at the same relative positions as the experiments are extracted and cross-correlated to determine the convection velocities. The flowfield variables are averaged along the LES azimuthal direction, for better comparison with FLDI measurements. Cross-correlation is performed with signals from streamwise planes separated by approximately the same distance  $\Delta x_2$  of the experimental FLDI velocimetry pair. Similar to the experimental case, velocity measurements are obtained in subsets of 0.1 ms and combined into an average value. The results of convection velocities obtained from density and pressure signals are shown in Figure 15. The high-pass filtering used in the experimental case is also repeated here. When filtering above 1 MHz outside the boundary layer, the resulting signal retains little of the simulated flowfield (see the spectral amplitudes in Figure 13). The velocity measurements in such cases are therefore discarded.

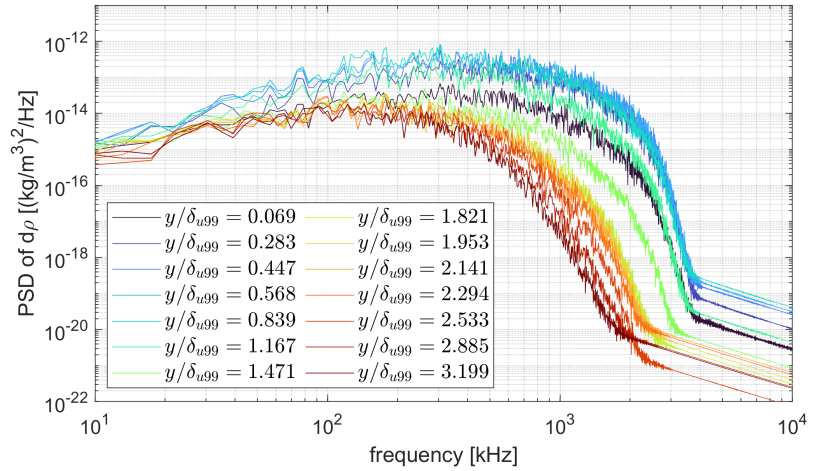


**Figure 14.** Power spectral distribution of the first spatial differences along the streamwise direction of azimuthally averaged LES density, at wall-normal locations corresponding to the experimental probes.

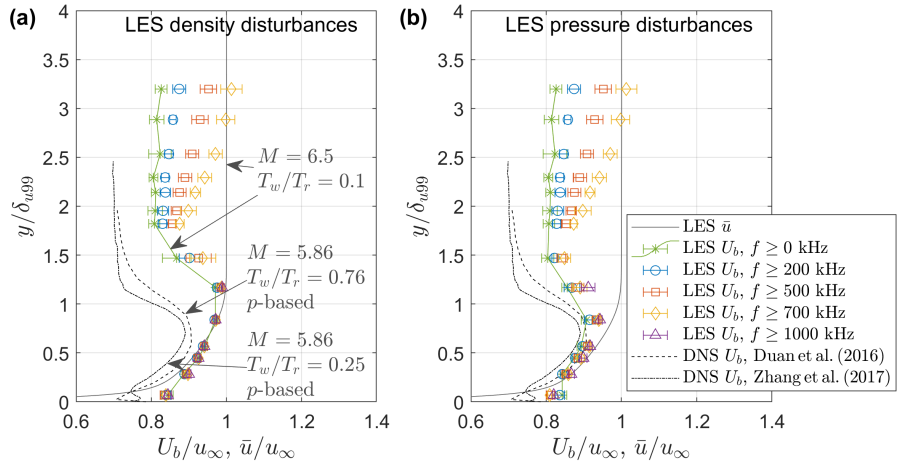


**Figure 15.** Convection velocities across the LES hypersonic turbulent boundary layer, based on (a) density and (b) pressure disturbances. Annotations shown in (a) are also valid for (b). Wall-normal distances along the  $x$ -axis are normalized by the LES boundary layer thickness  $\delta_{i99}$ . Velocities in the  $y$ -axis are normalized with the flowfield velocity at  $\delta_{i99}$ . The mean velocity profile  $\bar{u}$  is shown as a reference. DNS  $U_b$  data from [4,19] based on pressure disturbances on a flat plate with lower free stream Mach number are plotted for comparison.

### 3.3. Computational FLDI

Computational FLDI (cFLDI) was simulated on the LES flowfield, at the normalized positions corresponding to the experimental probes. The spectral distributions of the cFLDI probes are shown in Figure 16.

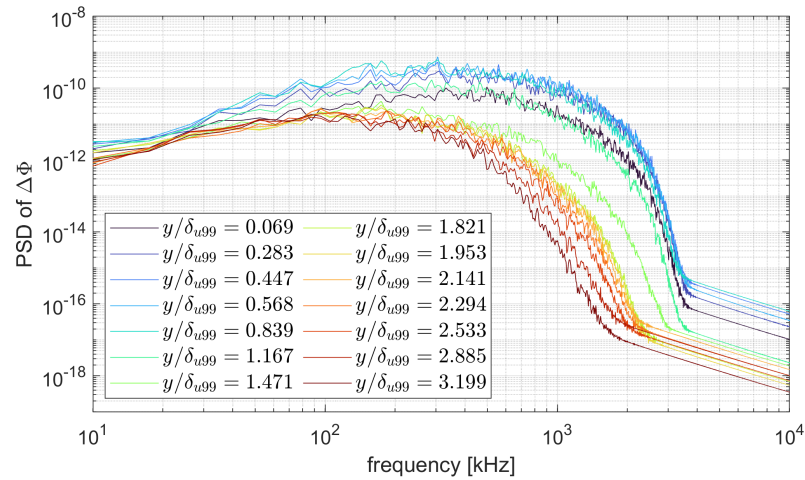


**Figure 16.** Spectra of cFLDI output  $\Delta\Phi$ , at wall-normal locations on the LES flowfield corresponding to the experimental probes.

In this figure, the  $y$ -axis is set to display the same number of decades as Figure 14. Despite the different dimensional units of the time series, namely  $\text{kg}/\text{m}^3$  in Figure 14 and radians in Figure 16, it is possible to notice strong similarities in the spectral distributions. This will be further explored in Section 4.5.

#### 4. Discussion

##### 4.1. Velocity Measurements

Figure 8 shows that the distributions of the convection velocities of density disturbances are overall similar to the DNS results of [4,19], with a larger velocity in the boundary layer and a rather significant drop in the free stream. The maxima and free stream values are also close.

Despite the agreement in shape, however, the experimental results show evident displacement towards the free stream. This may be an effect of the different wall-to-recovery temperatures. There is also a difference in the velocity distribution very close to the wall. In addition to the different wall temperature, the finite FLDI-sensitive length and probing along a secant line through the boundary layer might cause this effect. In order to probe very closely to the wall, the FLDI must cross through the entire boundary layer. In the present setup, the length of the intersection between the FLDI and the boundary layer is approximately 60 mm. As demonstrated in Figure 17, the spatial filter effect of the present FLDI within this distance is small for frequencies as high as 1 MHz. It is therefore subject to accumulated contributions from regions of strong density fluctuation in the vicinity of the focal plane. This is further indicated by the distribution of the convection velocities in the LES results in Figure 15, which do not share this issue and follow the results in [4] more closely near the wall.

The velocity distributions shown in Figure 8 evidence an overall distinction between the convection velocity of the density disturbances and the local mean flowfield velocity. The departure is greater in the free stream than in the boundary layer, but the boundary layer effect is still noticeable, at least up to 1.5 times of its thickness. Furthermore, disturbances of different sizes, which correspond to different frequency bounds in Figure 8, convect with similar velocities in the boundary layer. In the free stream, smaller disturbances (higher frequencies) convect slightly slower than larger ones (lower frequencies). However, the influence of the boundary layer extends further into the free stream for smaller disturbances than for larger ones.

The numerical results in Figure 15 show that the convection velocities based on pressure fluctuations in the boundary layer are comparable with the experimental measurements. This also holds for large disturbances in the free stream for both density and pressure, within a small difference. Conversely, the boundary layer density disturbances in the LES convect at larger velocities than the experimental and LES pressure-based velocities. Additionally, smaller disturbances of both pressure and density in the LES present increasingly larger convection velocities farther away from the model wall, unlike the experimental measurements. These discrepancies require additional analyses of the numerical solution, which are beyond the scope of the present work.

The addition of this work's experimental mean free stream convection velocity to the dataset in Figure 9 allows the verification that the velocity measurements based on density fluctuations yield comparable values to existing pressure-based ones. When considering the extrapolation of the literature points, a slight upward offset of the present measurement can be seen. This agrees with the trend observed in the two similar DNS points of  $M = 5.86$ , in which a colder wall corresponds to a larger eddy convection velocity.

The observed agreement between the convection velocities of pressure and density disturbances is an expected result, since the free stream flowfield can be regarded as isentropic. Nonetheless, contrary to other methods, such as DNS or intrusive experimental devices that measure localized quantities, the FLDI is an integrating instrument. Therefore, the verification that the FLDI measurements are similar to other available data despite this fundamental difference is an important result. It indicates that the existing database of bulk velocity information may be complemented with multi-foci FLDI measurements.

#### 4.2. Spectra of Density Fluctuations

The spectra of density fluctuations shown in Figure 7 allow the observation of the energy cascade of the density disturbances. In an environment dominated by acoustic disturbances, the flowfield is isentropic and thus pressure and density fluctuations are correlated by a constant (square of the sound speed). Therefore, it makes sense to analyze the energy cascade detected by the FLDI in light of the expected behavior of pressure, as a first approximation. The power laws for pressure spectra are represented together with the experimental density data in the figure, for reference.

In [72], power laws are derived for the spectral distribution of pressure fluctuations in a shear flow. Interactions of the turbulence–turbulence type are found therein to follow a  $f^{-7/3}$  decay, while turbulence–mean shear interactions decay as  $f^{-11/3}$  (second moment) and  $f^{-3}$  (third moment). The two latter decays are experimentally observed in the density spectra of a Mach 2 shear layer in [8] and associated with isotropic and anisotropic turbulence, respectively. Nevertheless, in the mentioned work, anisotropic turbulence was observed at low-to-moderate wavenumbers, with power laws measured between 2.9 and 3.2, while isotropic turbulence was found at high wavenumbers. The  $f^{-11/3}$  decay has also been experimentally observed in the Mach 6.1 free stream pressure fluctuation measurements of [73].

The turbulence–turbulence  $f^{-7/3}$  decay is analogous to Kolmogorov's  $-5/3$  power law for velocity [30] and relates to acoustic disturbances (eddy Mach waves). It has been experimentally observed in the farfield of a Mach 4.5 turbulent boundary layer in [12]. More recent DNS studies have also detected the  $f^{-7/3}$  slope at the wall of a transonic turbulent boundary layer with an adverse pressure gradient in [74] and in the Mach 2.5 free stream above a turbulent boundary layer in [9]. It must be noted, however, that this slope was not present in the DNS investigation of a Mach 5.86 turbulent boundary layer in [4]. A scaling value of power  $-5$  is mentioned in [4,74] and attributed to sources in the inner region of the turbulent boundary layer.

It is seen in Figure 7 that the experimental spectra of density fluctuations obtained in the present work follow the power laws to some extent. Both the free stream and the boundary layer have regions described by these scalings, albeit within different frequency ranges. A rather large region following the  $-7/3$  power slope is seen for both the boundary

layer and free stream. This indicates a significant contribution of acoustic disturbances to the turbulent energy. It may be related to the noisy shock tunnel environment [75], which is dominated by acoustic disturbances, but only partially, as it is also present in the LES spectra in Figure 13. Interestingly, the  $-5$  power slope is well defined in measurements at distances more than two times the thickness of the boundary layer. Since this behavior is linked to boundary layer sources, this could be an indication of energy emission into the free stream. However, given that the source of the  $f^{-5}$  slope is found to the sublayer region below  $z^+ = 20$  [4], more intricate phenomena would then be responsible for allowing this to reach the free stream, the investigation of which is beyond the scope of this work.

Although these observations are useful to provide insight into the mechanisms governing the energy cascade in hypersonic flowfields, they must be interpreted with caution. As mentioned in Section 3.1, the spectral distribution of densities was obtained by assuming direct proportionality between the FLDI phase differences and the flowfield density fluctuations. This hypothesis neglects the wavenumber-dependent sensitivity length of the FLDI. The simplification is reasonable for low frequencies up to a certain threshold, as it can be seen in Figure 13 that the density spectra directly calculated from the numerical flowfield also agree with the  $-7/3$  power in an intermediate range of frequencies.

However, in order to correctly convert the high end of the FLDI spectrum, more sophisticated approaches are needed. Furthermore, the threshold to use the simplified approach of merely deconvolving  $\omega^2$  on the FLDI data is not easily defined. The following sections discuss computational FLDI as an alternative solution for direct comparison between experimental and numerical results. Once the comparison is established, it becomes possible to take advantage of the insight given by the numerical investigation without the need to directly address the complexity of the experimental measurement instrument.

#### 4.3. Constraints for Experimental and Numerical Direct Spectral Comparison

For direct comparisons between computational and experimental FLDI results, it is important to consider the limitations pertinent to each environment.

In the experiments, the FLDI instrument must run through a noisy shear layer that surrounds the core flowfield. The wavenumber-dependent sensitivity length of the instrument is well explored in [33]. It is such that high-frequency content is only detected near the center plane, but the lower end of the spectrum is detected along the entire optical axis. Therefore, the shear layer imposes a lower limit on the useful frequency response of the FLDI, below which the measurements are dominated by shear layer content [11,52]. However, the limit is not a well-defined value, as the FLDI response to a disturbance of a given wavenumber rolls off continuously away from the center plane.

A methodology to assess the lower bound of the FLDI bandwidth in the presence of strong disturbances surrounding the flowfield is presented in [76]. The method is based on a ratio of sensitivity functions between the volume of interest and the noisy region, and it uses the transfer functions of the FLDI instrument and assumptions on the average amplitudes of disturbances across the probed volume. This approach has been applied to a test case of free stream measurements through a nozzle shear layer in [11]. In the present work, a simplified approach is chosen, aiming at a plane-by-plane analysis, as will be shown. This is a less conservative approach than the more complex method of [76], but is preferred in this work for two main reasons. First, it does not require explicit assumptions on the spatial distribution of disturbance magnitudes. Second, for the present case, at the same time that the direct contribution of the shear layer to the FLDI signal is constrained to the edges of the flowfield volume, the total width of the shear layers is comparable to the length of the intersection between the FLDI and the turbulent boundary layer. This means that the contribution of a signal either in the shear layer or in the boundary layer will be similar in terms of spatial integration. Nonetheless, the FLDI filtering effect away from the focus will cause the damping of the amplitudes at the location of the shear layer. This damping is evaluated using transfer functions as follows.

The FLDI transfer function is defined as the ratio between the spatial derivative measured by the instrument and a true spatial derivative of the same disturbance field. As explored by many authors [33,44,45,76], a useful reference disturbance field is a single-frequency sinusoidal wave of infinitesimal thickness. The transfer function representing the FLDI spatial filtering in this case is

$$H_w(k) = \exp\left(-\frac{w^2 k^2}{8}\right), \quad (3)$$

where  $w$  is the local FLDI beam radius and  $k$  is the wavenumber of the sinusoidal wave, which relates to frequency  $f$  and convection velocity  $U_b$  as  $k = 2\pi f / U_b$ . The use of this formulation to evaluate the FLDI wavenumber-dependent sensitivity length has been experimentally validated in [45], through analyses of multiple ultrasonic wavefronts of well-defined frequencies.

In the shock tunnel experiments reported here, the core flowfield presents a radius of approximately 250 mm [53]. Equation (3) is therefore used to evaluate the FLDI transfer function magnitudes at this location, denoted for simplicity as  $H_{250}(k)$ , for a wide range of wavenumbers. Corresponding reference magnitudes at the center plane, denoted  $H_0(k)$ , are also evaluated. The comparison between them provides a wavenumber-resolved loss parameter, shown in Figure 17. For a more straightforward interpretation, the figure displays the results plotted against frequencies obtained from wavenumbers using the measured free stream convection velocity of approximately  $0.75 \cdot u_\infty$ , as shown in Figure 8.

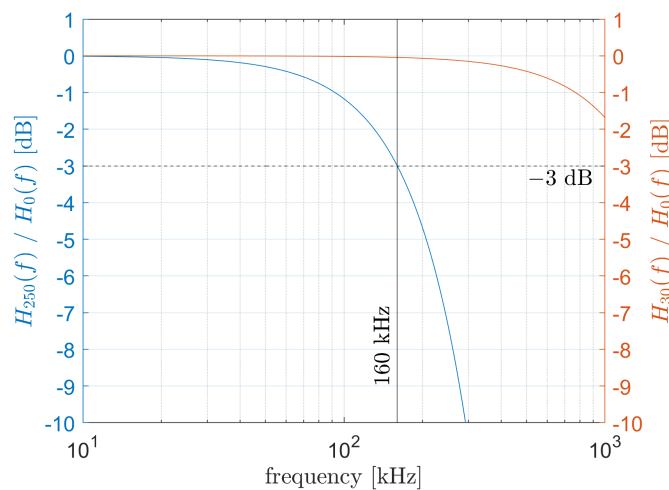


**Figure 17.** Loss of FLDI transfer function due to spatial filtering, evaluated for multiple frequencies at two distances from the center plane: 250 mm (left  $y$ -axis), representative of the nozzle shear layer, and 30 mm (right  $y$ -axis), representative of the edge of the conical boundary layer.

Without losing generality, a loss of  $-3$  dB is defined as a reference bound. This corresponds to a half power decay, before which the signal amplitudes detected in the shear layer are expected to be significant enough to bias the measurements from the core flowfield. Figure 17 shows that at 250 mm from the center plane, the FLDI in the present work presents a  $-3$  dB loss at  $f = 160$  kHz. The experimental spectra below this frequency value are hence discarded. It should be noted that despite the simplifications contained in this approach, this value is in agreement with the experimental spectra shown in Figure 6, which show separate amplitudes between the boundary layer and free stream in the vicinity of this frequency. If the contribution of the shear layer was not sufficiently damped, an

overlap of the spectral amplitudes would be expected, such as in the region below 100 kHz in the figure.

An additional line is plotted in Figure 17 using the right  $y$ -axis for the transfer function magnitudes at a distance of 30 mm from the focal plane, corresponding to the boundary layer intersection mentioned in Section 4.1. It is verified that, in this case, the transfer function value remains close to the best focus reference across all evaluated frequencies, which represents the weak spatial filter effect in this analysis.

Additional limitations must be considered at the opposite end of the spectrum, towards extremely high frequencies. First, the experimental measurement capabilities are limited by the FLDI beam separation distance  $\Delta x_1$ . Wavelengths smaller than twice the separation  $\Delta x_1$  cannot be resolved. In the present case,  $2 \cdot \Delta x_1 \approx 180 \mu\text{m}$ , which corresponds to 10 MHz in the free stream and 12 MHz in the boundary layer, using the velocity information in Figure 8. These are constraints of a spatial nature. The oversampling in the time domain, which, in the present work, is 100 MHz (see Section 2.1), favors the proper detection of amplitudes in addition to frequencies. It is important to highlight that a compromise must be made between  $\Delta x_1$  and the signal-to-noise ratio, since the differences between two points will be smaller as the distance between them is reduced. In this regard, Figure 6 shows that the FLDI in the present work was able to optimize this trade-off.

A second high-frequency constraint relates once more to the wavenumber-dependent sensitivity length of the FLDI. At this edge of the spectrum, it is possible that the same spatial filtering that allows the instrument to see through the shear layer starts damping information within the scope of the investigation. This is especially the case for the free stream spectra in the present work. The conical flowfield contributions to the FLDI signal are expected to be approximately equal throughout the probing volume, or at least within the boundaries of the conical shock (notwithstanding, the circular symmetry of the flowfield surrounding the conical model must be properly considered when probing along a straight-line FLDI, as seen in [49]). With such an extensive probing volume, the influence of the varying sensitive length is expected to cause significant amplitude differences across the frequency spectrum. The resulting FLDI signal accumulates contributions from lower-frequency disturbances across the full probing length, while higher frequencies contribute only along a limited portion of it. Such cases are the main motivation to use the transfer function approaches from [33,46,47]. However, these functions must be obtained while respecting the flowfield characteristics, and the derivation of a transfer function for conical flowfields is beyond the scope of the present work.

Turning to the numerical flowfield, constraints for FLDI comparison concern the resolved frequency bandwidth and the limited spatial domain. The frequency bandwidth is determined by three factors: (1) the temporal resolution of the LES; (2) the spatial resolution of the grid; and (3) the explicit spatial filtering required for the numerical stability of the compact finite difference scheme. In the present case, the temporal resolution of  $0.014 \mu\text{s}$  is enough to provide reliable amplitudes up to at least 7 MHz, assuming a conservative oversampling of 10 times. The grid resolution is  $245 \mu\text{m}$ , yielding a Nyquist limit of approximately 4 MHz, assuming a flowfield velocity of 2 km/s. The sixth-order compact filter dampens high-frequency phenomena starting with a weakened effect above 1 MHz and becoming progressively stronger at higher frequencies, due to its non-sharp spectral behavior. The effect is shown in Figures 13, 14 and 16. Representing the stricter high-frequency constraint in the present dataset, the upper bound of 1 MHz is chosen for the numerical and experimental comparisons in Section 4.4.

Lastly, the limited spatial domain of the LES may impose a constraint for experimental and numerical comparisons that relates yet again to the FLDI spatial filtering. If a numerical flowfield is obtained along the full FLDI probing length, then the spatial filtering of high frequencies is also present in the cFLDI simulation. In this case, direct comparisons between experimental and computational FLDI are valid without the need to correct the amplitudes in any way. If, on the other hand, the simulated flowfield corresponds to a section of the volume that contributes to the FLDI signal, the comparison is still possible, albeit with

further considerations. One option is to correct for the FLDI spatial filtering in some way, as mentioned above. Alternatively, the comparisons must be restricted to frequencies above a certain value, similar to the shear layer analysis presented earlier in this section.

#### 4.4. Direct Comparison between Experimental and Numerical Spectra

The conical boundary layer offers an advantage in the sense of the preceding observations. The amplitudes of the fluctuations inside the boundary layer are much larger than in the free stream. Furthermore, the FLDI crosses the conical boundary layer following a secant line close to its edge. Therefore, the volume largely contributing to the FLDI signal is much reduced. For example, when the FLDI is positioned at a height of  $0.8 \cdot \delta_{i,99}$ , the length of intersection between the FLDI and the boundary layer is approximately 30 mm. This length has initially informed the definition of the size of the LES domain in this work, which presents a large enough azimuthal width to comprise the entirety of the intersection at this height. As a result, in the upper portion of the boundary layer, the full length of the intersection between the FLDI and the conical boundary layer is calculated.

This means that for a subset of the experimental and numerical data presented in Figures 6 and 13, respectively, a direct comparison is allowed with minimum constraints. Figure 18 displays the comparison for three probing stations inside the boundary layer, namely  $y/\delta = 0.447$ ,  $0.568$  and  $0.839$ .

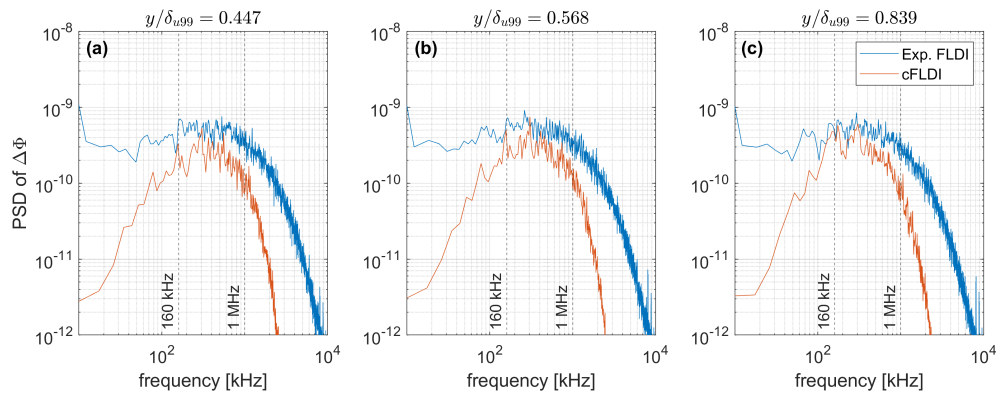


**Figure 18.** Direct comparison between the spectra of phase differences from experimental FLDI and cFLDI calculated on the LES, for three different locations. (a)  $y/\delta = 0.447$ , (b)  $y/\delta = 0.568$  and (c)  $y/\delta = 0.839$ . The lower and upper frequency bounds for the comparison are shown as dashed lines.

These results show encouraging agreement between the experimental and numerical results within an intermediate range of frequencies. This range agrees to a certain extent with that obtained from the analyses in Section 4.3, namely  $160 \text{ kHz} < f < 1 \text{ MHz}$ .

It is important to highlight the low-frequency bound of  $f = 160 \text{ kHz}$  determined in the previous section. Figure 18 confirms that indeed the experimental and numerical lines diverge significantly for frequencies below approximately this value. This is an indication that the lower frequencies in the experimental results have an origin other than the boundary layer. Therefore, it is paramount that a high-pass filter is used when employing FLDI for shock tunnel velocimetry, as exemplified in Figure 8. Otherwise, the signals being cross-correlated will most likely contain spurious low-frequency contributions, which have a strong impact on the cross-correlation operation and may thus bias the results.

Nonetheless, as mentioned before, the FLDI filter effect rolls off continuously, meaning that there is no unique means of finding a cut-off limit. Hence, there is an inevitable level of arbitrariness when choosing how to define a threshold. The  $-3 \text{ dB}$  loss with respect to the response at the focus was chosen in the present work, but alternative metrics have been previously used in the literature, such as  $1/e$  folding in the RMS response [32] or the full-width half maximum (FWHM) of the transfer function [47]. This stresses the importance of

having complementary methods of checking the calculated limit. In the present work, these are the simultaneous measurement of the free stream and boundary layer disturbances and the direct comparison to numerical results.

4.5. On the Simplified Comparison between Experimental FLDI and Numerical Solutions

As mentioned in Section 3, there is apparent similarity between the cFLDI spectra in Figure 16 and the LES  $d\rho$  spectra in Figure 14. This is an indication that the focusing effects of the FLDI are negligible.

An analysis similar to the one in Figure 17 was performed to evaluate the spatial filtering effect within the LES domain. At the edges of the boundary layer intersection previously mentioned, frequencies below 1.1 MHz still retain over 95% of the FLDI center plane sensitivity. In other words, the FLDI spatial filtering effect is very small in the boundary layer within the frequency bandwidth resolved by the LES.

In such cases, fluctuations in density  $\rho$  and FLDI output  $\Delta\Phi$  are correlated in an almost direct manner, as a simplification of Equation (1):

$$\Delta\Phi_{\text{direct}} = \frac{2\pi K}{\lambda_0} L \Delta\rho, \tag{4}$$

where  $\Delta\rho$  is the summation (line integral) of the density fluctuations along a line crossing the LES volume at any given time instant, and  $L$  is the length of this line.

Figure 19 shows the result of evaluating Equation (4) along a line of constant wall-normal coordinates in the LES rectangular system of coordinates, which is equivalent to a horizontal line in Figure 4a. It is denoted ‘cFLDI approximation’ and plotted together with experimental and computational FLDI at the same probing height, measured at the center plane.

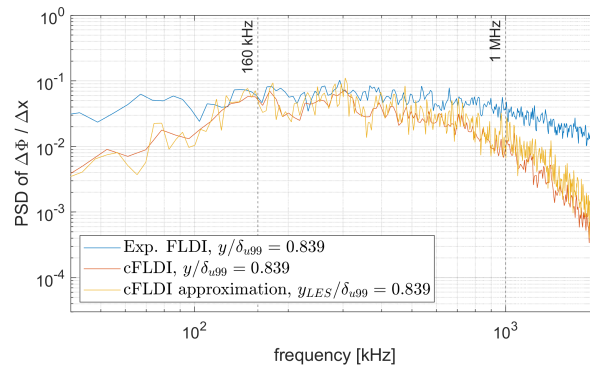


**Figure 19.** Comparison between spectra of phase differences at a single probing location. The spectra are obtained from experimental FLDI, cFLDI on the LES solution and a simplified, approximate conversion directly on the LES. The lower and upper frequency bounds for the comparison are shown as dashed lines.

As expected from the previous observations, the results show strong similarities, despite the large complexity gap between the cFLDI algorithm and the straightforward  $\Delta\Phi_{\text{direct}}$  estimation. Most importantly, there is similarity between the latter and the experimental data. This shows that useful comparisons might also be performed using a very simple formulation on the LES flowfield, in the absence of a complex cFLDI algorithm.

Evidently, the case presented here presents some facilitating properties, such as a very weak FLDI filtering effect within the volume of interest, low flowfield curvature and the computational simulation of the entire relevant volume. Nonetheless, the possibility of numerical and experimental comparison with such simplicity is encouraging.

## 5. Conclusions

This work has reported on the investigation of a turbulent boundary layer with cold walls at a free stream Mach number 7.4 and unit Reynolds number  $4.2 \times 10^6 \text{ m}^{-1}$ . Experimental shock tunnel data were analyzed in combination with a Large-Eddy Simulation (LES) under the same flowfield conditions to allow direct comparison. The main measurement technique was Focused Laser Differential Interferometry (FLDI), employed in a multi-foci arrangement with all probes parallel to each other for optimal signal cross-correlation.

The convection velocities of the density disturbances were experimentally measured using the cross-correlation of streamwise FLDI pairs along several locations inside the boundary layer and in the nearby free stream. Evidence of spurious low-frequency contributions likely coming from the nozzle shear layer highlighted the importance of high-pass filtering the FLDI signal before the cross-correlation operation. Results show the convection velocity to be highest slightly above the boundary layer edge at approximately 0.9 times the free stream velocity. Farther away from the boundary layer edge, the convection velocity was verified to drop to approximately 0.75 times that of the free stream, with larger disturbances propagating slightly faster than smaller ones. The magnitude of the measured convection velocity of the density disturbances is in agreement with the literature data on pressure disturbances in supersonic flows. An exception was observed when probing very close to the model wall, at approximately 7% of the boundary layer thickness, due to the contribution of the upper layers of the conical boundary layer to the FLDI signal. An improvement in future works might be obtained by increasing the beam convergence of the FLDI setup, which will enhance its filtering ability away from the focal plane. In the LES, the convection velocities presented similar behavior when pressure disturbances were evaluated, but significant differences for density disturbances. This discrepancy requires further investigation, which was beyond the scope of the present work. Future work shall also investigate the LES flowfield beyond the data directly related to FLDI diagnostics, e.g., temperature–velocity relationship, strong Reynolds analogy, among others.

The experimental spectra of the density fluctuations across the turbulent boundary layer were evaluated and compared to power laws reported in the literature for pressure fluctuations. The FLDI data were able to evidence the presence of regions with identifiable power laws of  $-7/3$ ,  $-11/3$  and  $-5$ . However, the upper limit of the frequency spectrum may have been biased by the FLDI frequency-dependent sensitive length, which was not compensated for in this work.

A framework to enable FLDI comparisons despite this complexity was explored by means of the use of computational FLDI (cFLDI) on the LES flowfield. Constraining conditions pertaining to both low and high ends of the frequency spectrum were detailed. The former was related to the noisy shear layer of the experimental flowfield and was calculated to be 160 kHz. The latter was around 10 MHz for the experimental FLDI and around 1 MHz for the computational solution. Furthermore, comparisons were performed in probing locations where the straight-line FLDI and the circular boundary layer within the LES domain presented significant intersection, as most of the flowfield disturbances were expected to be contained therein. Within these bounds, experimental and numerical direct comparisons yielded reasonable agreement. Encouraging agreement was also seen when a simple line integral of the computational data was analyzed in place of the complex cFLDI algorithm.

Overall, these observations present a positive scenario for future developments towards the understanding of high-speed turbulence, concerning experimental and numerical comparisons. In the absence of a complete model of cFLDI in groups focused on numerical investigations, useful data for spectral comparisons with experiments may be provided in a much simpler manner. At the same time, data provided by experimentalists can be used with minimal post-processing in numerical comparisons, as long as the necessary information for the determination of the constraining frequency bounds is also provided.

**Author Contributions:** Conceptualization, G.P.C., A.W., T.T. and C.S.; Data curation, G.P.C. and T.T.; Formal analysis, G.P.C.; Funding acquisition, A.W. and C.S.; Investigation, G.P.C., A.W. and T.T.; Methodology, G.P.C.; Project administration, G.P.C., A.W. and C.S.; Resources, A.W. and C.S.; Software, G.P.C. and T.T.; Supervision, A.W. and C.S.; Validation, G.P.C. and T.T.; Visualization, G.P.C.; Writing—original draft, G.P.C.; Writing—review and editing, A.W., T.T. and C.S. All authors have read and agreed to the published version of the manuscript.

**Funding:** This research received no external funding.

**Data Availability Statement:** The data that support the findings of this study are available from the corresponding author upon reasonable request.

**Acknowledgments:** The support given by Klaus Hannemann and Peter J. Klar is deeply appreciated. The authors also wish to acknowledge the assistance of Mariasole Laureti and the HEG team, particularly Ingo Schwendtko, Uwe Frenzel, Fabian Glasewald, Jan Martinez Schramm and Divek Surujhlal. The technical discussions with Victor C. B. Sousa and Emmanuel Gil Torres are also appreciated.

**Conflicts of Interest:** The authors declare no conflicts of interest.

### Abbreviations

The following abbreviations are used in this manuscript:

CFD	Computational Fluid Dynamics
cFLDI	Computational Focused Laser Differential Interferometer
DNS	Direct Numerical Simulation
FLDI	Focused Laser Differential Interferometer
HEG	High-Enthalpy Shock Tunnel Göttingen
LES	Large-Eddy Simulation
RANS	Reynolds-Averaged Navier–Stokes
SA	Spalart–Allmaras
QSV	Quasi-Spectral Viscosity

### Appendix A

A complete set of flowfield parameters, aimed at allowing the flowfield investigated in the present paper to be reproduced, is given in this appendix.

In the experiments, the cone model is placed partly inside the nozzle. This is needed to allow the investigation of the fully developed turbulent boundary layer at  $x = 825$  mm, as seen in Section 2.1, while using the existing test section windows in HEG and avoiding any effects of the nozzle shear layer interacting with the model. Nevertheless, the tip of the model is positioned in a region of the nozzle where the flowfield surrounding it is already sufficiently developed.

Flowfield information is extracted from a RANS solution of the nozzle flow, calculated from experimental stagnation conditions that were measured in the present investigation. The extraction is performed along a line upstream of the shock wave produced by the cone model, as shown in Figure A1.

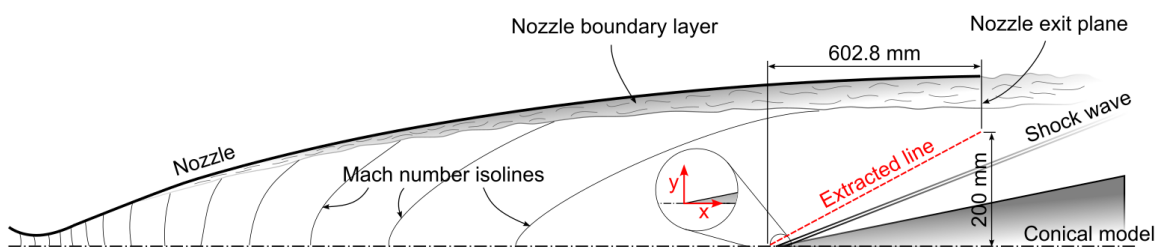


**Figure A1.** Topology of the flowfield around the cone model partly inside the nozzle. The line along which spatially resolved properties are extracted is highlighted.

The flowfield properties are separated into two groups, depending on their variation along the extracted line. The properties displayed in Table A1 present fluctuations in the order of 0.1% and are therefore assumed constant. In the table,  $Y_i$  refers to the mass fraction of species  $i$ ,  $\gamma$  is the ratio of specific heats and  $R$  is the gas constant.

**Table A1.** Flowfield properties that are constant along the extracted line from the RANS solution of the nozzle, calculated under experimentally observed stagnation conditions.

$p_0$ [MPa]	$Y_{N_2}$ [-]	$Y_{O_2}$ [-]	$Y_{NO}$ [-]	$Y_O$ [-]	$\gamma$ [-]	$R$ [J/(kg·K)]
19.265	0.75414	0.21825	0.02754	0.00007	1.3989	288.21

In Table A2, the properties showing non-negligible variation are listed with the spatial resolution. A total of 6 points are given for each property, uniformly distributed along the extracted line. When these points are used as references for a spline interpolation, the spatial distributions of the flowfield properties are reproduced with  $\pm 0.1\%$  accuracy. The coordinate system has its origin at the tip of the cone model, as shown in Figure A1. The velocity components along the  $x$  and  $y$  axes are denoted  $u$  and  $v$ , respectively. Although  $u$  is nearly constant, it is included in Table A2 for completeness.

**Table A2.** Spatially resolved flowfield properties, extracted along a line from the RANS solution of the nozzle, calculated under experimentally observed stagnation conditions.

$x$ [m]	$y$ [m]	$u$ [m/s]	$v$ [m/s]	$p$ [Pa]	$T$ [K]	$M$ [-]	$\mu \cdot 10^5$ [kg/(m·s)]	$\rho$ [kg/m <sup>3</sup> ]
-0.01838	0.00	2366.8	0.0	2487.2	266.70	7.2180	1.6822	0.032358
0.10218	0.04	2368.0	7.9	2399.5	263.95	7.2591	1.6683	0.031542
0.22274	0.08	2369.3	16.9	2292.7	260.54	7.3107	1.6511	0.030532
0.34331	0.12	2369.9	21.3	2250.8	259.19	7.3315	1.6443	0.030130
0.46387	0.16	2369.2	18.1	2316.1	261.37	7.2986	1.6553	0.030746
0.58444	0.20	2366.5	6.2	2522.0	267.80	7.2022	1.6877	0.032675

## References

- Ingenito, A.; Bruno, C. Physics and Regimes of Supersonic Combustion. *AIAA J.* **2010**, *48*, 515–525. [[CrossRef](#)]
- Roy, C.J.; Blottner, F.G. Review and assessment of turbulence models for hypersonic flows. *Prog. Aerosp. Sci.* **2006**, *42*, 469–530. [[CrossRef](#)]
- Pirozzoli, S.; Bernardini, M. Turbulence in supersonic boundary layers at moderate Reynolds number. *J. Fluid Mech.* **2011**, *688*, 120. [[CrossRef](#)]
- Duan, L.; Choudhari, M.M.; Zhang, C. Pressure fluctuations induced by a hypersonic turbulent boundary layer. *J. Fluid Mech.* **2016**, *804*, 578–607. [[CrossRef](#)] [[PubMed](#)]
- Zhang, C.; Duan, L.; Choudhari, M.M. Direct Numerical Simulation Database for Supersonic and Hypersonic Turbulent Boundary Layers. *AIAA J.* **2018**, *56*, 4297–4311. [[CrossRef](#)] [[PubMed](#)]
- Harvey, J.; Bergman, R.; Holden, M. An experimental study of hypersonic turbulence on a sharp cone. In Proceedings of the 20th Fluid Dynamics, Plasma Dynamics and Lasers Conference, Buffalo, NY, USA, 12–14 June 1989. . [[CrossRef](#)]
- Yoder, D.; DeBonis, J.; Georgiadis, N. Modeling of turbulent free shear flows. *Comput. Fluids* **2015**, *117*, 212–232. [[CrossRef](#)]
- Papamoschou, D.; Robey, H.F. Optical technique for direct measurement of power spectra in compressible turbulence. *Exp. Fluids* **1994**, *17*, 10–15. [[CrossRef](#)]
- Duan, L.; Choudhari, M.M.; Wu, M. Numerical study of acoustic radiation due to a supersonic turbulent boundary layer. *J. Fluid Mech.* **2014**, *746*, 165–192. [[CrossRef](#)]
- Lawson, J.M.; Neet, M.C.; Hofferth, J.W.; Austin, J.M. Supersonic Freestream Density Fluctuations from Focused Laser Differential Interferometry and Pitot-Probe Measurements. *AIAA J.* **2022**, *60*, 5173–5186. [[CrossRef](#)]
- Gillespie, G.I.; Ceruzzi, A.P.; Laurence, S.J. A multi-point focused laser differential interferometer for characterizing freestream disturbances in hypersonic wind tunnels. *Exp. Fluids* **2022**, *63*, 180. [[CrossRef](#)]
- Laufer, J. Some Statistical Properties of the Pressure Field Radiated by a Turbulent Boundary Layer. *Phys. Fluids* **1964**, *7*, 1191. [[CrossRef](#)]
- Martin, M.P. Direct numerical simulation of hypersonic turbulent boundary layers. Part 1. Initialization and comparison with experiments. *J. Fluid Mech.* **2007**, *570*, 347–364. [[CrossRef](#)]

14. Bernardini, M.; Pirozzoli, S. Wall pressure fluctuations beneath supersonic turbulent boundary layers. *Phys. Fluids* **2011**, *23*, 085102. [[CrossRef](#)]
15. Lagha, M.; Kim, J.; Eldredge, J.D.; Zhong, X. Near-wall dynamics of compressible boundary layers. *Phys. Fluids* **2011**, *23*, 065109. [[CrossRef](#)]
16. Duan, L.; Beekman, I.; Martin, M.P. Direct numerical simulation of hypersonic turbulent boundary layers. Part 3. Effect of Mach number. *J. Fluid Mech.* **2011**, *672*, 245–267. [[CrossRef](#)]
17. Duan, L.; Martin, M.P. Direct numerical simulation of hypersonic turbulent boundary layers. Part 4. Effect of high enthalpy. *J. Fluid Mech.* **2011**, *684*, 25–59. [[CrossRef](#)]
18. Zhang, C.; Duan, L.; Choudhary, M.M. Acoustic Radiation from a Mach 14 Turbulent Boundary layer. In Proceedings of the 54th AIAA Aerospace Sciences Meeting, San Diego, CA, USA, 4–8 January 2016; . [[CrossRef](#)]
19. Zhang, C.; Duan, L.; Choudhari, M.M. Effect of wall cooling on boundary-layer-induced pressure fluctuations at Mach 6. *J. Fluid Mech.* **2017**, *822*, 5–30. [[CrossRef](#)]
20. Wenzel, C.; Selent, B.; Kloker, M.; Rist, U. DNS of compressible turbulent boundary layers and assessment of data/scaling-law quality. *J. Fluid Mech.* **2018**, *842*, 428–468. [[CrossRef](#)]
21. Duan, L.; Choudhari, M.M.; Chou, A.; Munoz, F.; Radespiel, R.; Schilden, T.; Schröder, W.; Marineau, E.C.; Casper, K.M.; Chaudhry, R.S.; et al. Characterization of Freestream Disturbances in Conventional Hypersonic Wind Tunnels. *J. Spacecr. Rocket.* **2019**, *56*, 357–368. [[CrossRef](#)]
22. Chen, Y.; Scalo, C. Trapped waves in supersonic and hypersonic turbulent channel flow over porous walls. *J. Fluid Mech.* **2021**, *920*, A24. [[CrossRef](#)]
23. Xu, D.; Wang, J.; Wan, M.; Yu, C.; Li, X.; Chen, S. Compressibility effect in hypersonic boundary layer with isothermal wall condition. *Phys. Rev. Fluids* **2021**, *6*, 054609. [[CrossRef](#)]
24. Xu, D.; Wang, J.; Wan, M.; Yu, C.; Li, X.; Chen, S. Effect of wall temperature on the kinetic energy transfer in a hypersonic turbulent boundary layer. *J. Fluid Mech.* **2021**, *929*, A33. [[CrossRef](#)]
25. Huang, J.; Duan, L.; Choudhari, M.M. Direct numerical simulation of hypersonic turbulent boundary layers: effect of spatial evolution and Reynolds number. *J. Fluid Mech.* **2022**, *937*, A3. [[CrossRef](#)]
26. Trettel, A.; Larsson, J. Mean velocity scaling for compressible wall turbulence with heat transfer. *Phys. Fluids* **2016**, *28*, 026102. [[CrossRef](#)]
27. Pecnik, R.; Patel, A. Scaling and modelling of turbulence in variable property channel flows. *J. Fluid Mech.* **2017**, *823*, R1. [[CrossRef](#)]
28. Owen, F.K.; Horstman, C.C. On the structure of hypersonic turbulent boundary layers. *J. Fluid Mech.* **1972**, *53*, 611–636. [[CrossRef](#)]
29. Williams, O.J.; Sahoo, D.; Baumgartner, M.L.; Smits, A.J. Experiments on the structure and scaling of hypersonic turbulent boundary layers. *J. Fluid Mech.* **2018**, *834*, 237–270. [[CrossRef](#)]
30. Tsuji, Y.; Fransson, J.H.M.; Alfredsson, P.H.; Johansson, A.V. Pressure statistics and their scaling in high-Reynolds-number turbulent boundary layers. *J. Fluid Mech.* **2007**, *585*, 1–40. [[CrossRef](#)]
31. Choi, H.; Moin, P. On the space-time characteristics of wall-pressure fluctuations. *Phys. Fluids A Fluid Dyn.* **1990**, *2*, 1450–1460. [[CrossRef](#)]
32. Parziale, N. Slender-Body Hypervelocity Boundary-Layer Instability. Ph.D. Thesis, California Institute of Technology, Pasadena, CA, USA, 2013.
33. Fulghum, M.R. Turbulence Measurements in High-Speed Wind Tunnels Using Focusing Laser Differential Interferometry. Ph.D. Thesis, The Pennsylvania State University, University Park, PA, USA, 2014.
34. Chou, A.; Leidy, A.; King, R.A.; Bathel, B.F.; Herring, G. Measurements of Freestream Fluctuations in the NASA Langley 20-Inch Mach 6 Tunnel. In Proceedings of the 2018 Fluid Dynamics Conference, Atlanta, GA, USA, 25–29 June 2018. . [[CrossRef](#)]
35. Birch, B.; Buttsworth, D.; Zander, F. Measurements of freestream density fluctuations in a hypersonic wind tunnel. *Exp. Fluids* **2020**, *61*, 158. [[CrossRef](#)]
36. Ceruzzi, A.; McManamen, B.; Cadou, C.P. Demonstration of Two-Point Focused Laser Differential Interferometry (2pFLDI) in a Mach 18 flow. In Proceedings of the AIAA Scitech 2021 Forum, Virtual Event, 11–15. 19–21 January 2021. . [[CrossRef](#)]
37. Bathel, B.F.; Weisberger, J.M.; Herring, G.C.; King, R.A.; Jones, S.B.; Kennedy, R.E.; Laurence, S.J. Two-point, parallel-beam focused laser differential interferometry with a Nomarski prism. *Appl. Opt.* **2020**, *59*, 244. [[CrossRef](#)] [[PubMed](#)]
38. Weisberger, J.M.; Bathel, B.F.; Herring, G.C.; Buck, G.M.; Jones, S.B.; Cavone, A.A. Multi-point line focused laser differential interferometer for high-speed flow fluctuation measurements. *Appl. Opt.* **2020**, *59*, 11180. [[CrossRef](#)] [[PubMed](#)]
39. Xiong, Y.; Yu, T.; Lin, L.; Zhao, J.; Wu, J. Nonlinear Instability Characterization of Hypersonic Laminar Boundary Layer. *AIAA J.* **2020**, *58*, 5254–5263. [[CrossRef](#)]
40. Benitez, E.K.; Jewell, J.S.; Schneider, S.P. Focused Laser Differential Interferometry with Contoured Tunnel Windows. *AIAA J.* **2021**, *59*, 419–429. [[CrossRef](#)]
41. Gragston, M.; Siddiqui, F.; Schmisser, J.D. Detection of second-mode instabilities on a flared cone in Mach 6 quiet flow with linear array focused laser differential interferometry. *Exp. Fluids* **2021**, *62*, 81. [[CrossRef](#)]
42. Siddiqui, F.; Gragston, M.; Saric, W.S.; Bowersox, R.D.W. Mack-mode instabilities on a cooled flared cone with discrete roughness elements at Mach 6. *Exp. Fluids* **2021**, *62*, 213. [[CrossRef](#)]

43. Siddiqui, F.; Gragston, M.; Bowersox, R.D.W. Measurement of Wall-Cooling Effects on Hypersonic Boundary-Layer Transition Using Focused Laser Differential Interferometry. *AIAA J.* **2022**, *60*, 6214–6224. [[CrossRef](#)]
44. Schmidt, B.E.; Shepherd, J.E. Analysis of focused laser differential interferometry. *Appl. Opt.* **2015**, *54*, 8459. [[CrossRef](#)]
45. Lawson, J.M.; Neet, M.C.; Grossman, I.J.; Austin, J.M. Static and dynamic characterization of a focused laser differential interferometer. *Exp. Fluids* **2020**, *61*, 187. [[CrossRef](#)]
46. Hameed, A.; Parziale, N.J. Focused Laser Differential Interferometric Investigation of Turbulent Jet Spectra. *J. Spacecr. Rocket.* **2022**, *59*, 1565–1573. [[CrossRef](#)]
47. Ceruzzi, A.P.; Cadou, C.P. Interpreting single-point and two-point focused laser differential interferometry in a turbulent jet. *Exp. Fluids* **2022**, *63*, 112. [[CrossRef](#)]
48. Lawson, J.M.; Austin, J.M. Focused laser differential interferometer response to shock waves. *Meas. Sci. Technol.* **2021**, *32*, 055203. [[CrossRef](#)]
49. Camillo, G.P.; Wagner, A. Focused laser differential interferometry post-processing methodology for flowfields with circular symmetry. *Rev. Sci. Instrum.* **2023**, *94*, 045102. [[CrossRef](#)]
50. Benitez, E.K.; Borg, M.P.; Rhodes, C.; Jewell, J.S. Optical-Axis Spatial Sensitivity of a Simulated Focused Laser Differential Interferometer. *AIAA J.* **2023**, *61*, 1–14. [[CrossRef](#)]
51. Benitez, E.K.; Jewell, J.S. Simulated Focused Laser Differential Interferometry of Time-Varying Signals. In Proceedings of the AIAA SCITECH 2022 Forum, San Diego, CA, USA & Virtual, 3–7 January 2022. . [[CrossRef](#)]
52. Benitez, E.K.; Borg, M.P.; Hill, J.L.; Aultman, M.T.; Duan, L.; Running, C.L.; Jewell, J.S. Quantitative focused laser differential interferometry with hypersonic turbulent boundary layers. *Appl. Opt.* **2022**, *61*, 9203. [[CrossRef](#)] [[PubMed](#)]
53. Deutsches Zentrum für Luft - und Raumfahrt (DLR). The High Enthalpy Shock Tunnel Göttingen of the German Aerospace Center (DLR). *J. Large-Scale Res. Facil.* **2018**, *4*, A133. .: 10.17815/jlsrf-4-168. [[CrossRef](#)]
54. Wagner, A. *Passive Hypersonic Transition Control by Means of Ultrasonically Absorptive Thermal Protection Materials (UAT)*; Report AFRL-AFOSR-UK-TR-2020-0025; Deutsches Zentrum für Luft- und Raumfahrt: Cologne, Germany, 2020.
55. Wartemann, V.; Camillo, G.P.; Reiter, P.; Neumann, J.; Wagner, A. Influence of transpiration cooling on second-mode instabilities investigated on hypersonic, conical flows. *CEAS Space J.* **2019**, *11*, 341–350. [[CrossRef](#)]
56. Wartemann, V.; Camillo, G.P.; Neumann, J.; Weber, A.; Wagner, A. Stability Analyses of Hypersonic, Conical Flows with Transpiration Cooling. In *IUTAM Laminar-Turbulent Transition*; Springer International Publishing: Cham, Switzerland, 2021; pp. 671–689. . [[CrossRef](#)]
57. Ceruzzi, A.; Cadou, C.P. Simultaneous Velocity and Density Gradient Measurements using Two-Point Focused Laser Differential Interferometry. In Proceedings of the AIAA Scitech 2019 Forum, San Diego, CA, USA, 7–11 January 2019. . [[CrossRef](#)]
58. Camillo, G.P.; Wagner, A. A low-effort and inexpensive methodology to determine beam separation distance of multi-foci FLDI. *Exp. Fluids* **2022**, *63*, 53. [[CrossRef](#)]
59. Sanderson, S.R. Simple, adjustable beam splitting element for differential interferometers based on photoelastic birefringence of a prismatic bar. *Rev. Sci. Instrum.* **2005**, *76*, 113703. [[CrossRef](#)]
60. Lawson, J.M.; Neet, M.C.; Grossman, I.J.; Austin, J.M. Characterization of a Focused Laser Differential Interferometer. In Proceedings of the AIAA Scitech 2019 Forum, San Diego, CA, USA, 7–11 January 2019. . [[CrossRef](#)]
61. Nagarajan, S.; Lele, S.; Ferziger, J. A robust high-order compact method for large eddy simulation. *J. Comput. Phys.* **2003**, *191*, 392–419. [[CrossRef](#)]
62. Sousa, V.C.B.; Scalo, C. A Unified Quasi-Spectral Viscosity (QSV) Approach to Shock Capturing and Large-Eddy Simulation. *J. Comput. Phys.* **2022**, *459*, 111139. [[CrossRef](#)]
63. Gottlieb, S. On high order strong stability preserving Runge-Kutta and multi step time discretizations. *J. Sci. Comput.* **2005**, *25*, 105–128. [[CrossRef](#)]
64. Lele, S.K. Compact finite difference scheme with spectral-like resolution. *J. Comput. Phys.* **1992**, *103*, 16–42. [[CrossRef](#)]
65. Spalart, P.R.; Allmaras, S.R. A One-Equation Turbulence Model for Aerodynamics Flow. In Proceedings of the 30th Aerospace Sciences Meeting and Exhibit, Reno, NV, USA, 6–9 January 1992. . [[CrossRef](#)]
66. Taylor, G.I.; Maccoll, J.W. The Air Pressure on a Cone Moving at High Speeds.—I. *Proc. R. Soc. Lond. Series A* **1933**, *139*, 278–297. [[CrossRef](#)]
67. Urbin, G.; Knight, D. Large-eddy simulation of a supersonic boundary layer using an unstructured grid. *AIAA J.* **2001**, *39*, 1288–1295. [[CrossRef](#)]
68. Toki, T.; Sousa, V.C.B.; Chen, Y.; Camillo, G.P.; Wagner, A.; Scalo, C. Large-eddy simulation of a hypersonic turbulent boundary layer over a cone in support of focused laser differential interferometry (FLDI) measurements. In Proceedings of the 12th International Symposium on Turbulence and Shear Flow Phenomena, Osaka, Japan, 19–22 July 2022.
69. Born, M.; Wolf, E. *Principles of Optics*, 7th ed.; Cambridge University Press: Cambridge, UK, 1999.
70. Tennekes, H.; Lumley, J.L. *A First Course in Turbulence*; The MIT Press: Cambridge, MA, USA, 1972.
71. Phillips, O.M. On the generation of sound by supersonic turbulent shear layers. *J. Fluid Mech.* **1960**, *9*, 1–28. [[CrossRef](#)]
72. George, W.J.; Beuther, P.; Arndt, R. Pressure spectra in turbulent free shear flows. In Proceedings of the 6th Aeroacoustics Conference, Hartford, CT, USA, 6–8 June 1980. . [[CrossRef](#)]
73. Biagioni, L.; d’Agostino, L. Measurement of energy spectra in weakly compressible turbulence. In Proceedings of the 30th Fluid Dynamics Conference, Norfolk, VA, USA, 28 June–1 July 1999. [[CrossRef](#)]

74. Bernardini, M.; Pirozzoli, S.; Grasso, F. The wall pressure signature of transonic shock/boundary layer interaction. *J. Fluid Mech.* **2011**, *671*, 288–312. [\[CrossRef\]](#)
75. Masutti, D.; Spinosa, E.; Chazot, O.; Carbonaro, M. Disturbance Level Characterization of a Hypersonic Blowdown Facility. *Phys. Fluids* **2012**, *50*, 2720–2730. [\[CrossRef\]](#)
76. Ceruzzi, A.P. Development of Two-Point Focused Laser Differential Interferometry for Applications in High-Speed Wind Tunnels. Ph.D. Thesis, University of Maryland, College Park, MD, USA, 2022.

**Disclaimer/Publisher’s Note:** The statements, opinions and data contained in all publications are solely those of the individual author(s) and contributor(s) and not of MDPI and/or the editor(s). MDPI and/or the editor(s) disclaim responsibility for any injury to people or property resulting from any ideas, methods, instructions or products referred to in the content.

## 4. Conclusions

This Ph.D. work has focused on the problem of paucity of experimental information on hypersonic turbulent boundary layers. The technique of Focused Laser Differential Interferometry (FLDI) was employed to obtain off-wall density fluctuation measurements in a shock tunnel, with high temporal and spatial resolution.

The main contributions of this thesis have been: 1) the new experimental dataset of spectral distributions and convection velocities of density fluctuations, both given with wall-normal resolution; and 2) the analysis of direct comparisons between experimental FLDI and computational FLDI (cFLDI) performed on a LES solution of the flowfield under the experimentally observed conditions.

The measured convection velocities based on density disturbances presented similar relative magnitudes to previous investigations of pressure disturbances at neighboring Mach numbers. The profile of convection velocity along the boundary layer, on the other hand, was different than existing numerical data. However, the flowfield conditions across the cases were not identical, in particular regarding wall temperature, which could be the cause of the discrepancies. The frequency spectra of density disturbances measured up to 10 MHz showed regions governed by clear power laws, with powers that are usually found in pressure spectra. Regarding the analysis of the experimental and numeric shock tunnel flowfields, the proof obtained in the present work that they can be directly compared using FLDI output (real or virtual) is of great importance. It represents a new form of approaching the issue of lack of experimental data to test against turbulence models and flowfield simulations. The comparisons are further facilitated in cases where the FLDI divergence angle is shallow, such as the one reported here. Under such conditions, it was observed that the cFLDI can be replaced with a simple line integral on the numeric flowfield, not distant in complexity to a numerical schlieren, for example. Hence this is an approach that may be implemented in CFD visualization and analysis softwares right now.

Prior to the experiments, the FLDI instrument and auxiliary resources, e.g., the frequency response of the instrument and techniques to measure the placement of the beams, were iterated upon and optimized. The experimental data collected in the High Enthalpy Shock Tunnel Göttingen (HEG) was analyzed with attention to experimental uncertainties and limitations, to provide future investigators who may be interested in this data with as clear a picture as possible.

Along those same lines, the shock tunnel flowfield explored in the investigation reported in this thesis has been extensively detailed in the pertinent publication. This was done in order to allow reproducibility of the flowfield and the observed results. Hopefully, this may be used by future investigators as an experimental baseline to compare against different simulations and models, such as to contribute to advance the current understanding of high-speed turbulence.

In the course of reaching the main contributions summarized above, two relevant accessory contributions are noteworthy. The first one is an alternative low-effort technique to measure the separation distance between FLDI probes meant for velocimetry. The proposed method was able to provide measurements of similar quality to directly imaging the beams with a beam profiler, but at a fraction of the cost and with more flexibility. The relevance of this measurement is highlighted by the fact that any imprecision within it is directly carried over to the velocity measurements performed with FLDI. The results presented in this work have shown that multi-foci FLDI instruments are capable of high-quality convection velocity measurements, as long as proper attention is given to calibrating the system.

The second accessory contribution is a post-processing methodology for FLDI measurements performed in flowfields with circular symmetry. The proposed approach includes this kind of flowfield in the restricted group of cases where the conversion of FLDI data into flowfield quantities is possible analytically. Furthermore, this development has introduced the cFLDI as a helping tool to aid in the assessment of simplifying hypotheses, which might be assumed when developing FLDI data conversion methods. Hopefully, this kind of approach may be used in future efforts to advance FLDI data interpretation, further expanding the scientific gains enabled by the technique.

Turning to future works, a few improvements can be suggested to build upon the work presented here. In spite of all its advantages, the FLDI is a point measurement. In order to obtain the turbulent boundary layer information across its thickness presented here, several different shock tunnel runs were necessary. Such effort is budget- and work-intensive, and combining different shock tunnel runs, although possible once free stream repeatability is adequately assessed, increases uncertainties. A means to avoid this problem is to further multiply the FLDI probes. Even though the multiplication strategies adopted in the present work could be employed in a sequential, repeated manner, that can be very cumbersome to implement. Better approaches have been proposed by works referenced in this thesis that could be implemented in the FLDI system used here, such as using a diffractive optical element to produce an array of beams [48], or a cylindrical lens to produce a stretched line at the focal plane of the system [68].

Additionally, the blast wave technique explored in the first publication could only be applied to obtain the separation distance between two independent FLDI probes,  $\Delta x_2$ . To measure the internal separation of the beams in one FLDI probe,  $\Delta x_1$ , other methods must still be employed, such as the weak lens approach or direct beam imaging. It might be possible to use an approach similar to the blast wave technique to also obtain  $\Delta x_1$ . Perhaps a stronger blast wave would be needed, to take advantage of its sharper wave front. Or some other way to interpret the acquired signal.

Complementing the improvements on the experimental side, a continued effort may also benefit the numeric flowfield. The LES computations used in the present work presented remarkable temporal resolution. However, the analysis has shown that the grid refinement was far more restrictive than the time steps. As such, a balance can be sought in future efforts, in a way that the spatial resolution is

improved. The experimental measurements performed in HEG with an optimized FLDI have shown frequency content to be detectable up to 10 MHz. This can be used in combination with the expected flowfield velocities, to provide a target spatial resolution for the computational domain.



## Bibliography

- [1] E. R. van Driest. “The Problem of Aerodynamic Heating”. *Aeronautical Engineering Review* 15.10 (Oct. 1956), pp. 26–41.
- [2] B. C. Chynoweth, C. Ward, and S. P. Schneider. “Measuring transition and instabilities in a Mach 6 hypersonic quiet wind tunnel”. In: *44th AIAA Fluid Dynamics Conference*. Atlanta, GA, USA, 16–20 June 2014. DOI: 10.2514/6.2014-2643.
- [3] M. T. Semper and R. D. Bowersox. “Tripping of a hypersonic low-Reynolds-number boundary layer”. *AIAA Journal* 55.3 (Mar. 2017), pp. 808–817. DOI: 10.2514/1.J055341.
- [4] D. A. Yoder, J. R. DeBonis, and N. J. Georgiadis. “Modeling of Turbulent Free Shear Flows”. In: *21st AIAA Computational Fluid Dynamics Conference*. San Diego, CA, USA, 24–27 June 2013. DOI: 10.2514/6.2013-2721.
- [5] L. Duan and M. P. Martin. “Effect of Finite-rate Chemical Reactions on Turbulence in Hypersonic Turbulence Boundary Layers”. In: *47th AIAA Aerospace Sciences Meeting Including The New Horizons Forum and Aerospace Exposition*. Orlando, FL, USA, 5–8 Jan. 2009. DOI: 10.2514/6.2009-588.
- [6] M. Martin et al. “DNS of reacting hypersonic turbulent boundary layers”. In: *29th AIAA, Fluid Dynamics Conference*. Albuquerque, NM, USA, 15–18 June 1998. DOI: 10.2514/6.1998-2817.
- [7] L. J. DeChant and J. A. Smith. “An Approximate Turbulent Pressure Fluctuation Frequency Spectra for a Finite Supersonic Plate”. In: *53rd AIAA Aerospace Sciences Meeting*. Kissimmee, FL, USA, 5–9 Jan. 2015. DOI: 10.2514/6.2015-1985.
- [8] L. Duan, M. M. Choudhari, and C. Zhang. “Pressure fluctuations induced by a hypersonic turbulent boundary layer”. *Journal of Fluid Mechanics* 804 (Sept. 2016), pp. 578–607. DOI: 10.1017/jfm.2016.548.
- [9] K. Raman. “Surface pressure fluctuations in hypersonic turbulent boundary layers”. In: *Aeroacoustics Conference*. Seattle, WA, USA, 15–17 Oct. 1973. DOI: 10.2514/6.1973-997.
- [10] S. P. Schneider. “Effects of Roughness on Hypersonic Boundary-Layer Transition”. *Journal of Spacecraft and Rockets* 45.2 (Mar. 2008), pp. 193–209. DOI: 10.2514/1.29713.
- [11] L. Duan, M. M. Choudhari, and M. Wu. “Numerical study of acoustic radiation due to a supersonic turbulent boundary layer”. *Journal of Fluid Mechanics* 746 (Mar. 2014), pp. 165–192. DOI: 10.1017/jfm.2014.116.
- [12] L. Duan et al. “Characterization of Freestream Disturbances in Conventional Hypersonic Wind Tunnels”. *Journal of Spacecraft and Rockets* 56.2 (Mar. 2019), pp. 357–368. DOI: 10.2514/1.a34290.

- [13] M. Lagha et al. “Near-wall dynamics of compressible boundary layers”. *Physics of Fluids* 23.6 (June 2011), p. 065109. DOI: 10.1063/1.3600659.
- [14] S. Pirozzoli and M. Bernardini. “Turbulence in supersonic boundary layers at moderate Reynolds number”. *Journal of Fluid Mechanics* 688 (Oct. 2011), pp. 120–168. DOI: 10.1017/jfm.2011.368.
- [15] O. J. Williams et al. “Experiments on the structure and scaling of hypersonic turbulent boundary layers”. *Journal of Fluid Mechanics* 834 (Nov. 2018), pp. 237–270. DOI: 10.1017/jfm.2017.712.
- [16] C. Wenzel et al. “DNS of compressible turbulent boundary layers and assessment of data/scaling-law quality”. *Journal of Fluid Mechanics* 842 (Mar. 2018), pp. 428–468. DOI: 10.1017/jfm.2018.179.
- [17] S. Wang et al. “Large Eddy Simulation of Supersonic Boundary Layer Transition over a Flat-Plate Based on the Spatial Mode”. *Advances in Mechanical Engineering* 6 (Jan. 2014), p. 350203. DOI: 10.1155/2014/350203.
- [18] C. Zhang, L. Duan, and M. M. Choudhary. “Acoustic Radiation from a Mach 14 Turbulent Boundary layer”. In: *54th AIAA Aerospace Sciences Meeting*. San Diego, CA, USA, 4–8 Jan. 2016. DOI: 10.2514/6.2016-0048.
- [19] L. Smits, P. Martin, and S. Girimaji. “Current Status of Basic Research in Hypersonic Turbulence”. In: *47th AIAA Aerospace Sciences Meeting including The New Horizons Forum and Aerospace Exposition*. Orlando, FL, USA, 5–8 Jan. 2009. DOI: 10.2514/6.2009-151.
- [20] E. F. Spina, A. J. Smits, and S. K. Robinson. “The Physics of Supersonic Turbulent Boundary Layers”. *Annual Review of Fluid Mechanics* 26.1 (Jan. 1994), pp. 287–319. DOI: 10.1146/annurev.fl.26.010194.001443.
- [21] Z. B. Lin and J. K. Harvey. “Experimental study of the hypersonic turbulent boundary layer on a cold slender cone”. *Journal of Thermophysics and Heat Transfer* 3.2 (Apr. 1989), pp. 105–111. DOI: 10.2514/3.136.
- [22] C. Zhang, L. Duan, and M. M. Choudhari. “Direct Numerical Simulation Database for Supersonic and Hypersonic Turbulent Boundary Layers”. *AIAA Journal* 56.11 (Nov. 2018), pp. 4297–4311. DOI: 10.2514/1.J057296.
- [23] J. Harvey, R. Bergman, and M. Holden. “An experimental study of hypersonic turbulence on a sharp cone”. In: *20th Fluid Dynamics, Plasma Dynamics and Lasers Conference*. Buffalo, NY, USA, 12–14 June 1989. DOI: 10.2514/6.1989-1866.
- [24] D. Yoder, J. DeBonis, and N. Georgiadis. “Modeling of turbulent free shear flows”. *Computers & Fluids* 117 (Aug. 2015), pp. 212–232. DOI: 10.1016/j.compfluid.2015.05.009.
- [25] R. Pecnik and A. Patel. “Scaling and modelling of turbulence in variable property channel flows”. *Journal of Fluid Mechanics* 823 (June 2017), R1. DOI: 10.1017/jfm.2017.348.
- [26] Y. Tsuji et al. “Pressure statistics and their scaling in high-Reynolds-number turbulent boundary layers”. *Journal of Fluid Mechanics* 585 (Aug. 2007), pp. 1–40. DOI: 10.1017/s0022112007006076.

- 
- [27] C. J. Roy and F. G. Blottner. “Review and assessment of turbulence models for hypersonic flows”. *Progress in Aerospace Sciences* 42.7 (Oct. 2006), pp. 469–530. DOI: 10.1016/j.paerosci.2006.12.002.
- [28] D. Papamoschou and H. F. Robey. “Optical technique for direct measurement of power spectra in compressible turbulence”. *Experiments in Fluids* 17.1 (June 1994), pp. 10–15. DOI: 10.1007/bf02412798.
- [29] T. Aoyama et al. “Statistics of Energy Transfer in High-Resolution Direct Numerical Simulation of Turbulence in a Periodic Box”. *Journal of the Physical Society of Japan* 74.12 (Dec. 2005), pp. 3202–3212. DOI: 10.1143/jpsj.74.3202.
- [30] W. J. George, P. Beuther, and R. Arndt. “Pressure spectra in turbulent free shear flows”. In: *6th Aeroacoustics Conference*. Hartford, CT, USA, 6–8 June 1980. DOI: 10.2514/6.1980-985.
- [31] H. Tennekes and J. L. Lumley. *A First Course in Turbulence*. Massachusetts: The MIT Press, 1972. ISBN: 978-0-262-53630-1.
- [32] A. Wagner et al. “Combined free-stream disturbance measurements and receptivity studies in hypersonic wind tunnels by means of a slender wedge probe and direct numerical simulation”. *Journal of Fluid Mechanics* 842 (Mar. 2018), pp. 495–531. DOI: 10.1017/jfm.2018.132.
- [33] D. Neeb, D. Saile, and A. Gülhan. “Experiments on a smooth wall hypersonic boundary layer at Mach 6”. *Experiments in Fluids* 59.4 (Mar. 2018), p. 68. DOI: 10.1007/s00348-018-2518-z.
- [34] D. Zahradka et al. “Krypton Tagging Velocimetry (KTV) in Supersonic Turbulent Boundary Layers”. In: *54th AIAA Aerospace Sciences Meeting*. San Diego, CA, USA, 4–8 Jan. 2016. DOI: 10.2514/6.2016-1587.
- [35] L. E. Dogariu et al. “Femtosecond Laser Electronic Excitation Tagging Velocimetry in a Large-Scale Hypersonic Facility”. *AIAA Journal* 57.11 (Nov. 2019), pp. 4725–4737. DOI: 10.2514/1.j057759.
- [36] G. Smeets. “Laser Interferometer for High Sensitivity Measurements on Transient Phase Objects”. *IEEE Transactions on Aerospace and Electronic Systems* AES-8.2 (Mar. 1972), pp. 186–190. DOI: 10.1109/taes.1972.309488.
- [37] G. Smeets and A. George. *Laser Differential Interferometer Applications in Gas Dynamics*. Report 28/73. A. Goetz, translator, DTIC ADA307459. Institut Saint-Louis, 1973.
- [38] G. Smeets. “Flow Diagnostics by Laser Interferometry”. *IEEE Transactions on Aerospace and Electronic Systems* AES-13.2 (Mar. 1977), pp. 82–90. DOI: 10.1109/taes.1977.308441.
- [39] N. J. Parziale, J. E. Shepherd, and H. G. Hornung. “Differential Interferometric Measurement of Instability in a Hypervelocity Boundary Layer”. *AIAA Journal* 51.3 (Nov. 2012), pp. 750–754. DOI: 10.2514/1.J052013.
- [40] N. Parziale. “Slender-Body Hypervelocity Boundary-Layer Instability”. PhD thesis. Pasadena, CA, USA: California Institute of Technology, 2013.
- [41] M. Born and E. Wolf. *Principles of Optics*. 7th. Cambridge, UK: Cambridge University Press, 1999. ISBN: 978-0-521-64222-4.

- [42] J. S. Jewell et al. “Disturbance and Phase Speed Measurements for Shock Tubes and Hypersonic Boundary-Layer Instability”. In: *32nd AIAA Aerodynamic Measurement Technology and Ground Testing Conference*. Washington, D.C., USA, 13–17 June 2016. DOI: 10.2514/6.2016-3112.
- [43] B. F. Bathel et al. “Simultaneous focused laser differential interferometry and high-speed schlieren in a Mach 6 flow”. *Measurement Science and Technology* 32.9 (June 2021), p. 095907. DOI: 10.1088/1361-6501/abf67a.
- [44] E. K. Benitez, J. S. Jewell, and S. P. Schneider. “Focused Laser Differential Interferometry with Contoured Tunnel Windows”. *AIAA Journal* 59.2 (Feb. 2021), pp. 419–429. DOI: 10.2514/1.j060081.
- [45] A. Ceruzzi and C. P. Cadou. “Simultaneous Velocity and Density Gradient Measurements using Two-Point Focused Laser Differential Interferometry”. In: *AIAA Scitech 2019 Forum*. San Diego, CA, USA, 7-11 Jan. 2019. DOI: 10.2514/6.2019-2295.
- [46] A. Ceruzzi et al. “Investigation of Focused Laser Differential Interferometry (FLDI) Sensitivity Function”. In: *AIAA Scitech 2021 Forum*. Virtual Event, 11–15, 19–21 Jan. 2021. DOI: 10.2514/6.2021-1299.
- [47] A. P. Ceruzzi and C. P. Cadou. “Interpreting single-point and two-point focused laser differential interferometry in a turbulent jet”. *Experiments in Fluids* 63.7 (July 2022), p. 112. DOI: 10.1007/s00348-022-03459-w.
- [48] M. Gragston et al. “Linear array focused-laser differential interferometry for single-shot multi-point flow disturbance measurements”. *Optics Letters* 46.1 (Jan. 2021), pp. 154–157. DOI: 10.1364/ol.412495.
- [49] A. Hameed and N. J. Parziale. “Focused Laser Differential Interferometry Transfer Functions for Complex Density Disturbance Fields”. In: *AIAA AVIATION 2021 FORUM*. Virtual Event, 2–6 Aug. 2021. DOI: 10.2514/6.2021-2907.
- [50] A. Hameed and N. J. Parziale. “Focused Laser Differential Interferometric Investigation of Turbulent Jet Spectra”. *Journal of Spacecraft and Rockets* 59.5 (Sept. 2022), pp. 1565–1573. DOI: 10.2514/1.a35292.
- [51] J. S. Jewell et al. “Disturbance Speed Measurements in a Circular Jet via Double Focused Laser Differential Interferometry”. In: *AIAA Scitech 2019 Forum*. San Diego, CA, USA, 7–11 Jan. 2019. DOI: 10.2514/6.2019-2293.
- [52] G. S. Settles and M. R. Fulghum. “The Focusing Laser Differential Interferometer, an Instrument for Localized Turbulence Measurements in Refractive Flows”. *Journal of Fluids Engineering* 138.10 (July 2016). DOI: 10.1115/1.4033960.
- [53] J. M. Lawson et al. “Characterization of a Focused Laser Differential Interferometer”. In: *AIAA Scitech 2019 Forum*. San Diego, CA, USA, 7-11 Jan. 2019. DOI: 10.2514/6.2019-2296.
- [54] J. M. Lawson et al. “Static and dynamic characterization of a focused laser differential interferometer”. *Experiments in Fluids* 61.8 (Aug. 2020), p. 187. DOI: 10.1007/s00348-020-03013-6.

- 
- [55] B. Birch, D. Buttsworth, and F. Zander. “Measurements of freestream density fluctuations in a hypersonic wind tunnel”. *Experiments in Fluids* 61.7 (June 2020), p. 158. DOI: 10.1007/s00348-020-02992-w.
- [56] A. Ceruzzi, B. McManamen, and C. P. Cadou. “Demonstration of Two-Point Focused Laser Differential Interferometry (2pFLDI) in a Mach 18 flow”. In: *AIAA Scitech 2021 Forum*. Virtual Event, 11–15, 19–21 Jan. 2021. DOI: 10.2514/6.2021-0983.
- [57] A. Chou et al. “Measurements of Freestream Fluctuations in the NASA Langley 20-Inch Mach 6 Tunnel”. In: *2018 Fluid Dynamics Conference*. Atlanta, GA, USA, 25–29 June 2018. DOI: 10.2514/6.2018-3073.
- [58] G. Gillespie, A. Ceruzzi, and S. Laurence. “Multi-point Focused Laser Differential Interferometry for Noise Measurements in High-Speed Tunnels”. In: *AIAA AVIATION 2021 FORUM*. Virtual Event, 2–6 Aug. 2021. DOI: 10.2514/6.2021-2918.
- [59] G. I. Gillespie, A. P. Ceruzzi, and S. J. Laurence. “A multi-point focused laser differential interferometer for characterizing freestream disturbances in hypersonic wind tunnels”. *Experiments in Fluids* 63.11 (Nov. 2022), p. 180. DOI: 10.1007/s00348-022-03522-6.
- [60] J. M. Lawson et al. “Supersonic Freestream Density Fluctuations from Focused Laser Differential Interferometry and Pitot-Probe Measurements”. *AIAA Journal* 60.9 (Sept. 2022), pp. 5173–5186. DOI: 10.2514/1.j061432.
- [61] N. J. Parziale, J. E. Shepherd, and H. G. Hornung. “Free-stream density perturbations in a reflected-shock tunnel”. *Experiments in Fluids* 55.2 (Jan. 2014). DOI: 10.1007/s00348-014-1665-0.
- [62] B. F. Bathel et al. “Two-point, parallel-beam focused laser differential interferometry with a Nomarski prism”. *Applied Optics* 59.2 (Jan. 2020), p. 244. DOI: 10.1364/ao.59.000244.
- [63] E. K. Benitez, J. S. Jewell, and S. P. Schneider. “Focused Laser Differential Interferometry for Hypersonic Flow Instability Measurements with Contoured Tunnel Windows”. In: *AIAA Scitech 2020 Forum*. Orlando, FL, USA, 6–10 Jan. 2020. DOI: 10.2514/6.2020-1282.
- [64] M. Gragston, F. Siddiqui, and J. D. Schmisser. “Detection of second-mode instabilities on a flared cone in Mach 6 quiet flow with linear array focused laser differential interferometry”. *Experiments in Fluids* 62.4 (Mar. 2021), p. 81. DOI: 10.1007/s00348-021-03188-6.
- [65] N. J. Parziale, J. E. Shepherd, and H. G. Hornung. “Observations of hypervelocity boundary-layer instability”. *Journal of Fluid Mechanics* 781 (Sept. 2015), pp. 87–112. DOI: 10.1017/jfm.2015.489.
- [66] F. Siddiqui et al. “Mack-mode instabilities on a cooled flared cone with discrete roughness elements at Mach 6”. *Experiments in Fluids* 62.10 (Sept. 2021), p. 213. DOI: 10.1007/s00348-021-03304-6.

- [67] F. Siddiqui, M. Gragston, and R. D. W. Bowersox. “Measurement of Wall-Cooling Effects on Hypersonic Boundary-Layer Transition Using Focused Laser Differential Interferometry”. *AIAA Journal* 60.11 (Nov. 2022), pp. 6214–6224. DOI: 10.2514/1.j061756.
- [68] J. M. Weisberger et al. “Multi-point line focused laser differential interferometer for high-speed flow fluctuation measurements”. *Applied Optics* 59.35 (Dec. 2020), p. 11180. DOI: 10.1364/ao.411006.
- [69] Y. Xiong et al. “Nonlinear Instability Characterization of Hypersonic Laminar Boundary Layer”. *AIAA Journal* 58.12 (Dec. 2020), pp. 5254–5263. DOI: 10.2514/1.j059263.
- [70] E. K. Benitez, J. S. Jewell, and S. Schneider. “Propagation of Controlled Disturbances through an Axisymmetric Separation Bubble at Mach 6”. In: *AIAA AVIATION 2021 FORUM*. Virtual Event, 2–6 Aug. 2021. DOI: 10.2514/6.2021-2844.
- [71] M. C. Neet, J. M. Lawson, and J. M. Austin. “Design, alignment, and calibration of a focused laser differential interferometer”. *Applied Optics* 60.26 (Sept. 2021), p. 7903. DOI: 10.1364/ao.435112.
- [72] B. F. Bathel et al. “Analysis of the Amplitude Response of a Two-Point and a Multi-Point Focused Laser Differential Interferometer”. In: *AIAA Scitech 2021 Forum*. Virtual Event, 11–15, 19–21 Jan. 2021. DOI: 10.2514/6.2021-0598.
- [73] A. Ceruzzi et al. “Non-intrusive velocimetry in a supersonic reacting flow using two-point focused laser differential interferometry”. In: *AIAA SCITECH 2023 Forum*. National Harbor, MD & Online, 23–27 Jan. 2023. DOI: 10.2514/6.2023-0223.
- [74] M. R. Fulghum. “Turbulence Measurements in High-Speed Wind Tunnels Using Focusing Laser Differential Interferometry”. PhD thesis. University Park, PA, USA: The Pennsylvania State University, 2014.
- [75] B. E. Schmidt and J. E. Shepherd. “Analysis of focused laser differential interferometry”. *Applied Optics* 54.28 (Sept. 2015), p. 8459. DOI: 10.1364/ao.54.008459.
- [76] J. M. Lawson. “Focused Laser Differential Interferometry”. PhD thesis. Pasadena, CA, USA: California Institute of Technology, 2021.
- [77] A. P. Ceruzzi. “Development of Two-Point Focused Laser Differential Interferometry for Applications in High-Speed Wind Tunnels”. PhD thesis. College Park, MD, USA: University of Maryland, 2022.
- [78] J. M. Lawson and J. M. Austin. “Focused laser differential interferometer response to shock waves”. *Measurement Science and Technology* 32.5 (Mar. 2021), p. 055203. DOI: 10.1088/1361-6501/abdbd3.
- [79] E. K. Benitez and J. S. Jewell. “Simulated Focused Laser Differential Interferometry of Time-Varying Signals”. In: *AIAA SCITECH 2022 Forum*. San Diego, CA, USA & Virtual, 3–7 Jan. 2022. DOI: 10.2514/6.2022-1312.
- [80] E. K. Benitez et al. “Optical-Axis Spatial Sensitivity of a Simulated Focused Laser Differential Interferometer”. *AIAA Journal* 61.5 (May 2023), pp. 1925–1938. DOI: 10.2514/1.j062270.

- 
- [81] E. K. Benitez et al. “Quantitative focused laser differential interferometry with hypersonic turbulent boundary layers”. *Applied Optics* 61.31 (Oct. 2022), p. 9203. DOI: 10.1364/ao.465714.
- [82] P. Yuldashev et al. “Mach-Zehnder interferometry method for acoustic shock wave measurements in air and broadband calibration of microphones”. *The Journal of the Acoustical Society of America* 137.6 (June 2015), pp. 3314–3324. DOI: 10.1121/1.4921549.
- [83] M. M. Karzova et al. “Characterization of spark-generated N-waves in air using an optical schlieren method”. *The Journal of the Acoustical Society of America* 137.6 (June 2015), pp. 3244–3252. DOI: 10.1121/1.4921026.
- [84] Deutsches Zentrum für Luft - und Raumfahrt (DLR). “The High Enthalpy Shock Tunnel Göttingen of the German Aerospace Center (DLR)”. *Journal of large-scale research facilities* 4, A133 (Oct. 2018). DOI: <http://dx.doi.org/10.17815/jlsrf-4-168>.
- [85] T. Toki et al. “Large-eddy simulation of a hypersonic turbulent boundary layer over a cone in support of focused laser differential interferometry (FLDI) measurements”. In: *12th International Symposium on Turbulence and Shear Flow Phenomena*. Osaka, Japan (Online), 19–22 July 2022.



## A. Lens formula for FLDI $\Delta x_1$ calibration

In publication 1, one of the means employed to obtain the FLDI internal separation distance  $\Delta x_1$  was by looking at the response of the system to a moving lens. The identity:

$$\Delta x_1 = \frac{\lambda_0 f_L}{T}, \quad (\text{A.1})$$

which is Equation (2a) in the publication, was given without further detail. In this appendix, the mathematical deduction of that formula is detailed. The subscript 1 in  $\Delta x_1$  is dropped in the following, for simplicity.

Figure A.1 illustrates the spatial paths traveled by two rays separated by a distance  $\Delta x$ , when going through a plane-convex lens of curvature radius  $R$  at a given distance from its center. The paths traveled within the lens medium are denoted  $L_i$ . We are interested in finding out how the separation distance between the rays,  $\Delta x$ , relates with the FLDI output when crossing the lens.

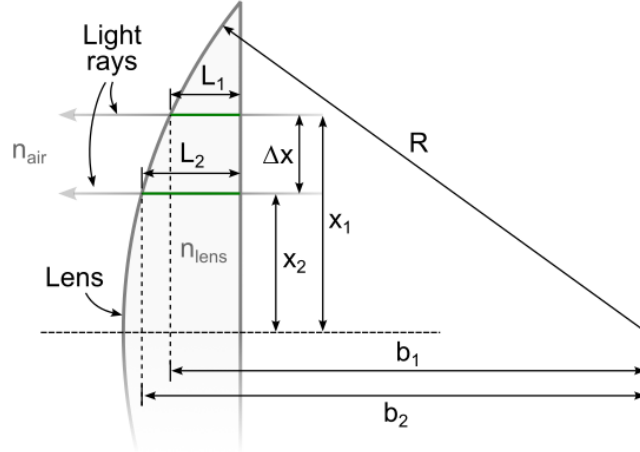


**Figure A.1.:** Schematic drawing of two light rays traveling through a plane-convex lens.

Starting with the basic relationship between the difference in optical path lengths and phase shift of two coherent light rays:

$$\int_{C_1} n(s_1) ds_1 - \int_{C_2} n(s_2) ds_2 = \frac{\lambda_0}{2\pi} \Delta\phi \quad (\text{A.2})$$

where  $C_i$  is the spatial path traveled by each beam, described by the spatial variable  $s_i$ ,  $n$  is the refractive index of the medium,  $\lambda_0$  is the light wavelength, and  $\Delta\phi$  is the resulting phase difference between the two light rays.

The left-hand side of Equation (A.2) corresponds to the optical path lengths. Returning to Figure A.1, when the beams have traveled identical spatial distances  $L_2$ , the optical path lengths are:

$$\int_{C_1} n(s_1) ds_1 = n_{air} (L_2 - L_1) + n_{lens} L_1 \quad (\text{A.3a})$$

$$\int_{C_2} n(s_2) ds_2 = n_{lens} L_2 \quad (\text{A.3b})$$

Assuming  $n_{air} \approx 1$  and  $n_{lens} = n$ , the difference in optical path lengths becomes:

$$\int_{C_1} n(s_1) ds_1 - \int_{C_2} n(s_2) ds_2 = (n - 1) (L_1 - L_2) \quad (\text{A.4})$$

It will be useful to rewrite this expression in terms of the position of the beams  $x_i$  with respect to the center of the lens, in place of the traveled distances  $L_i$ . Using the lengths  $b_i$  in Figure A.1, we note that  $b_i^2 = R^2 - x_i^2$ , and  $L_1 - L_2 = b_1 - b_2$ . Therefore, Equation (A.4) becomes:

$$\int_{C_1} n(s_1) ds_1 - \int_{C_2} n(s_2) ds_2 = (n - 1) \left( \sqrt{R^2 - x_1^2} - \sqrt{R^2 - x_2^2} \right) \quad (\text{A.5})$$

Turning now to the right-hand side of Equation (A.2), the phase difference  $\Delta\phi$  in the FLDI is detected as a voltage by a photodiode as:

$$V = V_0 (1 + \cos(\Delta\phi)) \quad (\text{A.6})$$

To avoid ambiguity of the FLDI response, it is usual to set the undisturbed instrument with a  $\Delta\phi_0 = \pm\pi/2$ . Without losing generality, we choose for the remaining steps a  $\Delta\phi_0 = +\pi/2$ , such that Equation (A.6) becomes:

$$\Delta\phi = -\sin^{-1} \left( \frac{V}{V_0} - 1 \right) \quad (\text{A.7})$$

Substituting Equations (A.5) and (A.7) into Equation (A.2) and rearranging, we have:

$$V = V_0 \left\{ 1 + \sin \left[ \frac{2\pi}{\lambda_0} (n - 1) \left( \sqrt{R^2 - x_2^2} - \sqrt{R^2 - x_1^2} \right) \right] \right\} \quad (\text{A.8})$$

Noting that for any given distance  $x$  with respect to the center of the lens,  $x_1 = x + \Delta x/2$  and  $x_2 = x - \Delta x/2$ , Equation (A.8) can be expressed as:

$$V = V_0 \left\{ 1 + \sin \left[ \frac{2\pi}{\lambda_0} (n - 1) \left( \sqrt{R^2 - \left( x - \frac{\Delta x}{2} \right)^2} - \sqrt{R^2 - \left( x + \frac{\Delta x}{2} \right)^2} \right) \right] \right\} \quad (\text{A.9})$$

Equation (A.9) is the instantaneous FLDI output of a pair of rays crossing a lens at an average distance  $x$  from its center. We will now analyze the argument of the sine function, specifically the terms that depend on  $x$ , which will be denoted  $g(x)$ :

$$g(x) = \sqrt{R^2 - \left(x - \frac{\Delta x}{2}\right)^2} - \sqrt{R^2 - \left(x + \frac{\Delta x}{2}\right)^2} \quad (\text{A.10})$$

Linearizing  $g(x)$  around  $x = 0$ :

$$\begin{aligned} \left. \frac{dg}{dx} \right|_{x=0} &= \left[ \frac{-2\left(x - \frac{\Delta x}{2}\right)}{2\sqrt{R^2 - \left(x - \frac{\Delta x}{2}\right)^2}} - \frac{-2\left(x + \frac{\Delta x}{2}\right)}{2\sqrt{R^2 - \left(x + \frac{\Delta x}{2}\right)^2}} \right] \Bigg|_{x=0} \\ &= \frac{\Delta x}{2\sqrt{R^2 - \left(\frac{\Delta x}{2}\right)^2}} - \frac{-\Delta x}{2\sqrt{R^2 - \left(\frac{\Delta x}{2}\right)^2}} \\ &= \frac{\Delta x}{\sqrt{R^2 - \left(\frac{\Delta x}{2}\right)^2}} \end{aligned} \quad (\text{A.11})$$

Assuming  $R \gg \Delta x$ , the result of Equation (A.11) becomes simply  $\Delta x/R$ , such that  $g(x)$  is linearized as:

$$g(x) \approx \frac{\Delta x}{R} x \quad (\text{A.12})$$

Substituting this in Equation (A.9), the FLDI output can be approximated as:

$$V \approx V_0 \left\{ 1 + \sin \left[ \frac{2\pi \Delta x}{\lambda_0 R} (n-1) x \right] \right\} \quad (\text{A.13})$$

For a thin lens, the curvature radius  $R$  and the focal length  $f_L$  correlate as:

$$\frac{1}{f_L} = (n-1) \left( \frac{1}{R_1} - \frac{1}{R_2} \right) \quad (\text{A.14})$$

where, for a plane-convex lens,  $R_1 = R$  and  $R_2 = +\infty$ . Substituting the resulting relation in Equation (A.13):

$$V \approx V_0 \left[ 1 + \sin \left( 2\pi \frac{\Delta x}{\lambda_0 f} x \right) \right] \quad (\text{A.15})$$

Finally, from Equation (A.15), it can be seen that the sinusoidal response when the FLDI is moved along the axis of the weak lens has a spatial period of  $T = \Delta x/(\lambda_0 f_L)$ , which is the identity that was used in the publication.

It should be noted that if a double-convex lens is used instead of the plane-convex one chosen for the present demonstration, the results remain unchanged. The double-convex lens requires using different parameters in Equation (A.14). However, Equation (A.3a) also changes, its effects being carried over the entire demonstration, ultimately leading to the same identity.



## B. Transfer function of FLDI spatial filtering

A transfer function representing the FLDI spatial filtering was used in publication 3 to assess the FLDI ability to dampen the contributions of disturbances away from the FLDI focus. In the paper, it was presented as Equation (3), repeated below:

$$H_w(k) = e^{-\frac{w^2 k^2}{8}}, \quad (\text{B.1})$$

where  $w$  is the local FLDI beam radius, and  $k$  is the wavenumber of the disturbance.

This equation is often used in FLDI works, but is rarely given any further attention. In the present appendix, this transfer function is demonstrated in detail.

By definition, the transfer function is the ratio between the measured FLDI output and the true value that is probed. Since the FLDI performs a spatial differentiation of the phase of the laser crossing the probed volume,  $\Phi$ , the transfer function  $H$  due to the finite beam width (subscript  $w$ ) is:

$$H_w(k) \triangleq \frac{\left(\frac{d\Phi}{dx}\right)_{\text{measured}}}{\left(\frac{d\Phi}{dx}\right)_{\text{true}}} \quad (\text{B.2})$$

We are interested in the effects of finite beam width. We separate that from the effects of finite FLDI internal separation distance,  $\Delta x_1$ , by assuming that the FLDI performs a perfect derivative, that is,  $\Delta x_1 \rightarrow 0$ . Furthermore, to quantify Equation (B.2), we analyze a generic refraction index disturbance in the form of a sine wave of wavenumber  $k$ , propagating along the axis of beam separation,  $x$ , and having an infinitesimal thickness in  $z$ :

$$n' = A \sin(kx) \delta(z), \quad (\text{B.3})$$

where  $A$  is an arbitrary disturbance amplitude,  $\delta$  is the Dirac delta function, and  $n'$  is the refraction index change with respect to a mean value.

For the numerator in Equation (B.2), we consider the FLDI response to be an area integral of the variables across a finite region, encompassing a bundle of light rays. The corresponding equations were given in publication 2 of the present thesis as Equations (4) and (7). They are repeated below for clarity, in terms of refraction index  $n$  rather than density  $\rho$ , noting that  $n' = K \rho'$ ,  $K$  being the Gladstone-Dale constant. Also, a Cartesian system of coordinates is used instead of polar as in the paper.

$$\Delta\phi = \frac{2\pi}{\lambda_0} \left( \int_{C_1} n'(s_1) ds_1 - \int_{C_2} n'(s_2) ds_2 \right) \quad (\text{B.4})$$

$$\Delta\Phi = \sin^{-1} \left( \iint I_0(x, y) \sin \Delta\phi(x, y) dx dy \right) \quad (\text{B.5})$$

In these equations,  $\phi$  is the phase of the individual rays,  $\Phi$  is the combined phase of all rays in the bundle,  $\lambda_0$  is the wavelength of the light,  $C_i$  is the spatial path traveled by the beams, which is described by the parametric representation  $s_i(x_i, y_i, z_i)$ , and  $I_0$  is the intensity distribution of the rays. Equation (B.4) can be used to calculate the phase difference introduced in each ray by a disturbance field, while Equation (B.5) gives the phase difference after the beams are recombined back together.

Starting with Equation (B.4) the disturbance field of Equation (B.3) yields:

$$\Delta\phi = \frac{2\pi A}{\lambda_0} (\sin(k x_{s_1}) - \sin(k x_{s_2})) \quad (\text{B.6})$$

It should be noticed that, despite the focusing of the FLDI beams, the pairs of rays always describe parallel trajectories separated by a distance  $\Delta x_1$  in the  $x$  direction. Therefore, Equation (B.6) can be generalized in a more clear manner for any ray that is recombined at a given coordinate  $x$ , by replacing  $x_{s_1} = x + \Delta x_1/2$  and  $x_{s_2} = x - \Delta x_1/2$ .

Assuming small phase shift magnitudes ( $\sin \xi \approx \xi$ ), substituting Equation (B.6) into Equation (B.5) yields:

$$\Delta\Phi = \iint I_0(x, y) \frac{2\pi A}{\lambda_0} \left[ \sin \left( k \left( x + \frac{\Delta x_1}{2} \right) \right) - \sin \left( k \left( x - \frac{\Delta x_1}{2} \right) \right) \right] dx dy \quad (\text{B.7})$$

We now differentiate Equation (B.7) in  $x$  by the definition, that is,  $d\Phi/dx = \lim_{\Delta x_1 \rightarrow 0} (\Delta\Phi/\Delta x_1)$ . The term inside the brackets in Equation (B.7) becomes:

$$\lim_{\Delta x_1 \rightarrow 0} \left[ \frac{\sin \left( k \left( x + \frac{\Delta x_1}{2} \right) \right) - \sin \left( k \left( x - \frac{\Delta x_1}{2} \right) \right)}{\Delta x_1} \right] = \frac{d}{dx} \sin(kx) \quad (\text{B.8})$$

Substituting the result of Equation (B.8) in Equation (B.7), the numerator of Equation (B.2) assumes the form:

$$\left( \frac{d\Phi}{dx} \right)_{\text{measured}} = \iint I_0(x, y) \frac{2\pi A}{\lambda_0} k \cos(kx) dx dy \quad (\text{B.9})$$

Before proceeding, an important side note concerns the beam intensity distribution  $I_0$ , which is found with different notations in the literature. The definition used in publications 2 and 3, namely  $\tilde{I}_0(r/w) = 2\pi^{-1} \exp(-2r^2/w^2)$ , with  $r$  the radial coordinate and  $w$  the local beam radius, follows the work of Lawson and Austin [78]. That is a non-dimensional notation with unit area integral, ideal for the application in computational FLDI as a weighting function for the summation of the contributions of each ray to the final signal. However, other works [47, 50, 75, 80] employ a slightly different definition,  $I_0(r) = 2\pi^{-1} w^{-2} \exp(-2r^2/w^2)$ . This notation takes into account the scaling of peak intensity with respect to the total power of the beam, when the beam is expanded. In other words, it is able to represent the fact that the intensity of the laser at the center of the beam is smaller

at larger distances from the focus. This is important to be taken into account in the present deduction, since the response of an expanding beam (numerator in Equation (B.2)) will be compared with that of one that is perfectly focused at all times (denominator). The latter representation will, therefore, be adopted here.

Substituting  $I_0(r)$  in Equation (B.9), with  $r^2 = x^2 + y^2$ :

$$\begin{aligned} \left(\frac{d\Phi}{dx}\right)_{\text{measured}} &= \iint \frac{2}{\pi w^2} e^{-2\left(\frac{x^2+y^2}{w^2}\right)} \frac{2\pi A}{\lambda_0} k \cos(kx) dx dy \\ &= \frac{2\pi A k}{\lambda_0} \frac{2}{\pi w^2} \int_{-\infty}^{+\infty} e^{-\frac{2y^2}{w^2}} \left[ \int_{-\infty}^{+\infty} e^{-\frac{2x^2}{w^2}} \left( \frac{e^{ikx} + e^{-ikx}}{2} \right) dx \right] dy \end{aligned} \quad (\text{B.10})$$

Noting that  $\int_{-\infty}^{+\infty} \exp(-a\xi^2) \exp(-2b\xi) d\xi = \sqrt{\pi/a} \exp(b^2/a)$ , the integral in  $x$  in Equation (B.10) becomes:

$$\begin{aligned} \int_{-\infty}^{+\infty} \frac{1}{2} \left( e^{-\frac{2x^2}{w^2}} e^{ikx} + e^{-\frac{2x^2}{w^2}} e^{-ikx} \right) dx &= \frac{1}{2} \left( \sqrt{\frac{\pi w^2}{2}} e^{-\frac{k^2 w^2}{8}} + \sqrt{\frac{\pi w^2}{2}} e^{-\frac{k^2 w^2}{8}} \right) \\ &= \sqrt{\frac{\pi w^2}{2}} e^{-\frac{k^2 w^2}{8}} \end{aligned} \quad (\text{B.11})$$

Substituting this result in Equation (B.10) and noting that  $\int_{-\infty}^{+\infty} \exp(-a\xi^2) d\xi = \sqrt{\pi/a}$ , we have:

$$\begin{aligned} \left(\frac{d\Phi}{dx}\right)_{\text{measured}} &= \frac{2\pi A k}{\lambda_0} \frac{2}{\pi w^2} \int_{-\infty}^{+\infty} e^{-\frac{2y^2}{w^2}} \sqrt{\frac{\pi w^2}{2}} e^{-\frac{k^2 w^2}{8}} dy \\ &= \frac{2\pi A k}{\lambda_0} \frac{2}{\pi w^2} \sqrt{\frac{\pi w^2}{2}} e^{-\frac{k^2 w^2}{8}} \sqrt{\frac{\pi w^2}{2}} \\ &= \frac{2\pi A k}{\lambda_0} e^{-\frac{k^2 w^2}{8}} \end{aligned} \quad (\text{B.12})$$

Now turning to the denominator in Equation (B.2), an expression for the true derivative can be found by applying the definition directly on Equation (B.6). Identical considerations as before concerning the  $x_{s_i}$  variables apply now, and the result of Equation (B.8) is also used:

$$\begin{aligned} \left(\frac{d\Phi}{dx}\right)_{\text{true}} &= \lim_{\Delta x_1 \rightarrow 0} \left[ \frac{2\pi A}{\lambda_0} \left( \frac{\sin(kx_{s_1}) - \sin(kx_{s_2})}{\Delta x_1} \right) \right] \\ &= \frac{2\pi A}{\lambda_0} k \cos(kx) \end{aligned} \quad (\text{B.13})$$

This equation is evaluated at the position representative of the center of the FLDI beam, i.e.,  $x = 0$ . Hence:

$$\left(\frac{d\Phi}{dx}\right)_{\text{true}} = \frac{2\pi A k}{\lambda_0} \quad (\text{B.14})$$

Finally, Equation (B.1) is obtained by dividing Equations (B.12) and (B.14).